Injectable Multi-drug Formulation for the Postoperative Management of Ocular Surgery

by
Maziar Mohammadi

A dissertation submitted in partial fulfillment
of the requirements for the degree of
Doctor of Philosophy
(Mechanical Engineering)
in the University of Michigan
2017

Doctoral Committee:

Professor Ronald G. Larson, Chair
Associate Professor Jordan J. Green
Assistant Professor Xiaogan Liang
Professor Michael J. Solomon

Maziar Mohammadi

maziar@umich.edu

ORCID id: http://orcid.org/0000-0001-8515-7717

Dedication

To my wife and my parents for their unconditional love and unfailing support.

Acknowledgements

I am very grateful to my advisor, Professor Ronald Larson, for his valuable guidance throughout my PhD research. The fact that he believed in me and allowed me to pursue a topic of research with such complexity has encouraged me to take risks to achieve high rewards and will have a significant impact in my professional life. It would not have been possible to successfully complete my PhD without his endless support and mentorship. In addition to guiding me in my academic endeavors, Professor Larson has taught me a great deal about humility and kindness. He supported me in completing part of my PhD at Johns Hopkins University School of Medicine, which had an immense impact on both my personal and professional life. It has been a true blessing to have him on my side and for that I am very grateful.

I would like to express my sincere thanks to Dr. Jordan Green, Associate Professor at Johns Hopkins University School of Medicine, for allowing me to join his group during the third year of my PhD. Although I was a new member, he made me feel right at home. The lessons I learned from him and his group with regards to drug delivery have been instrumental in achieving my academic goals and will be truly useful in my career.

I would like to thank Dr. Cagri Besirli, Assistant Professor in the Kellogg Eye Center at the University of Michigan, for his responsiveness and encouragements. His valuable advice and intellectual guidance right from the inception of my PhD project through its completion have been extremely useful.

Next, I would like to thank Professor Michael Solomon and Dr. Xiaogan Liang for spending their valuable time to assist as my PhD committee members. Their valuable advice and ideas have had a significant influence in the progress of my PhD.

All of the steps accomplished in the chapters of this dissertation have been made possible by the invaluable input from my colleagues. I am thankful to Eric D. Larson and Jun Liu for developing the Brownian Dynamics model, and Daniel Beltran-Villegas for his immense technical guidance. I appreciate Ali Salehi for his great advice regarding the LbL project and Ryan Branch and Lucas Cygan for their help with the LbL experiments. I am thankful to Professor Nick Kotov for allowing me to use his lab's QCM device as well as LbL robot and Douglas Montjoy from his lab for the many fruitful discussions regarding LbL films. I am thankful to Dr. Ron Shmueli, David Wilson, Jayoung Kim, and Jesse Zheng for their patience and willingness to teach me many valuable lessons regarding drug delivery. I am very grateful to Sandhya Ramachandran for help with the experiments. Kisha Patel is especially thanked for her assistance with performing the experiments and her consistent dedication to research. I am very grateful to Professor Alexander Popel and Dr. Niranjan Pandey for their advice regarding drug formulations. I would also like to thank Nisha Hollingsworth and Ying Liu for their help with the multidrug formulation project. I am very thankful to my collaborators in the projects regarding HIF inhibition: Dr. Akrit Sodhi and Dr. Monika Deshpande (ocular drug delivery), as well as Professor Gregg Semenza and Dr. Debangshu Samanta (cancer project).

In addition, I would like to thank all of the members of Larson group, Elnaz Hajizadeh, Hossein Rezvantalab, Ryan Marson, Taraknath Mandal, Weizhong Zou, Wenjun Huang, Ali Salehi, Kyle Huston, Soroush Moghadam, Abdulrazaq Adams, Ryan Hall, Nisha Hollingsworth, Yufei Wei, and Ying Liu, for the amazing time that I had with them during my stay in Ann Arbor. I am thankful to the members of Green lab at Johns Hopkins University School of Medicine, Dr. Camila Zamboni, Dr. Johan Karlsson, Dr. Stephany Tzeng, Kisha Patel, Sandhya Ramachandran, David Wilson, Jayoung Kim, Randall Meyer, Yuan Rui, Kelly Rhodes, Hannah Vaughan, Elana Ben-Akiva, Denis Routkevitch, James Shamul, Kamran Siddiq, Mark Supernant, and Pranshu Bhardwaj for being so welcoming and for their willingness to help me with my project.

I would like to end my acknowledgments by thanking those who have been with me from the very beginning: my beloved family. I am very grateful to my parents for instilling in me honesty, the desire to grow, and the ambition to achieve my goals. I am eternally in your debt, “Maman” and “Baba.” If it was not for your sacrifice, dedication, support and prayers, I would not be where I am today. In addition, I am very thankful to the love of my life who entered my world at a time when I least expected it, my wife Parisa. During my moments of weakness and doubt, it was her unconditional love and support that made me confident and kept me going. Thank you very much for your understanding and for the many weekends that you spent in the lab working by my side. Next, I would like to thank my kind father-in-law and mother-in-law for their affection, support, and encouragement. Last but not least, especial thanks to my brother and sister for their continued support and affection.

I would like to thank Howard Hughes Medical Institute for the International Student Research Fellowship. The research conducted in this project was supported by the Air Force Office of Scientific Research under MURI project #W911NF-10-1-0518, Research Discovery Fund by Paul R. Lichter, M.D., National Science Foundation, under grant DMR 1403335, and National Institutes of Health under grant No EY026148.

Table of Contents

List of Tables

List of Figures

List of Appendices

Abstract

In this dissertation, the interaction between particles or particles and polymers were examined. In addition, outcomes of such studies were used to develop drug delivery formulations.

Initially, by carrying out Brownian dynamics (BD) simulations binding kinetics between two spheres in the dilute limit under shear flow for the entire Pe values (measure of flow strength) was studied. Effects of Pe, hydrodynamic interactions, inter-particle potential and surface anisotropy were studied. Results were in agreement with previous literature that had limited range of applicability including zero and infinite shear rate Smoluchowski limits, as well as high Pe perturbation results of Feke and Schowalter [J. Fluid Mech. **133**, 17-35 (1983)].

Next, developing a drug delivery system for the postoperative management of ocular surgery was considered. In routine care after cataract surgery, patients are required to receive antibiotics for a week and steroids for at least a month. Later during postoperative treatment period, ocular pressure increases and could be managed by administration of ocular hypotensives, which adds to postoperative treatment burden. Currently, the required drug molecules in the postoperative treatment are delivered mainly by eye drops, which have significant shortcomings, such as poor patient compliance, low drug bioavailability and allergic reactions. Hence, different routes were pursued to make a formulation that reduces reliance on the patients to use eye drops.

Initially, layer-by-layer (LbL) assembly of nanoparticles (NPs) and polyelectrolytes was considered as a viable strategy. The goal was to layer different sheets of LbL films with different drug loaded NPs in order to fine-tune the drug release profile. The effect of different parameters on the growth of LbL films was studied and the optimal conditions to grow thick LbL films with inexpensive blank NPs were attained. Unfortunately, by switching from blank polystyrene NPs to

biodegradable poly(D,L-lactide-co-glycolide) (PLGA) NPs, the growth of LbL films was interrupted.

Therefore, we were faced with the challenge of modifying our research to find a more robust solution for postoperative management following cataract surgery. In a subsequent attempt, the multidrug release system was developed utilizing thermoresponsive polymer solutions. The invented drug release system is composed of microparticles incorporated into a bulk hydrogel that was engineered to be in liquid form at room temperature for simple delivery into the eye and form a hydrogel network at physiological body temperatures to act as a depot release platform. The delivery platform was designed to mimic current topical application of postoperative ocular formulations, releasing the antibiotic for up to a week, and the corticosteroid and the ocular hypotensive agents for at least a month. Different means to finely tune drug release was demonstrated. To ensure the most linear drug release, more hydrophobic blocks such as PLCL should be used in the triblock copolymer. Increasing the hydrophobicity of the polymer encapsulating the drug molecules, it was possible to prolong the release duration of drugs substantially.

Finally, preliminary results on overcoming the poor bioavailability of free drug molecules to be used for the treatment of ocular diseases and cancer were examined. Two anti-hypoxia inducible factors (anti-HIFs) were successfully loaded in PLGA NPs with small particle size and considerable drug loading. Next, drug release from NPs was evaluated, *in vitro*. Finally, the effect of NPs on inhibiting HIF expression and blocking angiogenesis were examined *in vivo*. Results demonstrate significant improvements using NPs compared to free drug.

Chapter 1

Introduction

1.1. Background

Eyes are important body organs. Without them one can't see the beauty of the world surround us. Based on recent reports, approximately 285 million people suffer from severe vision impairment throughout the world, and approximately 7 million people join this community annually.[1,2] As a result, significant effort has been focused on developing technologies for improving the delivery of the drug molecules to the eyes, improving treatment outcomes and enhancing vision recovery rate. Anatomy of an eye is shown in Fig. 1.1. Eye is a particularly attractive organ for drug delivery application. It is more accessible compared to internal body organs. This eases the direct injection of the drug delivery system to the eye avoiding the toxicity caused by drug molecules delivered through systemic drug delivery. Even though for drug delivery to other parts of the body, there are restrictions on the size of the drug delivery vehicle (e.g. <200 nm particles for intravenous drug delivery), tolerance of the eye for implants is much higher, since as shown in Fig. 1 vitreous cavity has a large volume (~4 ml in a human eye) and can accept large implants as long as they don't interfere with the vision. In fact, implants as large as few mm long (e.g. Iluvien® which is 3.5 mm long) have been approved by FDA for the intravitreal injection to the eye.[2,3] In addition, with local delivery of the implant to the target site, the required dosage of the drug for the optimum effectiveness is relatively low compared to other route of administrations. In this regard, several technologies have been developed to deliver drug molecules to the eye, and they are summarized in the following sections.

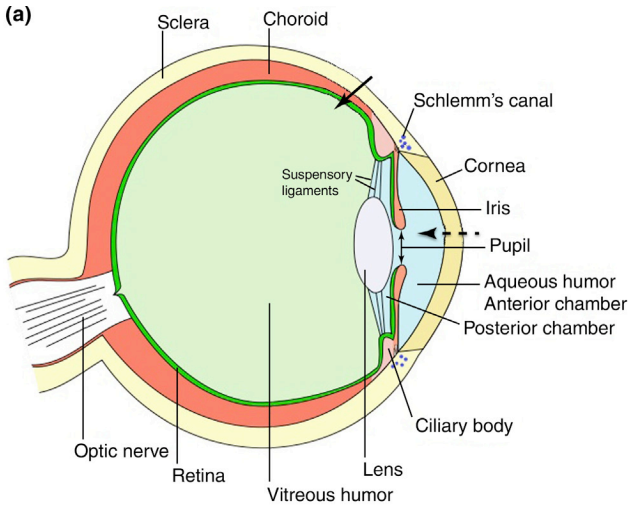

Fig. 1.1. Anatomy of the eye.[4]

1.1.1. Eye drops

Eye drops are the most commonly used drug delivery schemes for the treatment of eye diseases. They are inexpensive and less invasive compared to intraocular injections. However, they have several shortcomings, which has limited their treatment efficiency. Majority of the patients with ocular disorders are elderly, so they might have difficulty using eye drops. In addition, due to rapid clearance of small drug molecules by the body, eye drops have to be administered between 4 to 8 times daily, which is not only a burden for the patients, but also might reduce treatment outcomes if the drug is not administered at the right time. Due to presence of several ocular barriers as well as drug clearance by the tear flow and blinking, below 5% of administered dose makes it to the target site in the eye.[2,5,6] As a result, eye drops are dosed several times higher than the dosage required for the treatment. Drug overdose as well as some of the excipients that are used in eye drops could lead to burning sensation, eye surface irritation, and allergic reactions.[7,8] All in all, there is huge patient noncompliance when it comes to using eye drops.[1,9,10]

1.1.2. Topical gels

In situ forming gels are introduced to avoid rapid clearance of drug administered through eye drops. They are typically a viscose liquid and after instillation form a gel, due to change in pH, temperature, and ionic strength of the solution. These gels have a higher residence time on the surface of the eye and they are more likely to have a higher bioavailability (the required drug concentration in the eye) compared with eye drops. In addition, topical gels could sustain the release of drug molecules on the surface of the eye, thereby reduce the need for frequent administration.[4] Some in situ forming gels are currently available in the market for the treatment of bacterial conjunctivitis, inflammation and glaucoma.[4] However, these gels with the drug molecules loaded in have to be transparent to avoid interference with the vision. In addition, even though using these gels reduces the administration frequency, there will still be reliance on patients to instill these gels on a daily basis.[4]

1.1.3. Contact lenses

Contact lenses are alternative means of sustaining the drug release duration on the surface of the eye, and reducing the reliance on the patient to administer the drug molecules via eye drops or gels. The fact that contact lenses could serve the dual purpose of improved vision as well as delivering the required medications to the eye for chronic diseases makes them a more attractive option. In addition, unlike other implants, contact lenses don't require intraocular injection and thus, they are a less invasive treatment option. Contact lenses could cause patient discomfort over time. In addition, wearing them for a long time may increase the risk of bacterial growth and infection.[11] Further improvement in drug release technologies used in contact lenses (e.g. nanoparticles (NPs), micelles, liposomes, layer-by-layer films, etc.) are required to prolong the drug release duration, avoid sudden burst release of the drug from contact lenses during use or storage, and enhance their shelf life.[12-14] In addition, such sustained release technologies should

not dramatically alter mechanical properties of the contact lenses and their ability to permeate oxygen and ions. Incorporation of the drug molecules could also reduce the transparency of the contact lenses and interfere with the vision.[12] Contact lenses have been subject of extensive research on treatment of glaucoma or inflammation.[12] However, due to the mentioned limitations, they have not made their way to the market yet.

1.1.4. Nanocarriers

There have been numerous studies on the use of nanocarriers in different forms including polymeric NPs, micelles, dendrimers, liposomes for drug delivery to the eye.[15] Due to their small size targeted nanocarriers could bind and localize to the target site and reduce the side effect of drug molecules by local drug delivery.[16] Nanocarriers have either been administered as a topical formulation[17] as well as direct injection into the vitreous cavity.[18] A potential concern with nanocarriers is appearance of snow-globe effect and their interference with the vision due to their small size and resulting Brownian motion. In addition, nanocarriers degrade too fast to be able to sustain the release of the drug molecules for an extended period of time. Furthermore, due to their small size, drug loading in nanocarriers could be limited. Lastly, aggregation of nanocarriers in the container closure (which will impact the ultimate product's shelf-life) or after administration in the eye (which reduces their localization in the target site) should be addressed.[16]

1.1.5. Proteins

Proteins are an efficient means to treat the diseases of the back of the eye including age related macular degeneration, diabetic retinopathy and macular edema. Due to their large size (>100 kDa), they can't cross the ocular barriers if administered in the form of topical formulations and thus they are delivered to the eye with direct intraocular injections.[1,19] Proteins have fewer side effects compared to small molecule drug delivery, as they are made up of amino acid sequences

that are found naturally in the body. They are several proteins approved by FDA including Aflibercept also known as Eylea® and Ranibizumab also known as Lucentis® for the treatment of diseases of the back of the eye. One of the limitations of the proteins is their short intravitreal half-life and fast clearance from the eye. This requires subsequent injection of proteins to ensure their optimal efficiency. Frequent injections are not only an inconvenience for the patients but also lead to several complications including retinal detachment, infection and cataract formation. To prolong their effect, proteins have been encapsulated in the sustained release mechanisms.[19]

1.1.6. Implants

There are several FDA approved implants, including Retisert®, Vitrasert®, Ozurdex®, and Iluvien® for the sustained delivery of small molecules to the eye.[2] The ability of these implants to prolong the release of encapsulated drug molecules for several months is remarkable. Retisert and vitrasert are non-biodegradable and they require a surgical procedure for implantation and a follow up surgery for removal once the drug molecule is completely released. Ozurdex is a biodegradable implant and can be administered via intravitreal injection. A common side effect for all of the mentioned implants is elevation of ocular pressure.[2,20-25] To suppress elevated ocular pressure, patients need to use anti-glaucoma drugs.

1.1.7. Multidrug delivery systems

Despite the significant effort on development of sustained release technologies for the treatment of ocular diseases, there has not been much focus on delivering multiple drug molecules to the eye. Some of the mentioned technologies are designed to release a single drug molecule. Modifying those technologies to enable multidrug delivery would make them more complex and reduces their reliability. For the eye drops and topical gels, having multiple drugs in the same solution could risk unfavorable drug-drug interactions and reduces the treatment efficiency.

ODTx, which stands for "on demand therapeutics," is a multi-chamber stimuli responsive ocular implant. It can hold multiple drug molecules in its chambers and by laser activation and resulting increase in its membrane pore size, it can initiate the release of drug molecules. The implant is currently being evaluated in preclinical studies.[2,26]

To address the challenges in the treatment of proliferative vitreoretinopathy, Zhou et al designed a multidrug implant.[27] The implant was a cylinder made out of PLGA and was capable of releasing a corticosteroid, an antimetabolite, and a thrombolytic drug to the eye. Using a 20-gauge needle, the implant could be delivered to the eye via intravitreal injection. They demonstrated sustained drug release profile and the ability to finely tune it for several weeks.[27]

1.2. Dissertation overview

One of the objectives of this dissertation is to study the interaction between particles with each other or particles and polymers. The overall goal is to use these findings to develop formulations for drug delivery applications. Initially, some fundamental understanding about binding kinetics of particles and assembling those in different layers between polyelectrolytes are obtained.

In Chapter 2, Brownian dynamics (BD) simulations are performed to study the binding kinetics of two particles in the dilute limit under shear flow. The goals were:

- To calculate the binding kinetics between two particles considering hydrodynamic interactions, and various interparticle forces to capture the previous data reported in the literature, which had limited applicability and also go beyond that and provide binding kinetic results for the entire flow strength.
- To study the binding time of anisotropic particles for various flow strength

Next, effect of interactions between particles and polymers to grown layer-by-layer (LbL) films is addressed in Chapter 3. The goal of chapter 3 is as follows:

- To study the effect of polyelectrolyte molecular weight, ionic strength of the media as well as particle size and charge on the growth of LbL films.
- To demonstrate the ability to grow LbL films with thickness of at least few microns.

As the next step, the outcomes of these studies were used to develop formulations for drug delivery applications. Initially, drug delivery for postoperative management of ocular surgery (and cataract surgery in particular) is considered. In routine care after cataract surgery, patients are required to receive antibiotics (for a week) to prevent infection and steroids (for at least a month) to suppress any inflammatory response. Following a few days after surgery, elevation of ocular pressure could occur, due to inflammation or steroid response. To control ocular pressure, ocular hypotensives need to be delivered (for at least a month). For the postoperative management following ocular surgery, the current treatment paradigm is using eye drops and relying on the patients (who are usually elderly) to properly administer the drug molecules at the right time. Limitations of the eye drops were highlighted in the previous section. Hence, to overcome such limitations, the technology is optimized *in vitro* to make sure all three drug molecules required for postoperative management of cataract surgery can be released at required concentrations and proper timing.

To develop the multidrug carrier, the initial goal was to use LbL assembly of drug loaded NPs and polyelectrolytes. The plan was to use inexpensive polystyrene particles for the initial studies (demonstrated in Chapter 3) and once the optimum parameters to grow thick LBL films were determined, particles would be replaced with more valuable drug loaded biocompatible particles. Our preliminary results indicated that growth of LbL films is challenging with large NPs. In addition, Jianshan Liao, a member of Larson Group observed that biodegradable particles further slow down growth of such films.[28] Finally, over the course of this part of the project, the low reliability of LbL films to fine-tune the release of multiple drugs became more obvious due to their uneven surface morphology. These findings triggered the use of a different idea to enable multidrug delivery platform.

In a subsequent attempt, thermoresponsive hydrogels were employed to address the need for such drug delivery system (Chapter 4). The thermoresponsive hydrogels are liquid at room temperature, which enables injectability. Upon exposure to body temperature, they form a depot for sustaining the release of drug molecules. This chapter addresses the following points:

- To load drug molecules with different hydrophobicity and dosage as well as release duration requirements in thermoresposnive hydrogels.
- To show the flexibility of the drug delivery system in finely tuning the drug release dosage, profile and duration for different drug molecules encapsulated, *in vitro*.

The technology that is developed during this PhD project and highlighted in Chapter 4 could be widely applied for different ocular indications by changing the drug molecule encapsulated in the MPs or in the hydrogel network.

Chapter 5 presents preliminary results on using anti-hypoxia inducible factors (anti-HIF) loaded NPs to treat cancer and eye diseases. The overall goal of this chapter is as follows:

- To synthesize NPs loaded with anti-HIF agents with small enough particles size (<200 nm) and high drug loading (>10 µg/mg of NPs).
- To evaluate pharmacokinetics of NPs *in vivo.*
- To prolong the effect of anti-HIF agents on inhibition of HIF expression or angiogenesis.

Finally, chapter 6 briefly highlights the obtained results and provides recommendations for future directions.

1.3. References

1 Kim, Y. C., Chiang, B., Wu, X., & Prausnitz, M. R. Ocular delivery of macromolecules. *Journal of Controlled Release* **190** 172-181 (2014).

2 Yasin, M. N., Svirskis, D., Seyfoddin, A., & Rupenthal, I. D. Implants for drug delivery to the posterior segment of the eye: A focus on stimuli-responsive and tunable release systems. *Journal of Controlled Release* **196**, 208-221 (2014).

3 <http://www.iluvien.com/hcp/wp-content/uploads/2015/02/admin_guide.pdf> (2017).

4 Destruel, P.-L., Zeng, N., Maury, M., Mignet, N. & Boudy, V. In vitro and in vivo evaluation of in situ gelling systems for sustained topical ophthalmic delivery: state of the art and beyond. *Drug discovery today* **22**, 638-651 (2017).

5 Rawas-Qalaji, M., & Williams, C. A. Advances in ocular drug delivery *Current Eye Research* **37**, 345-356 (2012).

6 Mehta, P. *et al.* Approaches in topical ocular drug delivery and developments in the use of contact lenses as drug-delivery devices. (2017).

7 Hugues, F.-C. & Le Jeunne, C. Systemic and local tolerability of ophthalmic drug formulations. *Drug Safety* **8**, 365-380 (1993).

8 Vaede, D., Baudouin, C., Warnet, J. & Brignole-Baudouin, F. Preservatives in eye drops: toward awareness of their toxicity. *Journal francais d'ophtalmologie* **33**, 505-524 (2010).

9 Newman-Casey, P. A. *et al.* Patterns of glaucoma medication adherence over four years of follow-up. *Ophthalmology* **122**, 2010-2021 (2015).

10 Newman-Casey, P. A. *et al.* The most common barriers to glaucoma medication adherence: a cross-sectional survey. *Ophthalmology* **122**, 1308-1316 (2015).

11 Guzman-Aranguez, A. *et al.* Dry eye treatment based on contact lens drug delivery: a review. *Eye & contact lens* **42**, 280-288 (2016).

12 Maulvi, F. A., Soni, T. G. & Shah, D. O. A review on therapeutic contact lenses for ocular drug delivery. *Drug delivery* **23**, 3017-3026 (2016).

13 Hu, X. *et al.* Synthesis and surface modification of chitosan containing hydrogel for ophthalmic drug delivery. *Materials Technology* **29**, 144-151 (2014).

14 Huang, J.-F. *et al.* A hydrogel-based hybrid theranostic contact lens for fungal keratitis. *ACS nano* **10**, 6464-6473 (2016).

15 Wang, X., Wang, S. & Zhang, Y. Advance of the application of nano-controlled release system in ophthalmic drug delivery. *Drug delivery* **23**, 2897-2901 (2016).

16 Weng, Y. *et al.* Nanotechnology-based strategies for treatment of ocular disease. *Acta pharmaceutica sinica B* **7**, 281-291 (2017).

17 Ibrahim, M. M., Abd-Elgawad, A.-E. H., Soliman, O. A.-E. & Jablonski, M. M. Stability and Ocular Pharmacokinetics of Celecoxib-Loaded Nanoparticles Topical Ophthalmic Formulations. *Journal of pharmaceutical sciences* **105**, 3691-3701 (2016).

18 Li, H., Palamoor, M. & Jablonski, M. M. Poly (ortho ester) nanoparticles targeted for chronic intraocular diseases: ocular safety and localization after intravitreal injection. *Nanotoxicology* **10**, 1152-1159 (2016).

19 Radhakrishnan, K. *et al.* Protein delivery to the back of the eye: barriers, carriers and stability of anti-VEGF proteins. *Drug discovery today* **22**, 416-423 (2017).

20 Holbrook, J. T., Sugar, E. A., Burke, A. E., Vitale, A. T., Thorne, J. E., Davis, J. L., Jabs, D.A., and Multicenter Uveitis Steroid Treatment (MUST) Trial Research Group. Dissociations of the Fluocinolone Acetonide Implant: The Multicenter Uveitis Steroid Treatment (MUST) Trial and Follow-up Study. *American Journal of Ophthalmology* **164**, 29-36 (2016).

21 Jaffe, G. J., Martin, D., Callanan, D., Pearson, P. A., Levy, B., Comstock, T., & Fluocinolone Acetonide Uveitis Study Group. Fluocinolone acetonide implant (Retisert) for noninfectious posterior uveitis: thirty-four–week results of a multicenter randomized clinical study. *Ophthalmology* **113**, 1020-1027 (2006).

22 Tservakis, I., Koutsandrea, C., Papaconstantinou, D., Paraskevopoulos, T., & Georgalas, I. Safety and efficacy of dexamethasone intravitreal implant (Ozurdex) for the treatment of persistent macular edema secondary to retinal vein occlusion in eyes previously treated with anti-vascular endothelial growth factors. *Current Drug Safety* **10**, 145-151 (2015).

23 Sella, R., Oray, M., Friling, R., Umar, L., Tugal-Tutkun, I., & Kramer, M. Dexamethasone intravitreal implant (Ozurdex®) for pediatric uveitis. *Graefe's Archive for Clinical and Experimental Ophthalmology* **253**, 1777-1782 (2015).

24 Campochiaro, P. A., Brown, D. M., Pearson, A., Ciulla, T., Boyer, D., Holz, F. G., Tolentino, M., Gupta, A., Duarte, L., Madreperla, S., Gonder, J., Kapik, B., Billman, K., Kane, F., and FAME Study Group. Long-term benefit of sustained-delivery fluocinolone acetonide vitreous inserts for diabetic macular edema. *Ophthalmology* **118**, 626-635 (2011).

25 Cunha-Vaz, J., Ashton, P., Iezzi, R., Campochiaro, P., Dugel, P. U., Holz, F. G., Weber, M., Danis, R.P., Kuppermann, B.D., Bailey, C., Billman, K., Kapik, B., Kane, F., Green, K., for the FAME Study Group. Sustained delivery fluocinolone acetonide vitreous implants: long-term benefit in patients with chronic diabetic macular edema. *Ophthalmology* **121**, 1892-1903 (2014).

26 Sepahvandi, A., Eskandari, M. & Moztarzadeh, F. Drug Delivery Systems to the Posterior Segment of the Eye: Implants and Nanoparticles. *BioNanoScience* **6**, 276-283 (2016).

27 Zhou, T., Lewis, H., Foster, R. E. & Schwendeman, S. P. Development of a multiple-drug delivery implant for intraocular management of proliferative vitreoretinopathy. *Journal of Controlled Release* **55**, 281-295 (1998).

28 Liao, J. Undergraduate research report. *Unpublished document* (2016).

Chapter 2

Brownian Dynamics Simulations of Coagulation of Dilute Uniform and Anisotropic Particles under Shear Flow Spanning Low to High Peclet Numbers

This chapter is reproduced from [M Mohammadi, ED Larson, J Liu, RG Larson, Brownian dynamics simulations of coagulation of dilute uniform and anisotropic particles under shear flow spanning low to high Peclet numbers, 2015, The Journal of Chemical Physics 142 (2), 024108.], with the permission of AIP Publishing.

2.1. Introduction

Coagulation of colloids has considerable practical application, including but not limited to removing undesired reactants or bi-products from industrial solutions,[1] inducing surface modification,[2,3] and creating ordered colloidal structures.[4-6] On the other hand, for some cases, it is desirable to prevent flocculation to maintain a homogenous suspension applicable to pharmaceutics,[1] inkjet printing, coatings,[7] and heat transfer fluids[8-10] to name a few. Thus, fully understanding the binding kinetics of colloids is essential to expedite or delay flocculation.

For a dilute suspension, the first stage in coagulation is the formation of binary pairs. Brownian diffusion and flow convection are the major mechanisms affecting coagulation. The terms "perikinetic" and "orthokinetic" apply to coagulation in the limits where Brownian diffusion and flow convection, respectively, dominate the rate of coagulation.[11] These two limits correspond to zero and infinite Peclet number, respectively, where the Peclet number is defined as the ratio of shear rate to particle diffusion rate.

A century ago, Smoluchowski determined the collision rates of dilute spheres in both the perikinetic and orthokinetic limits, where hydrodynamic interactions (HI) between the spheres are neglected. This collision rate equals the flocculation rate if particle attractions are infinitely strong and infinitely short-ranged, so that particle motions are unaffected by inter-particle forces until contact, and then the particles bind irreversibly. The average Smoluchowski flocculation time (t_B) multiplied by the particle number concentration (n) gives a rescaled flocculation time t_V, which is given by Eqs. (2.1) and (2.2), respectively for the perikinetic and orthokinetic limits.[12,13] Later, by introducing the concept of a "stability ratio" W, defined by Eq. (2.3), the effects of both HI and finite-range attractive potentials were taken into consideration.[13]

$$t_{V-B}^{Smoluchowski} = t_B n = \frac{1}{J_B^{Smoluchowski}} = \frac{3\mu}{8k_B T} \tag{2.1}$$

$$t_{V-S}^{Smoluchowski} = t_S n = \frac{1}{J_S^{Smoluchowski}} = \frac{3}{32\dot{\gamma}a^3} \tag{2.2}$$

$$W = \frac{t_V}{t_V^{Smoluchowski}} = \frac{J^{Smoluchowski}}{J} \tag{2.3}$$

In the above, t_V denotes binding time per unit volume (i.e., binding time multiplied by particle concentration as noted above), μ is the fluid viscosity, J is the coagulation rate per unit concentration, a is the particle radius, k_B is the Boltzmann constant, T is the temperature, W is the stability ratio, and $\dot{\gamma}$ is the shear rate. Moreover, the subscripts B and S denote Brownian and shear dominated flocculation, respectively. Calculations of the stability ratio and therefore binding time have been reported in the presence of HI and finite-ranged potentials, in both the perikinetic and orthokinetic limits.[13,14]

Determining the binding time outside of the perikinetic and orthokinetic limits, where both Brownian diffusion and fluid convection are important, is challenging.[13] Swift and Friedlander suggested linear independence of Brownian motion and shearing flow, so that their effects on the

rate of binding could be simply added together.[15] They backed this idea with their experimental results for polystyrene particles. However, later, more detailed, studies proved that the presumed linear independence of Brownian motion and flow is not valid.[11,13,16]

Thirty years ago, Feke and Schowalter therefore carried out a perturbation expansion of the convection-diffusion equation for spherical particles to determine the effects of weak Brownian motion on orthokinetic coagulation.[13] They considered the effects of finite-ranged inter-particle forces (electrostatic repulsion and induced-dipole attraction), as well as HI. (With HI present, the finite-range attractive forces must become singular at particle contact to drive particle contact in the presence of singular lubrication resistances.) Their analysis yielded both the binding rate in the orthokinetic (infinite Pe) limit, plus a correction term of order $1/Pe$. They set a uniform particle concentration boundary condition in the upstream region. Thus, their method only applies to a strongly convection-dominated regime. They studied both shear and uniaxial extensional flows and emphasized the nonlinear relationship between Brownian diffusion and flow type and strength. They concluded that, depending on the flow number, which is the dimensionless ratio of the strength of the flow to the strength of the attractive potential, weak Brownian motion can lead to a positive or negative deviation from the orthokinetic coagulation rate.

Lattuada and Morbidelli recently (in 2011) carried out a numerical simulation using a finite difference method to study the effect of repulsive inter-particle forces on steady-state coagulation of binary pairs in an axisymmetric extensional flow, over the entire range of Pe values, with HI.[1] Their effort is one of the most advanced numerical studies of flow-induced coagulation to date. However, they noted that the governing convection-diffusion equation is very stiff, and implementation of both the short-ranged inter-particle interactions, and the far field boundary conditions, necessitated limiting their analysis to flows with cylindrical symmetry to reach converged results. Thus, simulating shear flows, for which the particle concentration field is three-dimensional, was still not possible using their method, even with modern computer power.

Another scheme employed for predicting the flocculation rate of colloids is Brownian dynamics (BD) simulations, in which a Langevin stochastic differential equation is numerically integrated in order to determine the positions of particles and their collision rates at discrete time intervals. Xu et al. recently performed BD simulations in the absence of HI to determine the rate of formation of particle pairs at intermediate shear rates between the perikinetic and orthokinetic limits.[11] They avoided problems of specifying boundary conditions for determining the steady-state rate of coagulation by solving an initial value problem of a shear flow suddenly imposed on a suspension of 20,000 spheres initially randomly distributed in a periodic cubic box. They calculated the initial rate of formation of particle pairs over a long enough time to get a reasonable average but short enough to avoid loss of many particles. Their method, while valid in principle, is wasteful in that a vast majority of particles does not collide and so does not contribute to the average collision time. The use of a huge number of spheres allows good averages to nevertheless be obtained, but also makes extension of the method to allow inclusion of HI impossibly expensive.

Within the past year, Kelkar et al. employed two theoretical models and BD simulations to investigate binding kinetics of dense colloidal suspensions in the absence of flow.[7] They also neglected HI, but accounted for short-time effects on binding in the dense-concentration limit, where particle-particle correlations affect the time-dependent binding rate. As an initial state, they assumed an equilibrated particle spatial distribution in the absence of coagulation, and then suddenly switched on the binding of colliding particles. In fact, attaining such an initial condition for particles capable of coagulation would appear to be a challenging task experimentally.

This brief summary of both now-classic work, and very recent theory and simulations, shows that *the basic problem of coagulation rates of sheared colloidal suspensions has not been solved, even in the dilute-particle limit and with spherical particles, except for negligibly slow or very fast flows.* In addition, novel colloids with non-uniform surface composition or dimpled surfaces have been introduced recently as building blocks for producing complex structures like helices,

and chains.[4-6] A particular example of particles with spherical shape but anisotropic interaction, is that of "Janus" particles, with an axisymmetric surface "cap" or face with attractive interactions that differ from that of the rest of the particle surface. For Janus spheres, in addition to separation distance, relative orientation of particles also affects binding kinetics. Determination of aggregation rates for Janus spheres by solving a convection-diffusion equation (e.g., such as that solved by Lattuada and Morbidelli[1]) would be even challenging than solving it for uniform spheres in shearing flow, because of the two extra degrees of freedom required to keeping track of the orientational degrees of freedom of the two colliding particles.

Recently, Larson Group implemented a BD simulation method to study binding kinetics of colloids, including Janus colloids, in the dilute limit, in the absence of flow, in the presence or absence of a potential, and with full HI.[6] A key innovation in this method was the use of BD calculations with only two spheres, since in the dilute limit only the interactions of pairs of spheres can influence the binding rate, even with HI. Here, this method is extended to investigate the effects of shearing flow of arbitrary strength on coagulation. The goal of this research is to provide a robust simulation method, able to predict recognition kinetics of colloids over the whole Pe range, in the dilute limit. (The developed method is extendable to the non-dilute limit by breaking HI into near-field lubrication and far-field multibody interactions with the method of Stokesian dynamics,[17] although this extension is not undertaken here.) To cope with the far-field boundary conditions at infinity, a set of periodic rectangular simulation boxes with different aspect ratios and different sizes are used and results are extrapolated towards infinite box size. In this way, a "shear-induced shadow effect" is overcome whereby parts of the box suffer a statistical depletion of particles that becomes non-physical in a finite periodic box, when either the fore and aft shadows, or the side shadows interact. Simulation results are compared and validated with several existing reports in different coagulation regimes, including the Smoluchowki no-HI limits,[12] and the results from Feke and Schowalter[13] in the high-shear limit with HI and attractive interactions. Also, different potential types are employed to consider a

range of inter-particle forces from pure attraction to a combination of attraction and repulsion. The ability to simulate particles with surface anisotropy opens promising routes for better understanding shear-enhanced self-assembly of complex structures formed from novel anisotropic colloids.

2.2. Simulation methodology

The code for Brownian dynamics simulations was developed by Eric Larson and Jun Liu under direction of Professor Ronlad Larson. The contribution of author of this dissertation in this regard was finding the proper boundary conditions and simulation box size to ensure the convergence of the results.

2.2.1. Incorporation of shear flow in Brownian dynamics method

Previously,[6] a 12×12 resistance matrix was established to account for the translational and rotational motions between two spheres induced by HI using formulae given by Jeffrey and Onishi.[18] The basics of the implemented BD method are described in Appendix A. Essentially, to include the effects of shear flow, another term has to be included in the Langevin stochastic equation (See Appendix A), which describes shear-induced HI effects. This term entails double-dot products of third-rank g or h tensors into the second-rank rate of strain (E) tensor. Eq. (2.4) can be written following Jeffrey's work:[19]

$$\begin{pmatrix} U_1 \\ U_2 \\ \Omega_1 \\ \Omega_2 \end{pmatrix} = \mu^{-1} \begin{pmatrix} a_{11} & a_{12} & \tilde{b}_{11} & \tilde{b}_{12} \\ a_{21} & a_{22} & \tilde{b}_{21} & \tilde{b}_{22} \\ b_{11} & b_{12} & c_{11} & c_{12} \\ b_{21} & b_{22} & c_{21} & c_{22} \end{pmatrix} \begin{pmatrix} F_1 \\ F_2 \\ T_1 \\ T_2 \end{pmatrix} + \begin{pmatrix} g_{11} & g_{12} \\ g_{21} & g_{12} \\ h_{11} & h_{12} \\ h_{21} & h_{22} \end{pmatrix} \begin{pmatrix} E \\ E \end{pmatrix} + \begin{pmatrix} U(x_1) \\ U(x_2) \\ \Omega \\ \Omega \end{pmatrix} \tag{2.4}$$

The elements $a, b(\tilde{b})$ and c are second-rank tensors which relate the forces and torques on each sphere to their translational and rotational velocities. The tilde sign on b matrices is the transpose operator.[20] Also, g and h are third-rank tensors describing the coupling between the flow field and the resulting translational and rotational motion, respectively.[19,20] In addition, E is the rate of strain tensor for a shear flow, U is the translational velocity, Ω is the rotational velocity, μ is the fluid viscosity, and F and T are the external force and torque exerted on each sphere, respectively. Finally, x is the position vector.[19,20]

In Eq. (2.4), subscripts 1 and 2 for variables or matrices refer to spheres 1 and 2, respectively. For instance, a_{12} is the proportionality constant multiplying the force exerted on sphere 2 (F_2) to give the translational velocity of sphere 1 (U_1). Finally, variables without a subscript describe the flow.[19,20]

Shear flow at any point is described by a superposition of a solid-body rotation and an extensional flow via Eq. (2.5):

$$v^S = \Omega \times x + E \cdot x \tag{2.5}$$

where x is the position vector, and Ω and E are the vorticity vector and rate of strain tensor, respectively.

In Eq. (2.4), mobility tensors $a, b(\dot{b})$ and $\mathcal{C}$ are obtained by inverting the 12×12 resistance matrix established previously.[6] To describe the shear-induced HI effects on the translation and rotation of spheres, the general form of the third-rank tensors mentioned in Eq. (2.4), i.e. g_{11}, g_{12}, g_{21}, g_{22}, h_{11}, h_{12}, h_{21}, and h_{22} for far and near-field cases, must be obtained using Eq. (2.6).[19,20]

$$\begin{pmatrix} g_{11} & g_{12} & h_{11} & h_{12} \\ g_{21} & g_{22} & h_{21} & h_{22} \end{pmatrix} = \begin{pmatrix} G_{11} & G_{12} & H_{11} & H_{12} \\ G_{21} & G_{22} & H_{21} & H_{22} \end{pmatrix} \begin{pmatrix} a_{11} & a_{12} & \tilde{b}_{11} & \tilde{b}_{12} \\ a_{21} & a_{22} & \tilde{b}_{21} & \tilde{b}_{22} \\ b_{11} & b_{12} & c_{11} & c_{12} \\ b_{21} & b_{22} & c_{21} & c_{22} \end{pmatrix} \tag{2.6}$$

The dimensionless resistance functions $G_{ijk}^{(\alpha\beta)}$ and $H_{ijk}^{(\alpha\beta)}$ can be obtained using Eqs. (2.7) and (2.8), respectively.[19]

$$G_{ijk}^{(\alpha\beta)} = X_{\alpha\beta}^{G}(d_i^{'}d_j^{'} - \frac{1}{3}\delta_{ij})d_k^{'} + Y_{\alpha\beta}^{G}(d_i^{'}\delta_{jk} + d_j^{'}\delta_{ik} - 2d_i^{'}d_j^{'}d_k^{'}) \tag{2.7}$$

$$H_{ijk}^{(\alpha\beta)} = Y_{\alpha\beta}^{H}(d_i^{'}\varepsilon_{jkm}d_m^{'} + d_j^{'}\varepsilon_{ikm}d_m^{'}) \tag{2.8}$$

where $d^{'}$ is a unit vector connecting the centers of the spheres, δ is Kronecker delta, and ε is the third-rank Levi-Civita tensor. Also, α and β are used to refer to spheres 1 or 2, while subscripts i, j, and k, (and dummy variable m) are employed to distinguish matrix and vector elements defined by the three spatial dimensions, where G, and H are third-rank tensors. Moreover, X and Y represent the hydrodynamic functions for flows axisymmetric and transverse to spheres' centerlines, respectively, as discussed in Jeffrey.[19] Similar to figures shown in the previous publication by Larson Group,[6] the G, and H functions were plotted against gap between the spheres and it was concluded that the cross-over formulae given by Jefferey and Onishi[18] and Jeffrey[19] appropriately bridge the near- and far-field limits.

In Eqs. (2.7) and (2.8), when $d_1^{'} = 1,\ d_2^{'} = 0,$ and $d_3^{'} = 0$, the centers of the two spheres are on the x-axis, and the expressions for the third-rank tensors $G_{ijk}^{(\alpha\beta)}$ and $H_{ijk}^{(\alpha\beta)}$ become relatively simple. To determine the effect of shear flow for an arbitrary orientation between the two spheres without needing to express $G_{ijk}^{(\alpha\beta)}$ and $H_{ijk}^{(\alpha\beta)}$ for all particle configurations, a special frame is defined in which the x axis is oriented along the axis connecting the centers of the two spheres.

The tensor E describing the shear flow is rotated into the special frame using a matrix Q which is defined as:

$$Q(\theta,\phi) = R_x(\phi)R_z(\theta) \tag{2.9}$$

Where R is the standard rotation matrix, and θ and ϕ correspond to the polar and azimuthal angles with respect to the x-axis, respectively. The rate of strain in the original frame is given by Eq. (2.10), and in the special frame will be of the form mentioned in Eq. (2.11):

$$E = \frac{\dot{\gamma}}{2}\begin{bmatrix} 0 & 1 & 0 \\ 1 & 0 & 0 \\ 0 & 0 & 0 \end{bmatrix} \tag{2.10}$$

$$E' = Q^T(\theta,\phi)EQ(\theta,\phi) \tag{2.11}$$

After rotating the E tensor into the special frame, using Eq. (2.4) the translational and rotational sphere velocities are calculated. Then, these velocities for each sphere are rotated back into the original frame using Eqs. (2.12) and (2.13), below.

$$U_{1\,or\,2} = Q(\theta,\phi)U'_{1\,or\,2} \tag{2.12}$$

$$\Omega_{1\,or\,2} = Q(\theta,\phi)\Omega'_{1\,or\,2} \tag{2.13}$$

While these rotations of frame involve extra computations, they use only second rank tensors, and save us the complication of expressing the third rank tensors $G_{ijk}^{(\alpha\beta)}$ and $H_{ijk}^{(\alpha\beta)}$ in an arbitrary frame, in which each tensor would contain 27 non-zero components.

2.2.2. Simulation details

To save computation time while preserving accuracy, a variable timestep is used that avoids sphere overlap, by requiring that the maximum decrease in the gap h between particles during a timestep is less than or equal to some fraction λ (usually 1/20) of the gap.

The general equation to determine timestep size for equal sized spheres is shown in Eq. (2.14). Neglecting HI, an upper limit for the decrease in gap between particles is obtained by adding the maximum possible decrease in gap due to the Brownian motion (first term on the left side) and shear flow (second term on the left side).

$$2\sqrt{3}\sqrt{\frac{6k_BT\Delta t}{3\pi(2a)\mu}} + \left|\dot{\gamma} y \cos\psi\right|\Delta t = \lambda h \tag{2.14}$$

Where k_B is Boltzmann constant, T is temperature, Δt is timestep size, μ is fluid viscosity, a is the sphere radius, $\dot{\gamma}$ is shear rate, y is the separation between the particle pairs in the shear gradient direction, and λh is the maximum distance that the particle is moved in a single timestep. The factor of $2\sqrt{3}$ in the first term on the left-hand side is to account for the fact that both spheres can diffuse in three orthogonal directions. The second term is a projection of the shear flow velocity onto the vector connecting the centers of the two spheres and ψ is the angle between this vector and the velocity vector of the shear flow at the location of sphere 2. Solving Eq. (2.14) yields the appropriate timestep size. Obviously, as particles get closer, the timestep size becomes smaller, but much time is saved by taking large steps when particles are far apart, while retaining accuracy.

To prevent the integration from taking too long when the spheres get very close, a cutoff shift distance is introduced (1 nm in this research). This means that when λh is less than 1 nm, 1 nm is substituted for λh in Eq. (2.14) before solving for Δt. Also, if the coefficient $\left|\dot{\gamma} y \cos\psi\right|$ is

less than 10^{-8} m/s, the equation is made easier to solve by removing this term and then solving the modified equation for Δt .

To determine binding times, two particles are placed randomly within the simulation box and the equations are integrated until a "collision" occurs, and the time to collision is recorded. Since hydrodynamic lubrication forces become singular when the particles come into contact, two methods are used to deal with this. For purely attractive potentials due to van der Waals interactions, the attractive force is singular at contact and this overcomes the singularity in the hydrodynamic force. As a second approach, for a combined attractive and repulsive potential with a secondary minimum, or in the absence of a singular attraction, a cut off distance is imposed close to the minimum in the potential (50 nm, unless stated otherwise) at which separation distance the particles are assumed to have aggregated, and the simulation is stopped at that point. Of course, when the potential is not singular, particle pairs will eventually separate due to hydrodynamic or Brownian forces, but for a reasonably deep minimum in potential at a distance away from the particle surface, binding can be long-lived enough to be considered "permanent," and hence cutting off the simulations at a pre-determined separation distance can be a reasonable approximation in some cases. Of course, in the absence of HI, particles simply collide, and the time of collision is taken from the point at which overlap first occurs.

For Janus particles with surface anisotropy, binding requires not only proximity, but also that the attractive sides face each other. Thus, simulating coagulation of Janus particles requires determination of relative orientation of spheres after each timestep, as well as particle positions.

At the end of each integration timestep, the origin of the coordinate system is translated to the center of one of the two spheres, the "test sphere" or sphere 1 at the center of the periodic simulation box. This eases the calculations, since it keeps the position of the test particle at zero, while the position of the second particle is updated accordingly. This method also assures that in the periodic domain, the closest particle to the test particle is always the second particle within the simulation box, and not any of its periodic images. Since in the dilute regime, the dynamics

are dominated by particle pairs only, this method also guarantees that the strongest two-body interaction with the test sphere is the one calculated. (Hydrodynamic interactions of the test sphere with periodic images of either sphere are not calculated, which is appropriate in the dilute-suspension limit.) If the second sphere passes through a wall of the box even after the test particle has been re-centered, then the test particle is re-introduced on the opposite face of the box.

For the case of periodic boundary condition in a shear flow, once a particle leaves the box in the velocity gradient direction and returns in the other side, it experiences a sudden shift in its longitudinal velocity. For the two-particle simulations, a dramatic effect of the periodic boundary condition for the velocity field is not expected, and so the simplest method is used, which allows a jump in velocity when crossing the boundary in the y direction. This was checked by also using the Lees-Edwards boundary condition[21] where once the particle leaves the simulation box in the velocity gradient direction, it will be placed on the other side with a different longitudinal position to account for the mentioned jump in velocity. Deviations of less than 5% were observed in the absence of HI between these two types of boundary conditions, showing that either boundary condition is able to impose an appropriate uniform concentration in the far field. For simulations of dense suspensions, it would be necessary, however, to use the Lees-Edwards boundary conditions.

The two particles were initially placed randomly inside the simulation box and then the equations were integrated until collision; a single "run" consists of a repetition of this around 2000 times, to obtain good averages of collision times and particle sampling of the simulation domain for a given shear rate. Simulations were performed using a computer cluster[22] and desktop computers. The duration of a run (as defined above) typically ranged from a few minutes (in the absence of HI) to several days (with HI) on a single processor. Due to the novel scheme implemented for the simulation boxes, which will be discussed later in the Results and Discussion Section, these run times represent a huge savings of computational time. Simulations were performed using a

constant temperature of $300K$. The viscosity of water at this temperature, namely $\mu = 0.865\times10^{-3}\ Pa.s$ was chosen, and the particle radius was chosen to be one micron for both particles ($a = b = 1\mu m$).

2.2.3. Error analysis

The standard error of the normalized binding times was calculated using Eq. (2.15):

$$e_r = \sqrt{\frac{1}{N_T(N_T-1)}\sum_{i=1}^{N_T}(\hat{t}_{V-i} - \bar{\hat{t}}_V)^2} \tag{2.15}$$

Where $\hat{t}_V$ is the binding time normalized by the zero-shear rate Smoluchowski limit in the absence of HI (Eq. (2.1)), N_T is the number of binding events (around 2000 in this study), and $\bar{\hat{t}}_V$ is average normalized binding time for the N_T binding events.

In the Results and Discussion section, it will be shown that to determine the normalized binding time for the infinite dilution, results are linearly extrapolated against inverse box length. Taking this linear extrapolation of the form $\hat{t}_V = m_1 + m_2 L_x^{-1}$, the total error ($e_T$) of normalized binding time for infinite dilution is calculated using Eqs. (2.16)-(2.18):

$$e_T = \sqrt{e_B^2 + e_i^2} \tag{2.16}$$

$$e_B = \sqrt{\frac{\sum_{i=1}^{N_B} e_r^2}{N_B}} \tag{2.17}$$

$$e_i = \sqrt{\frac{1}{N_B(N_B-2)}\left(\sum_{j=1}^{N_B}(\hat{t}_{V-j} - m_1 - m_2 L_{x-j}^{-1})^2\right)\frac{\sum_{i=1}^{N_B}(\hat{t}_{V-i})^2}{\sum_{i=1}^{N_B}(\hat{t}_{V-i} - \bar{\hat{t}}_V)^2}} \tag{2.18}$$

where e_B represents the standard error resulting from Brownian noise in the simulations amongst N_B data points, and e_i is the standard error for uncertainty in the intercept of fitting a linear line to data points using least square method. Also, N_B is number of different box sizes used to do an extrapolation towards infinite dilution.

As mentioned before, each run resulting in a binding event between two particles was repeated around 2000 times. After roughly 1000 collisions, the value of average binding time did not change dramatically, implying that 2000 repetitions were adequate enough to reduce the random noise. The error in the intercept of linear fit (e_i) contributes more to the total error than does Brownian noise (e_B). Error analysis shows that the total error in the binding time in the infinite dilution is generally between 1-5 %. For some cases (e.g. high shear rates), however, the error value can be as large as 8 %.

2.3. Results and discussion

2.3.1. No-flow case

In the absence of flow, only Brownian diffusion and the inter-particle potential affect particle motion.

2.3.1.1. Effect of hydrodynamic interactions on binding kinetics

The collision time for two equal-sized spheres in the infinite dilution limit and in the absence of flow, with HI, is calculated using the Smoluchowski solution:[6]

$$t_V = \frac{3\mu W}{8k_B T} \tag{2.19}$$

$$W = 2\int_{s_{cutoff}}^{\infty} \frac{\exp(U_P / k_B T)}{s^2 G(s)} ds \quad where \;\; s = \frac{2d}{a+b}, \;\; \frac{1}{G(s)} = \frac{A_{11}^{(\alpha\alpha)} - 2A_{11}^{(\alpha\beta)} + A_{11}^{(\beta\beta)}}{12\pi\mu a} \tag{2.20}$$

Here, μ is fluid viscosity, a and b are the particle radii, k_B is Boltzmann's constant, T is temperature, W is the "stability ratio," U_P is the interaction potential between the two particles, and d is center to center distance. Moreover, $G(s)$ is a hydrodynamic coefficient that represents the effects of HI in retarding the relative velocity of the two spheres. In the equation for the inverse of $G(s)$, the superscripts α and β on each matrix A identify the sphere (sphere 1 or sphere 2), and the numeric subscript "11" designates the first diagonal element of each 3×3 A matrix, which is the component governing resistance to changes in gap; i.e., squeezing motion, as discussed in previous paper published by Larson Group.[6]

As mentioned above, to avoid the singularity in the hydrodynamic functions that occurs at particle contact, a cut off distance can be introduced into the integral in Eq. (2.20) and into BD simulations. When the inter-particle distance becomes smaller than the cut off distance, a collision is deemed to occur. Taking 50 nm as the cut off distance, W is found to be 2.09 from the integration of Eq. (2.20), in the absence of an explicit interaction potential (i.e., $U_P = 0$). (The use of the cut off can be considered to represent the effect of a deep square well potential whose outer boundary lies at the cut off distance, so that there is no effect of the potential until it suddenly becomes very strong when the particle gap falls below the cut off.) Later in this project, a Hamaker attractive potential will be used, which becomes singular at contact and overcomes the repulsive singularity of the resistance matrix.

Figure 2.1 depicts the effect of inverse cubic box length L_x on normalized collision times for the case of no flow. For this case, cubic boxes with dimensions ranging from 100 to 700 μm are used and results are linearly extrapolated against $1/L_x$ to reach the infinite dilution limit.

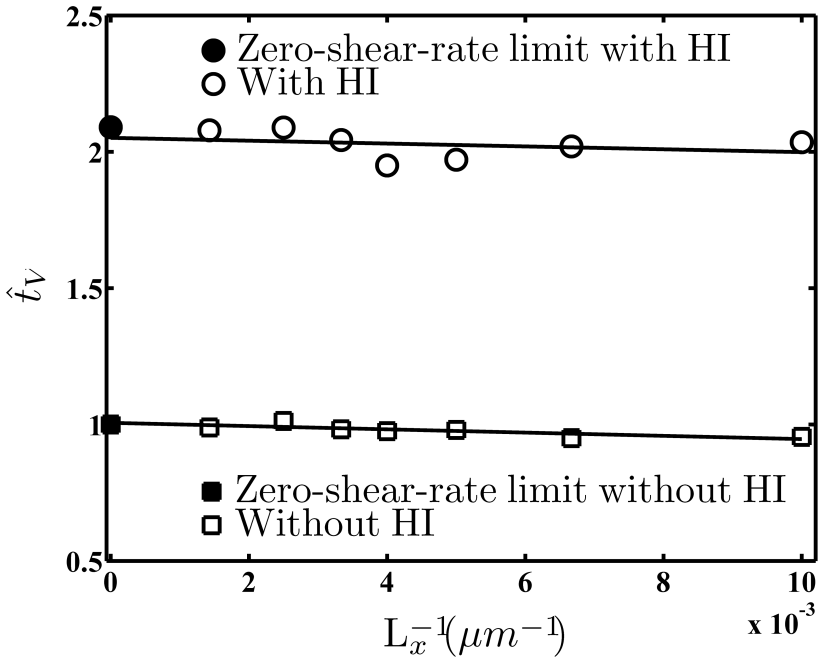

Fig. 2.1. Normalized collision times as a function of inverse cubic box length ($L_x = L_y = L_z$), in the absence of flow and no interaction potential. The limiting values at infinite box size are given by Eq. **(2.1)** for the absence of HI and Eqs. **(2.19)-(2.20)** with HI, where in the case of HI the particles are assumed to collide when the gap between them reaches 50 nm. Since the sphere radius is 1 μm, the numerical value of L_x in μm can also be taken to be box dimension made dimensionless with the particle radius.

The collision times, extrapolated to infinite dilution agree well with literature values both with and without HI (i.e., the Smoluchowski limits given by Eqs. (2.1) and (2.19)-(2.20)). The results show that HI slows down the binding of the particles, because of the strong lubrication resistance as the particles approach each other. The results in Fig. 2.1 also agree with the recent simulation results of Liu and Larson,[6] and are in fact based on the same method.

2.3.1.2. Induced-dipole attraction

The following expression can be used for the attractive Hamaker potential $U_{Hamaker}$ between equal-sized spheres, which is a singular function at particle contact.[13]

$$U_{Hamaker} = -\frac{A}{6}\left[\frac{2a^2}{d^2-4a^2} + \frac{2a^2}{d^2} + \ln\frac{d^2-4a^2}{d^2}\right] \tag{2.21}$$

Here d is the inter-particle distance, a is the particle radius, and A is the Hamaker constant, reflecting the strength of van der Waals interactions.[13]

The outer cut off distance, which is the gap distance above which effect of attraction of one particle on the other is taken to be negligible within the code, is set to 600 nm. The inner cut off distance is the gap below which particles are assumed to have collided. In the absence of flow, the collision time was found to be insensitive to the inner cut off distance, for cut off distances between 1 to 15 nm, which is a good indication of convergence of numerical method.

Figure 2.2 depicts the variation of the normalized binding time with inverse cubic box length in the presence of a Hamaker attractive potential, in the absence of flow, with HI. Using Eqs. (2.19)-(2.20), the predicted stability ratios are found to be 2.46, 1.9, and 1.38 for $A/k_BT = 0.1$, 1, and 10, respectively.

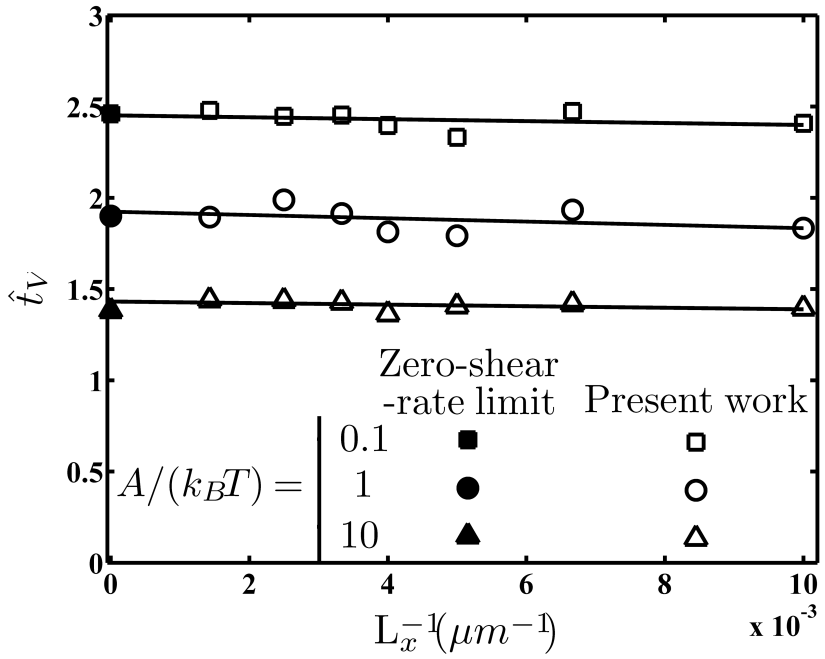

Fig. 2.2 Comparison of extrapolated binding time from simulations with theoretical predictions of Eqs. (2.19)-(2.21) for the presence of induced-dipole attraction, and HI.

Figure 2.2 shows good agreement of the extrapolated values of the simulated normalized binding time with theoretical predictions, and that binding time is reduced by 40% as $A / k_B T$ increases 100-fold from 0.1 to 10.

2.3.2. Shear flow

2.3.2.1. Implementation of rectangular simulation boxes

The strength of the shearing flow relative to particle diffusion is set by the Peclet number, given by:

$$\mathrm{Pe} = \frac{3\pi\mu a^3 \dot{\gamma}}{k_B T} \tag{2.22}$$

Figure 2.3 shows the normalized concentration profile of the second particle in the central xy plane (where $z = 0$) at a high Pe, where, as mentioned earlier, the coordinates are centered on the first particle's center. The concentration profile was obtained by binning particle positions in cubic cells of dimension equal to one particle radius. This profile is for a cubic box in which $L_x = L_y = L_z = 100\,\mu m$. As can be seen, there is a low-particle-concentration "shadow" of roughly cylindrical shape, oriented in the flow direction. When the particle enters this region, collision with the test sphere occurs very quickly, when flow is fast (i.e., high Pe). But outside this region the particle spends much of its time repeatedly shooting across the periodic box. It is physically realistic for a depletion "shadow" to exist downstream of the test particle at high Pe. However, the shadow upstream of the particle (where "upstream" is at negative x for $y > 0$ where the flow is in the positive direction, and is at positive x for $y < 0$, where the flow is in the negative direction) is an artifact of the periodic boundary conditions. No simple way could be found to introduce fresh particles into the upstream side of the box that would be robust to changes in Pe, and would not suffer artifacts arising from the variation of velocity across the

upstream surface of the box, and the presence of corners and sides of the box through which particles can diffuse. Periodic boundary conditions on all sides of the box seem to be the safest way to attain a far-field concentration of unity, when the box becomes asymptotically large. However, to approach the large-box limit at high Pe where the downstream depletion shadow becomes highly elongated, the box must become very long in the x direction, and cubic boxes become so voluminous that collisions become unreasonably rare. Under fast shear, the collision time is controlled by the time required for the second particle to diffuse into the cylindrical shadow region. This suggests the use of rectangular boxes (Fig. 2.4, a) with box length much larger than its width and height, so that the particle can diffuse into the shadow region faster, to both establish a uniform concentration far upstream of the test sphere and to accelerate collisions. Figure 2.5 reveals that the shadow is indeed obviated in a long rectangular box. While the concentration field in Fig. 2.5 is noisy because of the stochastic nature of the simulations, and binning approximation, it will be shown that an accurate estimate of the collision time is nevertheless obtained.

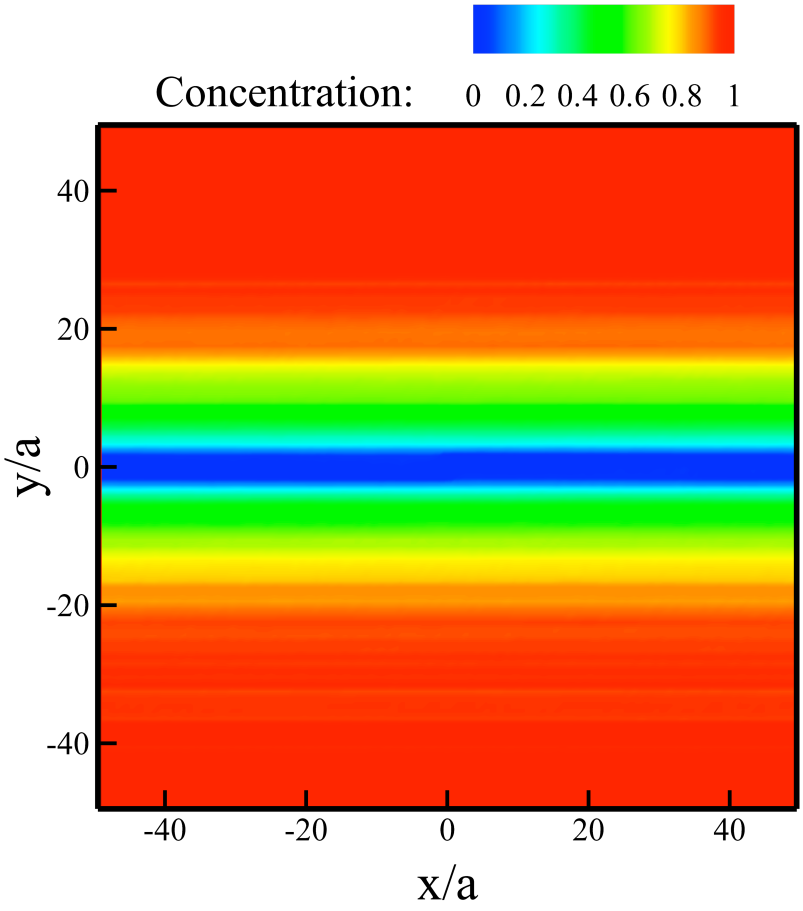

Fig. 2.3. Particle concentration field, normalized to unity on average, for the central xy plane, depicting the shadow effect, for $Pe = 295$, without HI, and binning resolution=1 μm. Here a is the particle radius.

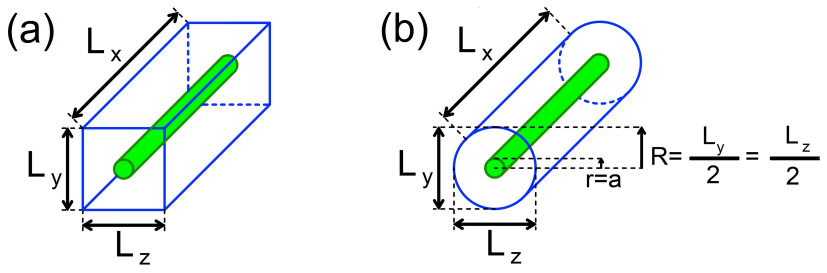

Fig. 2.4. (a) A rectangular box used to overcome the shadow effect, which in (b) it is approximated by a cylindrical domain for estimating the collision time, as described in the text.

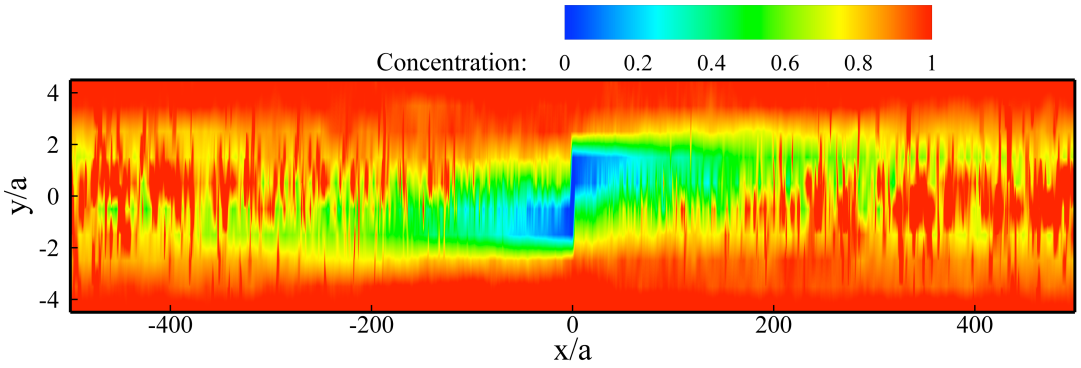

Fig. 2.5. Normalized concentration field for a long rectangular box for $Pe = 295$, without HI, and binning resolution=1 μm.

As shown in Fig. 2.4b, to roughly estimate the collision time for a rectangular box in which the rate-limiting step for collision is lateral diffusion into the shadow region, the rectangular box is replaced with a cylindrical domain, and the diffusion equation in cylindrical coordinates is solved assuming negligible variation in concentration along the angular and longitudinal directions (Eq. (2.23)). The effect of convection is accounted for by assuming that a particle will quickly collide with the test sphere once it has diffused into the inner "shadow" cylinder with radius equal to that of the test sphere. With boundary conditions of uniform concentration in the far field ($R = L_y / 2$), and zero concentration at the edge of the shadow ($R = a$), the collision flux and binding time are

calculated using Eqs. (2.24) and (2.25) below. While Eq. (2.25) provides a rough estimate, its accuracy should improve as the box width increases.

$$0 = \frac{1}{r}\frac{\partial}{\partial r}\left(r\frac{\partial n}{\partial r} \right), \tag{2.23}$$

$$Collision\ flux = \frac{\#collisions}{time \times area} = D\frac{\partial n}{\partial r} = \frac{Dn_0}{a\ell n(\frac{L_y}{2a})} \tag{2.24}$$

$$t_V = \frac{\ell n(\frac{L_y}{2a})}{2\pi D}\frac{1}{L_x} \tag{2.25}$$

In the above formulae, n is the concentration of the second particle, D is the diffusion coefficient, and the "*area*" used to compute the collision flux is that of the cylindrical shadow region (= $2\pi aL_x$). Equation (2.25) indicates that for rectangular boxes that are too short to allow collisions to occur before the particle has crossed by length of the box, the dimensionless collision time per unit volume is inversely proportional to the box length, as is confirmed in the simulation results in Fig. 2.6. Furthermore, Eq. (2.25) shows that slopes of lines of normalized collision time vs. L_x^{-1} should be proportional to $\ln(L_y / 2a)$, which is in fact also demonstrated to hold, in the inset to Fig. 2.6.

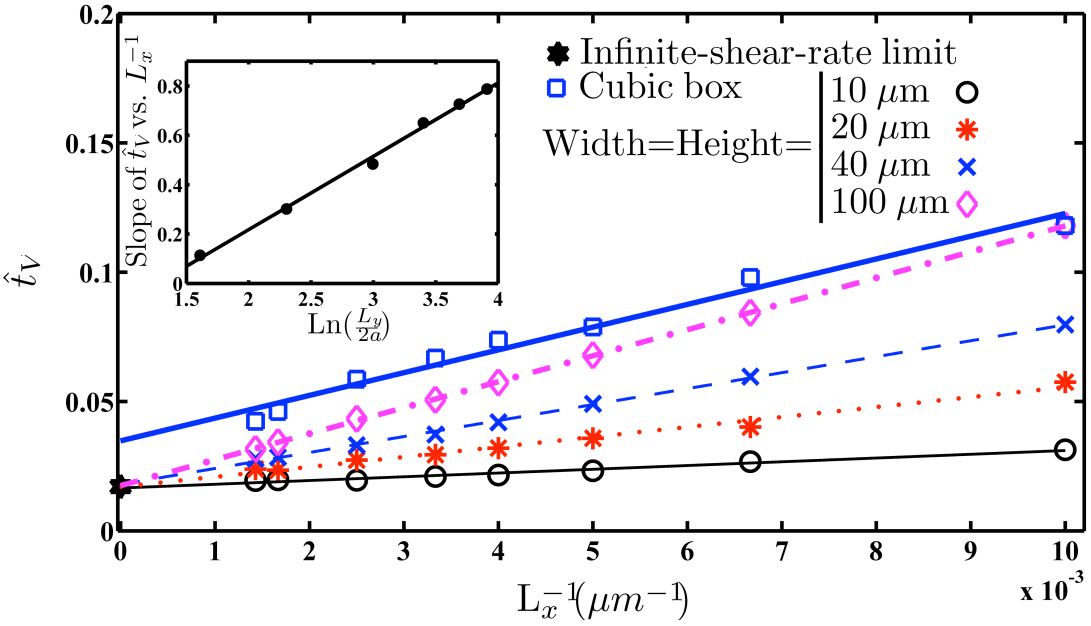

Fig. 2.6. Comparison of simulated normalized collision times for $Pe = 138$ in cubic and rectangular boxes, and their approach to the Smoluchowski orthokinetic limit. Inset shows the dependence of the slope of lines in the main figure for rectangular boxes vs. $\ell n(L_y / 2a)$.

Figure 2.6 shows that for cubic boxes, the plot of normalized binding time versus inverse box length is nonlinear, making extrapolation to infinite box size difficult. For rectangular boxes, however, the plots are linear, and the extrapolated values for all box widths converge to expected infinite-shear-rate Smoluchowski limit. (Data for box widths of 60 and 80 μm follow the same trend but are omitted for clarity.) So it appears that using rectangular boxes can counteract the adverse effect of the longitudinal shadow. (Later it will be shown that when the Pe becomes extremely large (> 300), the ratio of box length to its width or height has to be increased even further to obviate the shadow.)

Since for rectangular boxes, predictions for different box widths approach the same infinite-shear-rate Smoluchowski limit as the box is elongated, to save computational time a relatively narrow 20 μm width is used for simulations of binding kinetics in all flows with strength of about $15 < Pe < 300$.

For smaller shear rates ($Pe < 15$), however, as the box length is increased, an upturn appears in the plot of collision time vs. L_x^{-1}. This upturn occurs at ever-smaller box lengths as the shear rate decreases. As the box width is increased, however, the upturn is postponed to larger box lengths, as shown in Fig. 2.7. Thus, to minimize the effects of the upturn, for lower shear rates, simulations are carried out for larger box width (i.e. 40 μm). Also, with the exception of extremely fast flow with van der Waals inter-particle attraction, which will be discussed shortly, simulation results for very long boxes ($L_x > 700\,\mu m$) are ignored to allow a fit of a straight line to the simulation data to obtain the extrapolated value of the collision time.

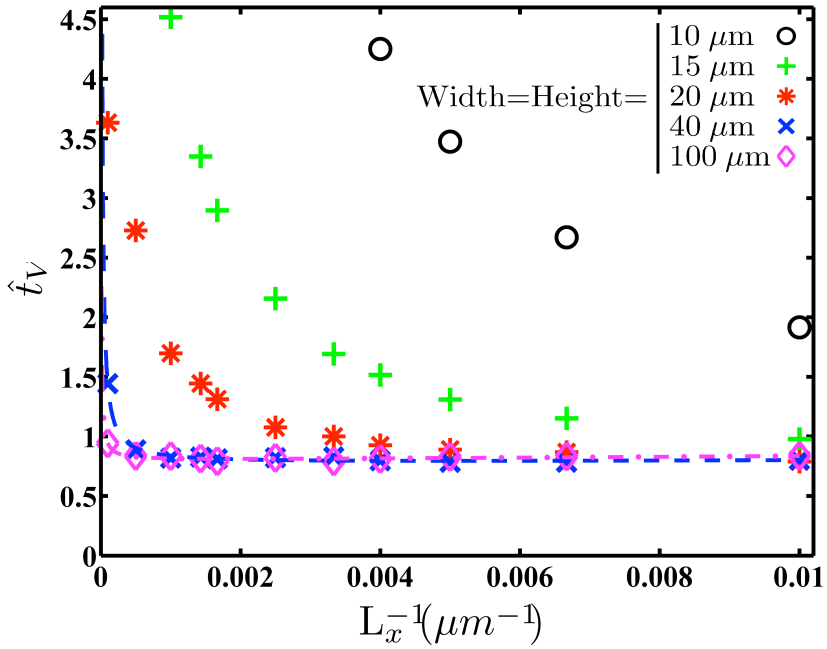

Fig. 2.7. The "upturn" in binding time as the box becomes very long for different box widths, at a small shear rate ($Pe = 0.15$). Empirical fits for simulation boxes with widths of 40 and 100 μm shown in the figure are $\hat{t}_V = 0.768 + 2.629L_x^{-1} + 6.702\times10^{-5}L_x$ and $\hat{t}_V = 0.797 + 3.717L_x^{-1} + 1.463\times10^{-5}L_x$, respectively. Particles have a radius of 1 μm.

As can be seen in Fig. 2.6 for all box widths, and in Fig. 2.7 for box widths greater than 20 μm, for L_x below a critical value (i.e., large enough L_x^{-1}), lines of normalized collision time for rectangular boxes are linear, and can be fit by $\hat{t}_V = m_1 + m_2 L_x^{-1}$. Also for very large L_x (small

L_x^{-1}), where the normalized collision time dramatically increases, the upturn can be fit to the formula $\hat{t}_V = m_3 / L_x^{-1}$. So the expression $\hat{t}_V = m_1 + m_2 L_x^{-1} + m_3 / L_x^{-1}$ is able to fit the simulation results with the constant m_1 giving the extrapolated value of the collision time at infinite dilution without the effect of the upturn. Examples of this fit are shown for the simulation results in Fig. 2.7 for box widths of 40 and 100 μm. This fit seems to work for most of simulation cases. In the rest of this chapter however, a linear extrapolation scheme is pursued, in which data for high L_x where the upturn occurs is omitted. Similar results are obtained, however, if the upturn is also fitted using the above empirical formula, except for extremely high shear rates discussed below.

To explore the cause of the upturn for very long boxes and low shear rates, Fig. 2.8 shows the normalized concentration contours in the central xy plane for a very long rectangular box, in the absence of flow. The box dimensions ($L_x = 1000\,\mu m$, $L_y = L_z = 10\,\mu m$) are chosen such that the resulting collision time will be in the upturn region.

Fig. 2.8 clearly shows that when the aspect ratio becomes very large, a depletion slab appears around the test sphere, extending across the entire box in the y direction, and the z direction as well (not shown). This depletion slab is a consequence of the periodic boundary conditions. The second particle, when it is a great distance along the x axis away from the test particle, and flow is absent or slow, takes a much longer time to diffuse to the plane containing the test particle and its periodic images in the yz plane, than it does to diffuse within that plane to the nearest periodic image. Hence the second particle sees the array of periodic images of the test particle as a single absorbing slab. The diffusion time thus becomes very long, since the test particles towards which the second particle must diffuse are much farther away, on average, than would be the case for randomly distributed particles, or for a particle in a cubic box and its periodic images. In other words, as the result of periodic images along the relatively small y and z directions, there is a lateral “shadow” that extends laterally across the box and prevents the attainment of the

far-field uniform concentration at large y or z. As the shear rate is increased, the influence of diffusion is reduced compared to longitudinal convective motion, and the upturn is postponed to larger aspect ratios.

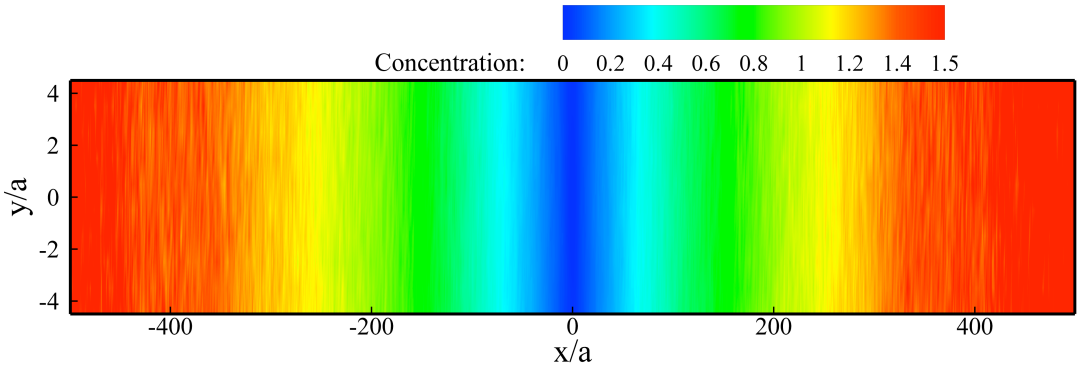

Fig. 2.8. Normalized concentration contours for the central xy plane in a rectangular box with aspect ratio of 100, $Pe = 0$, without HI, and binning resolution=1 μm.

Thus, while the longitudinal convective shadow is counteracted by lengthening the box in the x direction, this can eventually create a lateral diffusive shadow in y and z directions. So, the box length and width should be chosen to keep both shadows minimal. To wipe out the longitudinal shadow, the time for convection across the length of the box must be longer than the time required for lateral diffusion across the box. For long boxes, the time for convection across the box is dominated by the period of time that the particle is relatively close to the shadow region where the particle velocity is low; hence the convection time is of order $L_x / (a\dot{\gamma})$. The time required for the sphere to diffuse across the box width is of order L_y^2 / D, where D is the sphere diffusivity. Thus, the condition for removing the longitudinal shadow is $L_y^2 / D << L_x / (a\dot{\gamma})$. In terms of Peclet number (Eq. (2.22)), this condition is expressed as:

$$\frac{L_y}{a} << \left(\frac{L_x}{a} \times \frac{1}{Pe}\right)^{0.5} \tag{2.26}$$

On the other hand, to minimize the diffusive shadow in the lateral directions, $L_y = L_z$ should be chosen large enough that the particle cannot diffuse over the entire y direction in the time it takes to convect along the box. If the particle can diffuse in this time, then the depletion zone around one sphere will be affected by the loss of particles due to collisions with a periodic image of the sphere separated by a distance L_y in the y direction. This condition is just the opposite of the condition given by Eq. (2.26). So, minimizing both shadows simultaneously does not seem possible. However, since these equations are scaling laws, their prefactors could be quite different, making it possible to find an optimal range of box geometries that minimizes both shadows and allows extrapolation to an accurate solution. In fact, in the subsequent sections, it will be shown that for each Pe value, it is possible to find a range of box aspect ratios for which the effects of both shadows are minimal. In addition, it will be shown below that as the box width is increased, with box aspect ratio held within a specified range, the simulation results converge, and for fast and slow flows they converge to known asymptotic results.

Figure 2.9 shows the normalized concentration profile of the second particle in the central yz plane. This contour map is for a rectangular box where $L_x = 1000\,\mu m$, $L_y = L_z = 10\,\mu m$. In order to increase the resolution, the bin size in the y and z directions have been reduced to 0.2 μm. On the other hand, for the sake of decreasing the binning noise, bin thickness has been kept 1 μm in the x direction. This figure indicates that the diffusive shadow in the z direction plays a more important role than its counterpart in the y direction. Apparently the gradient of shear in the y direction makes the concentration profile more uniform in that direction compared to z.

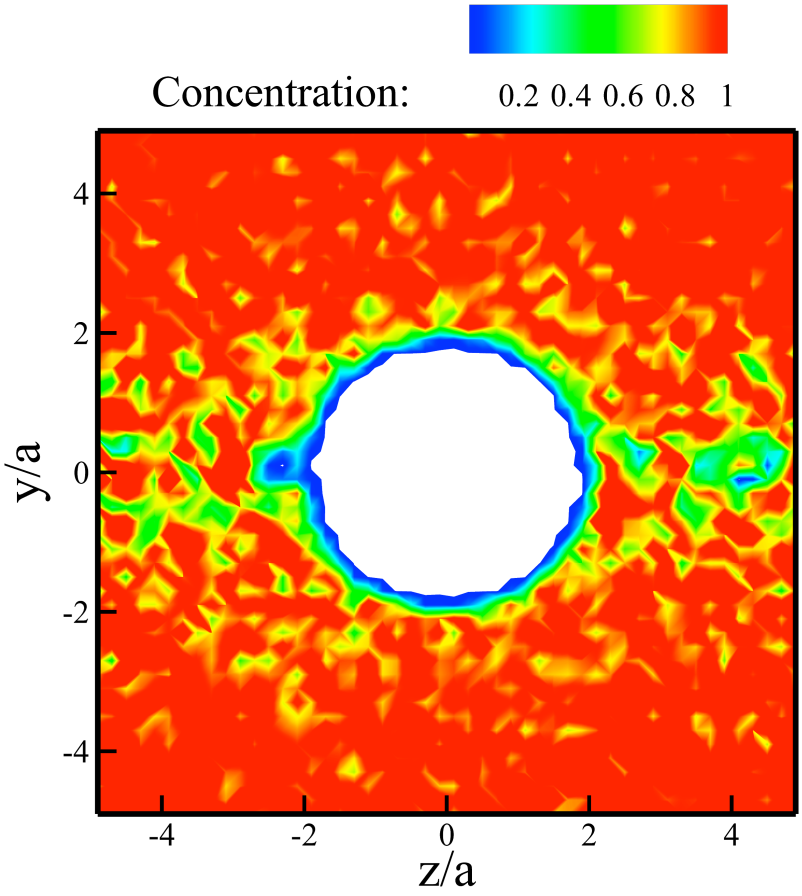

Fig. 2.9. Normalized concentration contours in the central yz plane, with $Pe = 295$, without HI, and binning dimension of 0.2 μm in y and z directions.

2.3.2.2 Particle trajectories with HI

When HI is considered, the motion of one particle affects the motion of the other. The accuracy of treatment of HI is tested by turning Brownian motion off, and comparing particle trajectories in Fig. 2.10 from our code with results published previously.[23,24] In Fig. 2.10a, particles are initially placed such that the distance between the centers of spheres is 10 sphere radii in the longitudinal direction and 0.4 sphere radii in the lateral direction (Although in order to enhance clarity, a more restricted longitudinal range is shown in this figure). In Fig. 2.10b, the initial longitudinal distance is 6 sphere radii, while the lateral distance is varied from 0.8 to 2.4 sphere radii. Figure

2.10 indicates nearly perfect agreement between particle trajectories predicted by the present research with those previously determined using boundary element methods.[23,24]

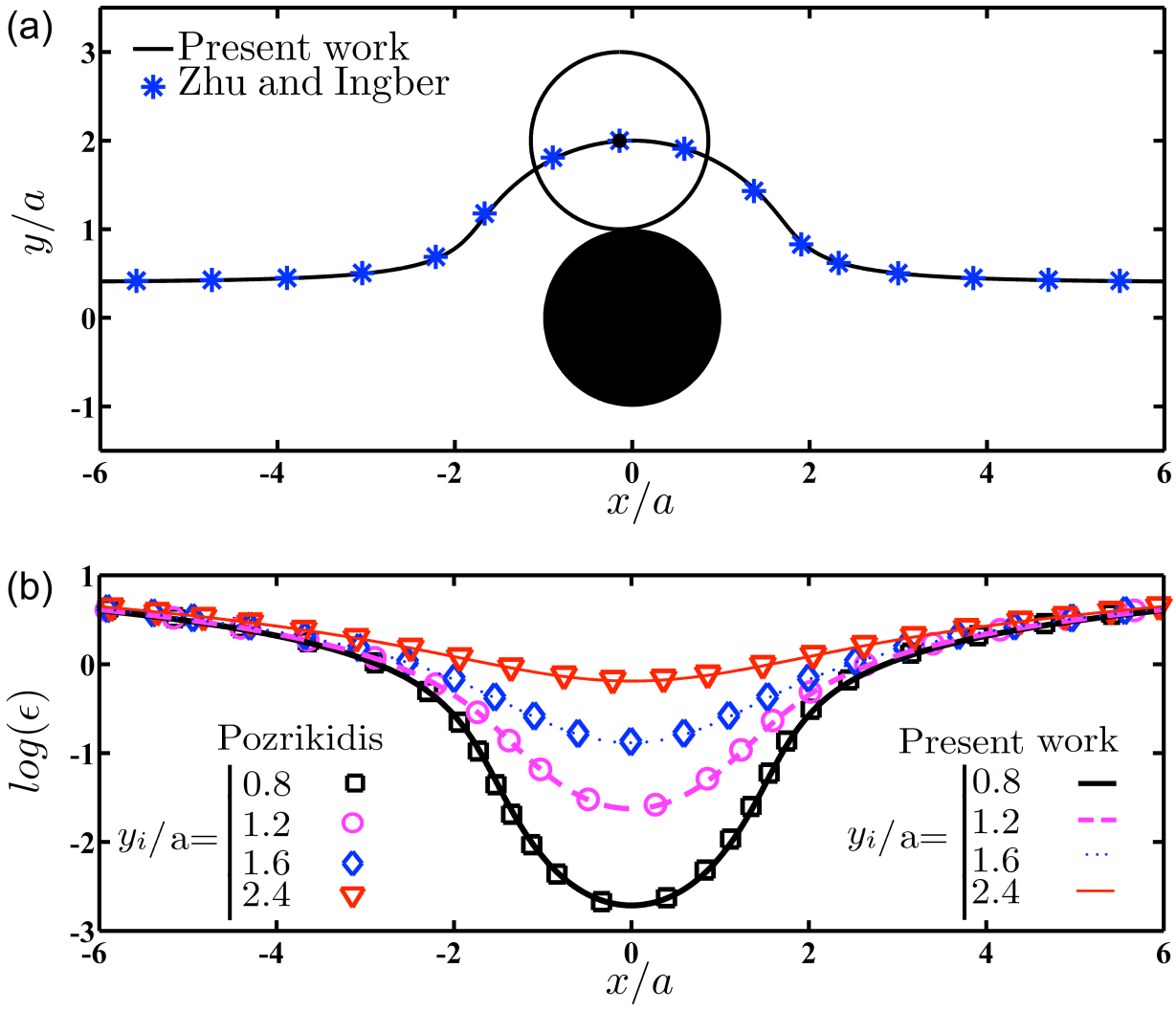

Fig. 2.10. Simulated particle trajectories. (a) Coordinates ($x.y$) of the second particle position in shear flow in a frame in which the origin moves with the test particle, compared with the trajectory from Zhu and Ingber.[23] Test particle is shown with a closed circle, and second particle by an open circle. (b) The logarithmic variation of ε, gap normalized by the sphere radius a, vs. second particle longitudinal position compared with results of Pozrikidis.[24] The particles are all placed in the xy plane, with $z = 0$.

Table 2.1 compares relative velocities of particles scaled with $\dot{\gamma}a$ (where $\dot{\gamma}$ is shear rate and a is particle radius) from the present work with theoretical predictions reported from a high order expansion that includes both lubrication and far-field contributions, tabulated by Pozrikidis.[24] It should be noted that in this case particles are placed at the same x coordinate but separated in the

velocity gradient direction by a gap of $h = \varepsilon a$. Table 2.1 shows that relative velocities of particles reported here are close to the higher order analytical solution.[24] The reason for slight difference between the present work and those of Pozrikidis is that the high-order solution is derived from a 12th order far-field expansion and a higher-order lubrication solution than the solution drawn from Jeffrey and Onishi[18] used in the current study.

Table 2.1. Particles relative velocities scaled with $\dot{\gamma}a$ as a function of non-dimensionalized gap (ε) compared with analytical values given by Pozrikidis.[24]

ε	0.05	0.001	0.0001	0.00001
$\hat{V}_y$ (Present work)	0.9339	0.8639	0.8510	0.8430
$\hat{V}_y$ (Analytical solution[24])	0.9237	0.8555	0.8424	0.8343

2.3.2.3. Binding kinetics in the absence of hydrodynamic interactions

Although there are many studies of shear-induced particle doublet formation in the absence of HI,[11,12] the Pe range covered has been limited. Here simulation results for doublet formation in the absence of HI are presented over the complete range of Pe values, both to supply a comprehensive set of results and to validate our simulation results against previous studies. The predicted normalized collision times in the infinite dilution limit for a wide range of Pe number are shown in Fig. 2.11.

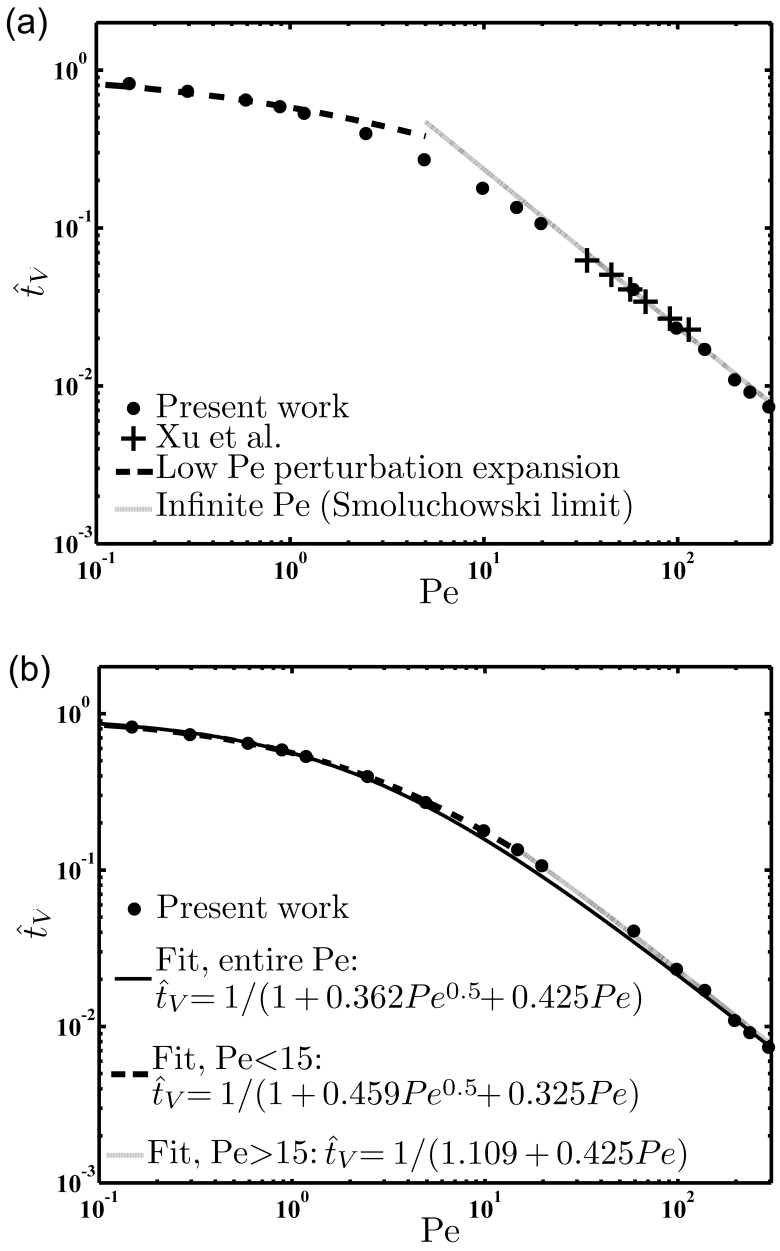

Fig. 2.11. Dependence of normalized collision time on Pe in the absence of HI. (a) Comparison with Smoluchowski limit,[12] with low-Pe formula of van de Ven[25] and with simulation results of Xu et al.[11]. (b) Fits for entire and partial ranges of Pe.

Fig. 2.11-a shows that as Pe becomes small, the simulation results approach the perturbation prediction of Van de Ven[25] namely:

$$\hat{t}_V = \frac{1}{1 + 0.5136\alpha_P (2\,\mathrm{Pe})^{0.5}} \tag{2.27}$$

In this equation, α_P represents the perikinetic capture efficiency, which in the absence of HI is just $\alpha_P = 1$. It should be noted that due to a difference in the definition of Pe, a factor of 2 appears in Eq. (2.27) compared to the relation given by Van de Ven.[25]

In addition, Fig. 2.11-a shows that for larger shear rates, the simulations results agree with those reported by Xu et al. obtained from the initial slope of the particle pair formation rate in simulations with thousands of particles.[11] Moreover, this figure illustrates that for $Pe > 60$, the extrapolated values of the normalized binding time are practically indistinguishable from infinite-shear-rate Smoluchowski limit (Eq. (2.2)). As a result, carrying out simulations of higher Pe values was not needed. Later, when the effects of HI with attractive inter-particle forces are considered, to attain the asymptotic limit for orthokinetic coagulation, it will be shown that it is essential to further increase Pe.

Equation (2.2) shows that the collision time scales with $1/(m_6 Pe)$ when Pe is very large, while Eq. (2.27) indicates that it scales with $1/(m_4 + m_5 Pe^{0.5})$, when Pe is very small. Combining these two equations to get an expression for the whole curve results in $\hat{t}_V = 1/(m_4 + m_5 Pe^{0.5} + m_6 Pe)$. Taking the constants "$m_4$" and "$m_6$," from the values for the zero-shear and infinite-shear-rate Smoluchowski predictions, and treating m_5 as a fitting parameter, yields $\hat{t}_V = 1/(1 + 0.362 Pe^{0.5} + 0.425 Pe)$, which is given by the solid black line in Fig. 2.11-b. This expression provides an approximate formula for the whole range of Pe in the absence of HI, and is especially accurate for very low and very high shear rates. A more accurate formula for low Pe values ($Pe \le 15$) is $\hat{t}_V = 1/(1 + 0.459 Pe^{0.5} + 0.325 Pe)$ while for high Pe values ($Pe \ge 15$), the expression $\hat{t}_V = 1/(1.109 + 0.425 Pe)$ is accurate, as shown in Fig. 2.11-b.

2.3.2.4. Normalized collision time in the presence of HI

Few studies have considered the effect of full HI on shear-induced coagulation of colloids,[14] and those that have done so have been generally limited to a very restricted range of Pe values. Figure 2.12 presents the normalized collision time computed from the simulations performed in this research as a function of Pe with HI but no inter-particle interaction. Instead, an inner cut off distance for "collision" is set at 50 nm. Comparing Figs. 2.11 and 2.12, one can conclude that in shear flow, HI slows collision times and coagulation by a factor of around 2 at low shear rates and around 3 in the high-shear rate limit, using this cut off criterion for coagulation. Figure 2.12 also shows agreement with the low-Pe perturbation expansion for very low Pe values (Eq. (2.28)).[14] It should be noted that for this prediction W is calculated using Eq. (2.20), and is found to be 2.09, using the cut off distance of 50 nm.

$$\hat{t}_V = \frac{W}{1 + 0.257 \dfrac{Pe^{0.5}}{W}} \tag{2.28}$$

Similar to results in the absence of HI, an expression of the form $\hat{t}_V = 1/(0.488 + 0.165Pe^{0.5} + 0.115Pe)$ shows good agreement with simulation results over a wide range of Pe numbers.

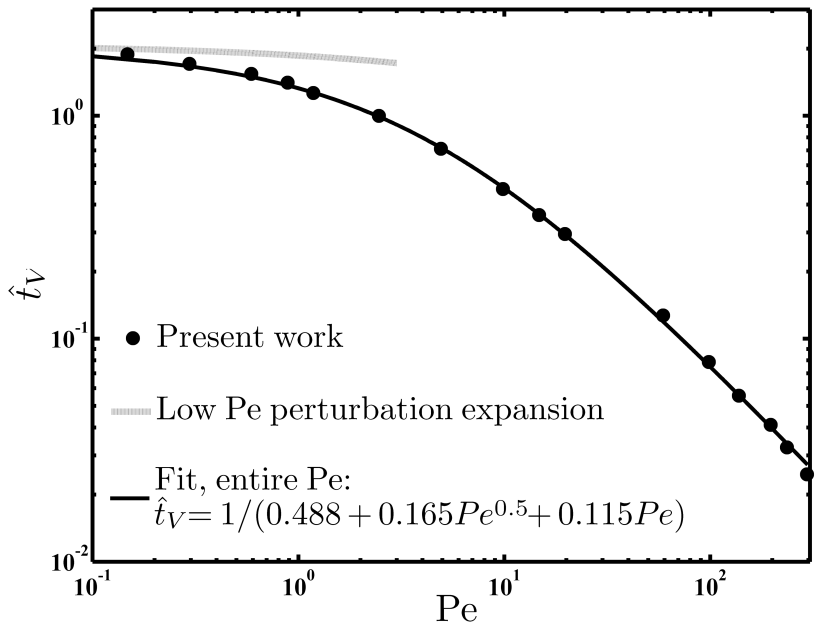

Fig. 2.12. Dependence of normalized collision time on Pe with HI. The line shows the low-Pe perturbation result from Russel et al.[14]

2.3.2.5. Influence of inter-particle forces on coagulation kinetics

2.3.2.5.1. Induced dipole attraction

With inclusion of a Hamaker attractive potential, for the case of no flow, good agreement between simulation results and theoretical predictions was observed in Fig. 2.2. The asymptotic limit with a Hamaker potential for extremely high shear rates has been reported for fixed values of the "flow number" (called fl hereafter), which is the ratio of flow strength to attractive potential, as defined in Eq. (2.29), given below.[13] To maintain the fl constant with increasing *Pe*, the Hamaker constant must also be increased proportionally. Figure 2.13 compares the dependence of extrapolated values of the collision time multiplied by Pe for different box widths to an asymptotic solution reported by Feke and Schowalter[13] for fl of 1000.

$$fl = \frac{6\pi\mu a^3}{A}\dot{\gamma} = \frac{2k_B T}{A}Pe \tag{2.29}$$

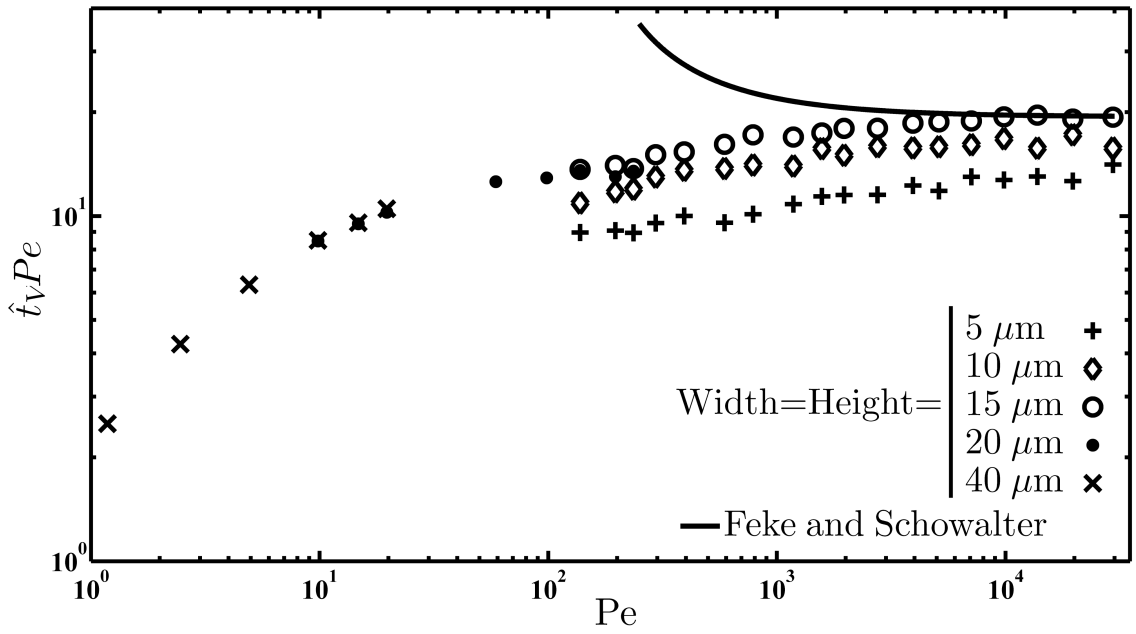

Fig. 2.13. Comparison of simulation results with those reported by Feke and Schowalter[13] for fl of 1000. For box width 20 μm and 40 μm, a fixed box length range (from 100 to 700 μm) was used, while for the other box widths, the box length range was varied to avoid the shear-induced shadow effects. Overlaps between simulation results, while box width is varied from 15 to 20 μm, and 20 to 40 μm is shown.

It should be noted that since Pe values are extremely high in this case, the aspect ratio of rectangular boxes must be made especially large, or the longitudinal shadow will corrupt the results; for example, for a Pe value of 30,000 even a box aspect ratio of 1000 is not large enough. So, to avoid the adverse effect of the shadow for high Pe values the box length should be set long enough that the particle has time to diffuse into the shadow and obviate it. However, if the box length is chosen too long, the lateral shadow produces an upturn in binding times vs. L_x^{-1}. So a range of box lengths spanning from approximately one third of the box length at which the upturn begins to the onset of the upturn is chosen to minimize the effects of both shadows at a typical high Pe value. Also, with variation of shear rate or box width, the range of box lengths is varied according to the scaling given in Eq. (2.26). For a fl of 1000, due to increased convection of fluid, it was necessary to decrease the inner cut off distance at which binding is deemed to occur from 15 to 1 nm to get converged results.

According to Fig. 2.13, as Pe is increased, the deviation between the simulation results and those predicted by Feke and Schowalter[13] decreases. Also, for extremely high Pe values (> 10^4), the slope of the simulated values of the aggregation time multiplied by Pe approaches the asymptotic horizontal line limit (zero slope) on a log-log plot.[13] Furthermore, this figure shows for box widths of 5 to 15 μm, a wider box gives results more closely approaching the asymptotic predictions at very high shear rates. This provides confidence that as the box width is increased, the results approach the infinite dilution limit. This suggests that the effects of the convective and diffusive shadows can eventually be overcome by increasing box size while choosing box shape to minimize errors of both longitudinal and lateral shadows.

For low and intermediate Pe values, the longitudinal shadow for rectangular boxes is not as serious an issue as it is at the higher Pe. One can see this in Fig. 2.13 by noting that for Pe in the range 100-200, the results for boxes of width 15 and 20 μm are almost identical. It should be noted that in this figure the results with box width of 20 μm were obtained using the previously specified fixed box length range from 100 to 700 μm, while for a box width of 15 μm, the box length was varied as described above. So for smaller Pe values, it is possible to return to the previous method of using the fixed box length range from 100 to 700 μm. As shear rate is further reduced, the lateral shadow begins to play a significant role and an upturn in collision time tends to corrupt a larger portion of the simulation data. To solve this problem, as before, the box width is further increased to 40 μm in order to postpone the effect of the lateral shadow (See Fig. 2.13).

Feke and Schowalter[13] performed a perturbation expansion to solve for the asymptotic high-shear-rate limit of coagulation with induced-dipole attraction, i.e., using the Hamaker potential given in Eq. (2.21). Their asymptotic solution yielded an expression for the aggregation time that included a zeroth and first order term in the aggregation rate, which can be written in terms of the aggregation time in the form $t_V = Pe/(m_7 + m_8 Pe)$, and thus is only valid at high shear rates. Here the constants m_7 and m_8 are both functions of the fl. The presented BD simulation method

is able to simulate shear flows at arbitrary Pe numbers, and the results over the whole range are plotted in Fig. 2.14 with the Hamaker potential at two different fl values. As described before, for high Pe, the box width is set to 15 μm, but as Pe is decreased and the transverse shadow starts to become important, the box width is increased. For example, to obtain Fig. 2.14, for fl=1, a box width of 20 μm was used for $15 < Pe < 138$, and a box width of 40 μm, for $Pe < 15$.

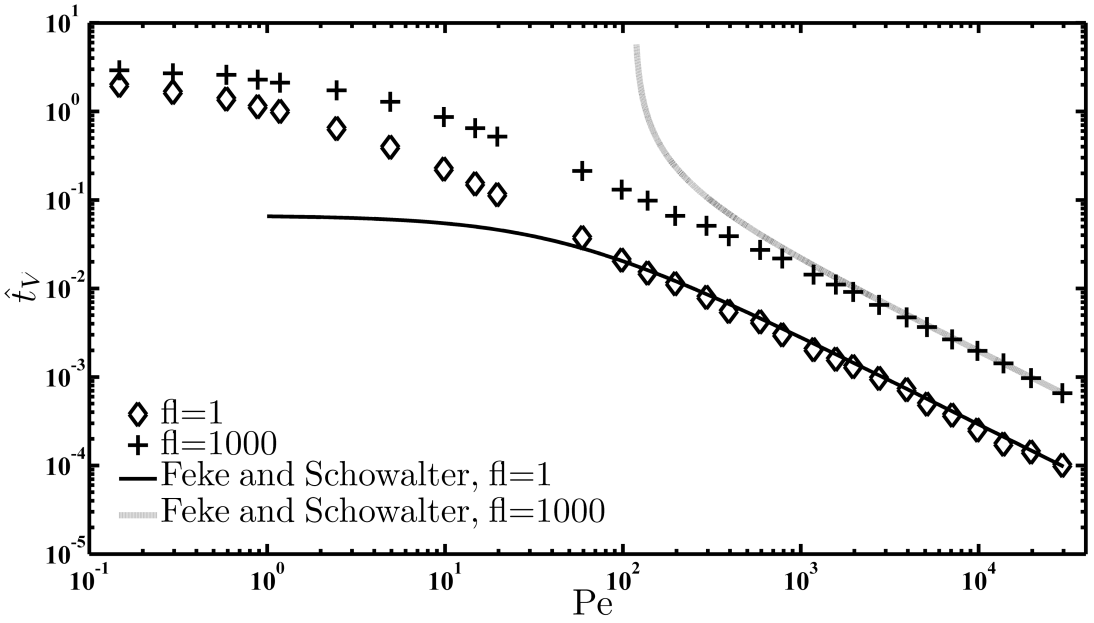

Fig. 2.14. Simulation results over the entire range of Pe with induced-dipole attraction at two different fl values, along with asymptotic results from Feke and Schowalter.[13]

According to Fig. 2.14, as Pe is reduced, the relative deviation between normalized binding times for different fl values decreases. As stated earlier, to keep the fl constant, the Hamaker constant is varied in proportion to *Pe*. Thus, for very small Pe values, the Hamaker constant is reduced so much that it has only a minor effect on the aggregation time. Also, the Feke and Schowalter results deviate from the numerical results as Pe drops below 10^2, and the deviations are in opposite directions for fl of 1 and 1000, because of the opposite signs of the m_7 term for $fl = 1$ and 1000 in the Feke and Schowalter perturbation expression given above. Of course, the

diverging aggregation time for $fl = 1000$, resulting from the negative value of m_7 in the Feke and Schowalter results is invalid at Peclet numbers below around 200. The numerical results show little indication of a change in sign of the coefficient m_7 when fl increases from 1 to 1000, indicating that the first order term with coefficient m_7 in the asymptotic expansion of Feke and Schowalter has a very limited range of applicability. To our knowledge, the results in Fig. 2.14 represent the first determination of the range of applicability of the now-classic Feke and Schowalter analysis of particle coagulation in sheared dilute suspensions.

2.3.2.5.2. Electrostatic repulsion and depletion attraction

Next, a potential composed of an electrostatic repulsion (Eq. (2.30)) and a depletion attraction (Eq. (2.31a)) is implemented in the simulations.

$$U_{electrostatic} = \frac{2\pi ab}{a+b} 64 k_B T n_\infty \gamma^2 \kappa^{-2} e^{-\kappa h} \tag{2.30}$$

$$U_{depletion} = -n_p k_B T V_{overlap} \tag{2.31a}$$

$$V_{overlap} = \begin{cases} 0, & d > a+b+2r_p \\ \dfrac{\pi(R+r-d)^2(\mathrm{d}^2+2d\,\mathrm{r}-3\mathrm{r}^2+2d\,\mathrm{R}+6\mathrm{rR}-3R^2)}{12d}, & d \le a+b+2r_p \end{cases} \tag{2.31b}$$

$$R = a + r_p, \quad r = b + r_p, \quad d = a + b + h \tag{2.31c}$$

In the above, a and b are particle radii, k_B is Boltzmann's constant, T is temperature, γ is the reduced surface potential (=0.589), $1/\kappa$ is the Debye length (=6.8 *nm*), and n_∞ represents the number density of ions in the solution ($=12.04\times10^{23}\ \#/m^3$). Moreover, r_p is the depletant radius (=100 *nm*), n_p is the depletant number density ($=7.30\times10^{20}\ \#/m^3$), h is the gap distance, and $V_{overlap}$ is the gap-dependent volume of overlap of the two spheres.[6] The values of the above

parameters given in parentheses were chosen so that the total potential energy (Eq. (2.32)) has a minimum at the selected inner cut off distance that was used earlier in the absence of a potential (=50 *nm*). The potential depth at this minimum using these parameters is determined to be $25.2 k_B T$.

$$U_{total} = U_{electrostatic} + U_{depletion} \tag{2.32}$$

Figure 2.15 shows the dependence of the normalized collision time on Pe in the presence of this potential. Also shown is the normalized binding time in the absence of an explicit potential but with the cut off distance set to the location of the minimum in the potential, namely at 50 *nm*, and more limited results for a cut off set to 25 and 100 *nm*.

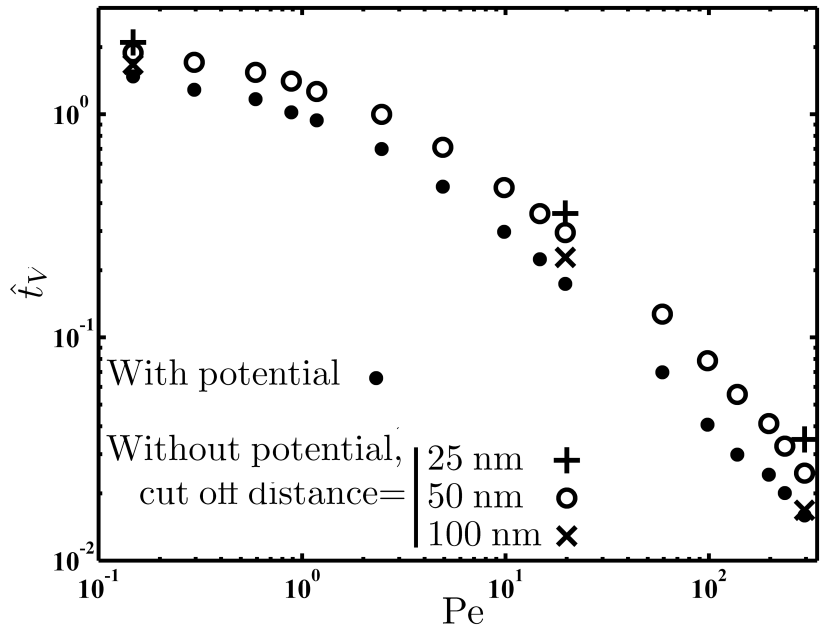

Fig. 2.15. Dependence of normalized collision time on Pe for an explicit potential given in Eqs. (30-32), and in the absence of a potential but with a cut off distance.

Figure 2.15 shows that the binding time obtained using a cut off set to the distance at the minimum of the potential is roughly a factor of two larger than what is obtained with the explicit potential, for this example. It also shows that one can bring the binding time down closer to what is predicted using an explicit potential by increasing the cut off distance by roughly a factor of two. This result hints at the errors incurred in setting an effective cut off distance in the absence of inter-particle forces, and suggests how more accurate results can be obtained. Since every change in parameters governing the potential would require a set of new simulations to give the binding time, the use of an effective cut off distance might be a simpler way of obtaining reasonable estimates, if a way could be found of estimating the best cut off distance.

2.4. Binding kinetics for particles with surface anisotropy

One of the advantages of the presented BD simulation method is its ability to study coagulation of particles with anisotropic interactions, such as Janus spheres having attractive as well as repulsive faces.[4] As a simple illustration of the power of this method, simulations of Janus spheres are carried out in which particles are deemed to have collided when they not only have approached each other close enough but also present their attractive sides to each other; see Fig. 2.16a. Figure 2.16-b depicts the variation of normalized binding times with Pe for both isotropic and Janus particles. When the Janus particles approach each other closely enough to bind, but their attractive sides are not aligned appropriately, it is assumed that due to repulsive forces between the surfaces of particles their gap is no longer allowed to decrease, but is held to the cut off value, and the spheres are allowed to translate and rotate in the shear flow, until the particles either separate from each other or their attractive faces are aligned appropriately for them to bind.

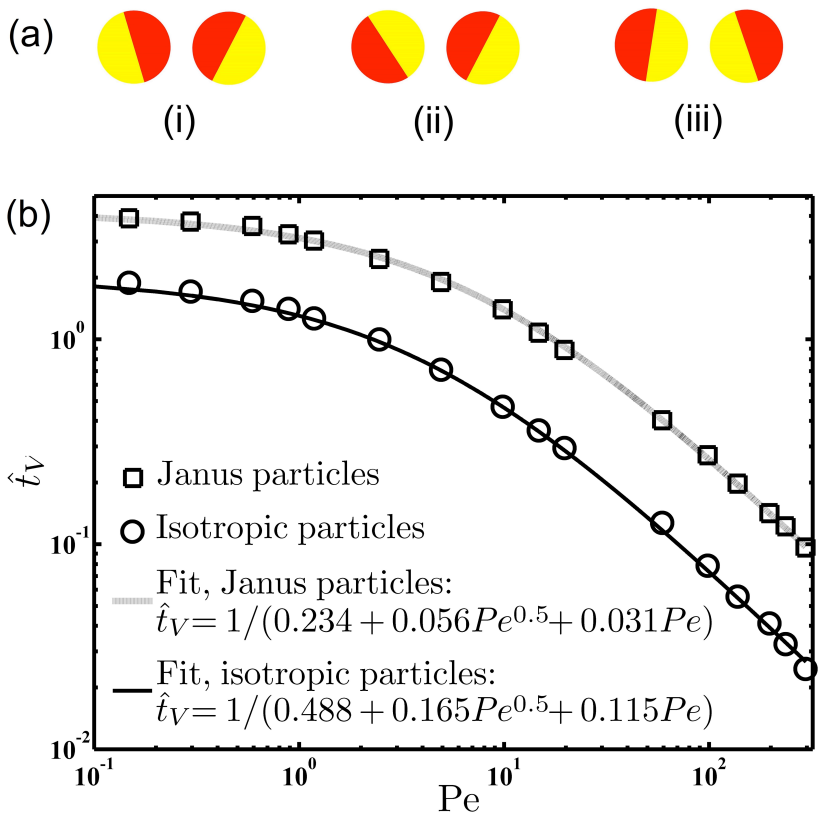

Fig. 2.16. (a) Janus spheres relative orientations. Only state (i) leads to a binding event. (b) Binding time versus Pe for uniform and Janus spheres with 50% of each sphere's surface attractive, and an inner cut off for binding set to 50 nm. Simulation data are fit by the functional forms given in the legend.

Figure 2.16-b illustrates that, as expected, coagulation of Janus particles is roughly four times slower than with isotropic particles. Similar to isotropic particles, an expression of the form $\hat{t}_V = 1/(m_4 + m_5 Pe^{0.5} + m_6 Pe)$ can be used to fit the normalized binding times for Janus particles where m_4, m_5, and m_6 are fitting parameters. The fitting expression is $\hat{t}_V = 1/(0.234 + 0.056Pe^{0.5} + 0.031Pe)$, which captures the data in Fig. 2.16-b with reasonable accuracy. The methods used to predict the results in Fig. 2.16-b could readily be used to consider realistic potentials, more complex particle anisotropic potentials, and unequal size spheres.

2.5. Conclusions

A systematic study using BD method has been carried out to examine the binding kinetics of colloids under shear flow. The following are the main outcomes of this research:

1) For the first time, a method was proposed to predict the coagulation rate of a particle pair with consideration of hydrodynamic interactions for across the entire range of Peclet numbers (Pe) including the perikinetic and orthokinetic limits.
2) Rectangular simulation boxes were introduced to apply the boundary conditions appropriately, and avoid or minimize artificial concentration-depleted "shadow" effects.
3) The effects of different types of inter-particle forces including induced-dipole attraction, a combination of depletion attraction and electrostatic repulsion, and simple abrupt binding at a cut off distance, were studied.
4) The presented simulation results converged to the perturbation solutions of the convection-diffusion equation of Feke and Schowalter[13] at high Pe and determined that their validity is limited to $Pe > 100$.
5) Particles with surface anisotropy were simulated and binding times were determined.

2.6. Acknowledgements

I would like to thank Eric D. Larson and Dr. Jun Liu for theoretical modeling and writing the Brownian Dynamics code used to do simulations presented in this work. I am grateful to Dr. Daniel J. Beltran-Villegas for the fruitful discussions. Also, financial support by the Air Force Office of Scientific Research under MURI project #W911NF-10-1-0518 is greatly appreciated.

2.7. References

1 Lattuada, M. & Morbidelli, M. Effect of repulsive interactions on the rate of doublet formation of colloidal nanoparticles in the presence of convective transport. *Journal of Colloid and Interface Science* **355**, 42-53 (2011).

2 Ahn, H. S. & Kim, M. H. A review on critical heat flux enhancement with nanofluids and surface modification. *Journal of Heat Transfer* **134**, 024001 (2012).

3 Mohammadi, N., Mohammadi, M. & Shafii, M. B. A Review of Nanofluidic Pulsating Heat Pipes: Suitable Choices for Thermal Management of Electronics. *Frontiers in Heat Pipes (FHP)* **3** (2013).

4 Chen, Q., Bae, S. C. & Granick, S. Directed self-assembly of a colloidal kagome lattice. *Nature* **469**, 381-384 (2011).

5 Sacanna, S., Irvine, W. T. M., Chaikin, P. M. & Pine, D. J. Lock and key colloids. *Nature* **464**, 575-578 (2010).

6 Liu, J. & Larson, R. G. Brownian dynamics method for simulation of binding kinetics of patterned colloidal spheres with hydrodynamic interactions. *Journal of Chemical Physics* **138** (2013).

7 Kelkar, A. V., Franses, E. I. & Corti, D. S. Nonideal diffusion effects and short-range ordering lead to higher aggregation rates in concentrated hard-sphere dispersions. *Langmuir* **30**, 3647-3657 (2014).

8 Jahani, K., Mohammadi, M., Shafii, M. B. & Shiee, Z. Promising technology for electronic cooling: Nanofluidic micro pulsating heat pipes. *Journal of Electronic Packaging, Transactions of the ASME* **135** (2013).

9 Mohammadi, M., Mohammadi, M., Ghahremani, A. R., Shafii, M. B. & Mohammadi, N. Experimental Investigation of Thermal Resistance of a Ferrofluidic Closed-Loop Pulsating Heat Pipe. *Heat Transfer Engineering* **35**, 25-33 (2014).

10 Mohammadi, M. *et al.* Ferrofluidic open loop pulsating heat pipes: Efficient candidates for thermal management of electronics. *Experimental Heat Transfer* **27**, 296-312 (2014).

11 Xu, S. H., Sun, Z. W., Li, X. & Wang, J. T. Coupling effect of Brownian motion and laminar shear flow on colloid coagulation: A Brownian dynamics simulation study. *Chinese Physics B* **21** (2012).

12 Smoluchowski, M. v. Versuch einer mathematischen Theorie der Koagulationskinetik kolloider Lösungen. *Z. phys. Chem* **92**, 9 (1917).

13 Feke, D. L. & Schowalter, W. R. The effect of Brownian diffusion on shear-induced coagulation of colloidal dispersions. *Journal of Fluid Mechanics* **133**, 17-35 (1983).

14 Russel, W. B., Saville, D. A. & Schowalter, W. R. *Colloidal dispersions*. (Cambridge university press, 1992).

15 Swift, D. L. & Friedlander, S. K. The coagulation of hydrosols by brownian motion and laminar shear flow. *Journal of Colloid Science* **19**, 621-647 (1964).

16 van de Ven, T. G. M. & Mason, S. G. The microrheology of colloidal dispersions - VIII. Effect of shear on perikinetic doublet formation. *Colloid and Polymer Science Kolloid Zeitschrift & Zeitschrift für Polymere* **255**, 794-804 (1977).

17 Brady, J. F. & Bossis, G. Stokesian dynamics. *Annual review of fluid mechanics* **20**, 111-157 (1988).

18 Jeffrey, D. J. & Onishi, Y. Calculatiuon of the resistance and mobility functions for two unequal rigid spheres in low-Reynolds-number flow. *Journal of Fluid Mechanics* **139**, 261-290 (1984).

19 Jeffrey, D. J. The calculation of the low Reynolds number resistance functions for two unequal spheres. *Physics of Fluids A* **4**, 16-29 (1992).

20 Kim, S. & Karrila, S.J. *Microhydrodynamics: principles and selected applications*. (Butterworth-Heinemann Publications, 1991).

21 Lees, A. & Edwards, S. The computer study of transport processes under extreme conditions. *Journal of Physics C: Solid State Physics* **5**, 1921 (1972).

22 Nyx. *See* https://sites.google.com/a/umich.edu/engin-cac/resources/systems/nyx/highlights-of-nyx *which provides some highlights of the cluster used for computer simulations.*

23 Zhu, G. & Ingber, M. S. Accurate treatment of lubrication forces between rigid spheres in viscous fluids using a traction-corrected boundary element method. *Engineering analysis with boundary elements* **33**, 467-473 (2009).

24 Pozrikidis, C. Interception of two spherical particles with arbitrary radii in simple shear flow. *Acta Mechanica* **194**, 213-231 (2007).

25 Van de Ven, T. *Colloidal Hydrodynamics*. (Academic Press, 1989).

26 Kraynik, A. M. & Reinelt, D. A. Extensional motions of spatially periodic lattices. *International Journal of Multiphase Flow* **18**, 1045-1059 (1992).

27 Shah, A. A., Schultz, B., Kohlstedt, K. L., Glotzer, S. C. & Solomon, M. J. Synthesis, assembly, and image analysis of spheroidal patchy particles. *Langmuir* **29**, 4688-4696 (2013).

Chapter 3

Growth Kinetics in Layer-by-Layer Assemblies of Organic Nanoparticles and Polyelectrolytes

The content of this chapter are published in:

M Mohammadi, A Salehi, RJ Branch, LJ Cygan, C Besirli, RG Larson, Growth Kinetics in Layer-by-Layer Assemblies of Organic Nanoparticles and Polyelectrolytes, 2017, ChemPhysChem 18 (1), 128-141.

3.1. Introduction

Functional thin films have attracted significant attention recently,[1,2] due to their versatility and ease of fabrication. One of the most flexible methods of assembling these films is by layer-by-layer (LbL) deposition, which is the alternating deposition of oppositely charged polyelectrolytes (PEs) or oppositely charged PEs and nanoparticles (NPs). LBL assembled thin films are easy to fabricate, inexpensive, and their properties can be finely tuned.[3,4] Furthermore, the process of making these films does not need to be done under extreme conditions.[5]

Even though the major driving force for the LbL assembly is usually electrostatic interactions, other interactions including hydrogen bonding, hydrophobic interactions, host-guest interactions, covalent bonding, etc., lead to the formation of such assemblies.[4,6] In electrostatically driven PE/PE assembly, LbL growth occurs due to charge overcompensation, i.e. each film ingredient deposited on the surface reverses the surface charge, making it ready to adsorb the next LbL layer.[4] LbL assembly of PEs and organic NPs has considerable applications in drug delivery,

coating, creation of three dimensional scaffolds, and sensors to name but a few.[4,7-16] However, little is known about the mechanism of their growth, and its effective parameters. Thus, it is important to study PE/organic NP LbL films to better understand the effects of different parameters on their assembly and growth.

A major parameter affecting the growth kinetics of LbL films is the molecular weight (MW) of the PE. MW affects the diffusion of the PE chains within the PE matrix and their mobility in the bulk solution. Moreover, MW influences the thermodynamic driving force for the diffusion and the overall integrity of the LbL film. For PE/PE films, several studies have shown the dramatic effect of MW on the thickness and morphology.[17-20] Nestler et al. studied the effect of MW on the growth kinetics of poly(styrenesulfonate) (PSS hereafter)/ poly(diallyldimethylammonium chloride) (PDADMAC hereafter) multilayer films.[17] Below a certain MW, they demonstrated that an increase in the MW of the polyanion (PSS) decreases both the film thickness and the layer number at which the growth rate changes to the linear regime. However, they reported a completely opposite trend in response to a variation of the MW of the polycation (PDADMAC). Shen et al. studied the effect of the polyanion (hyaluronan) MW on the growth kinetics of poly(L-lysine)/hyaluronan LbL films.[18] In contrast to Nestler et al.,[17] they showed that increasing the polyanion MW increases the film thickness. This reveals the complex effect of MW of the PE on LbL growth and suggests that it depends on the specific system being studied.

In contrast to PE/PE films, very few studies have addressed the effect of MW of the PE on the growth kinetics and surface morphology of PE/NP films, and even for these, the MW was not the main focus. Rahman and Taghavinia used poly(ethyleneimine) (PEI) with two different MWs (1.3 and 750 kg/mol) to grow PEI/TiO_2 NP composites.[3] They measured LbL growth with UV-visible spectrophotometry and concluded that film growth is 25 % slower when PEI with the lower MW is employed. In another study by the same group, Rahman et al. showed greater deposition for PEI/TiO_2 NP composites with lower MW PEI.[21] They explained this opposite growth behavior by noting that the substrate and its geometry have important effects on the film

growth. In the later study, they grew composites on cellulose fibers as opposed to the planar quartz sheets that they employed for the earlier work. They claimed that PEI with lower MW could diffuse into the porous structure of cellulose faster. In addition, they showed that films with lower MW of PEI have a less porous structure. In contrast to findings of Rahman et al.[3,21] which showed a large effect of MW of PE on growth and structure of TiO_2 composites, Kniprath et al. illustrated that the surface characteristics of PSS/TiO_2 NP or PDADMAC/TiO_2 NP films are independent of the MW of the PE.[5] They used MWs of 70 kg/mol and 1,000 kg/mol for PSS and < 100 kg/mol and 400 to 500 kg/mol for PDADMAC. In these studies, only a couple of MWs were considered, so it is hard to reach a conclusive picture of the effect of MW. Thus, there is need for further study of MW on the growth kinetics and surface morphology of PE/NP composite films.

In addition to the MW of the PE, the pH and salinity of the deposition solutions are decisive factors affecting the buildup of the LbL films. The pH, for example, affects the charge density of weak PEs.[22] Bieker and Schönhoff investigated the effect of the pH of the depositing solutions on the growth of poly(allyl amine hydrochloride) (PAH)/poly(acrylic acid) (PAA) LbL assemblies.[23] They discovered various growth regimes with different growth behavior (linear and exponential) and film quality (soft and rigid) with simple variation of pH. They rationalized their observations by noting that at different pH values, the degrees of ionization, electrostatic interactions, mobility and inter-diffusion of PE chains vary. Peng et al. studied the effect of pH and salinity of deposition solutions on the growth kinetics of PEI/SiO_2 NP composites, showing that deposition of low pH SiO_2 NPs and high pH PEI result in exponential film growth.[24] They claimed that the pH difference between PEI and SiO_2 solutions during the LbL assembly alters the charge of PEI chains and thereby enhances their diffusion, so that during a single nanoparticle deposition step, more nanoparticles are able to be deposited, leading to deposition of multiple layers of SiO_2 NPs in a single deposition step.

Salt has two competing effects on the growth kinetics of LbL films. First, simple ions screen the electrostatic interactions and reduce the driving force for LbL assembly.[22] Second, salt-induced weakening of electrostatic interactions increases the diffusivity of polymer chains and affects their conformation. Recently, Salehi et al. studied the effect of pH and salinity on the growth of PE/PE LbL films and how the growth rate correlates to the bulk complexation thermodynamics of the two PEs at the same pH and salinity.[22] It was shown that even though there is no one-to-one correlation between different regimes of LbL growth (linear and exponential growth) and bulk complexation (precipitate and coacervate formation), salinity influences the growth kinetics in a more or less universal fashion. It was shown that growth rate increases with salinity at low salt concentration, while it decreases as the salt concentration approaches the critical concentration for dissolution of the bulk polymer-rich phase into a single-phase. It was demonstrated that depending on the PEs employed, variation of pH and salinity could dramatically alter the growth mode of LbL films from linear to exponential and vice versa.

The effects of ionic strength of the deposition media on the growth rate of PE/NP composites have been studied as well.[5,24-28] Ghannoum et al. studying the growth kinetics of LbL assembly of PDADMAC and platinum NPs capped with poly(acrylate), showed that film growth is very sensitive to the ionic strength of the suspension.[25] They identified 50 mM as the optimum salt concentration beyond which film growth degrades. Some of the studies focused on the salinity of PE solutions, as the addition of salt to particulate suspensions could lead to aggregation as electrostatic repulsion is screened. Peng et al. demonstrated that addition of salt to a PEI solution degraded the growth of PEI/SiO_2 NP films.[24] In contrast, Ostendorf et al. reported that increasing the ionic strength of PAH solutions up to 1 M increases the thickness of PAH/gold NP films somewhat, although it did not seem to affect the amount of NPs deposited in the film.[26] Kniprath et al., on the other hand, found that increasing the ionic strength of the PE solution from 0 to 1 M did not affect the surface morphology of the resulting PSS/TiO_2 NP or PDADMAC/TiO_2 NP films.[5] All in all, it seems that the only clear conclusion that can be drawn is that the effect of

salinity on the growth and structure of LbL films strongly depends on the specific chemistry of the ingredients.

Despite the importance of the observations made in previous studies, to the best of our knowledge, there is no systematic study of the effect of the MW of the PE on the growth kinetics of PE/organic NP LbL films. Therefore, the dependence of MW on growth kinetics with different NP size and salinity of the media (both PE and PS solutions) are elucidated. In addition, the surface morphology of the LbL films with different MWs using atomic force microscopy (AFM) and scanning electron microscopy (SEM) is investigated. As a model for organic NPs, polystyrene (PS) beads of different size and surface functionalization are chosen to study the growth kinetics of their LbL assembly with two different PEs, namely, PEI and PAA. Being weakly dissociating PEs, PEI and PAA are selected so that their charge density can be tuned with pH. Prior to studying the effect of MW, the effect of the NP concentration, the pH of the deposition solutions, and the deposition time are examined to find the optimal growth conditions for each parameter. This study is aimed at engineering the structure of LbL films composed of organic NPs and PEs and possibly use such films for drug delivery application.

3.2. Experimental section

3.2.1. Materials

PEI and PAA with different MWs were employed as the polycation and polyanion, respectively. Branched PEI with MWs of 750 (Polydispersity index (PDI): 12.5) and 25 kg/mol (PDI: 2.5) were purchased from Sigma-Aldrich (St. Louis, MO). Branched PEI with a MW of 70 kg/mol (PDI: 13) and PAA with MWs of 2, 5 and 30 kg/mol (PDI for these polymers: 2.4) were purchased from Polysciences (Warrington, PA). PAA with a MW of 240 kg/mol was obtained from Acros Organics (Belgium). The PDIs were obtained from the manufacturers.[29] Negatively charged PS (PS-) NPs bearing sulfate functional groups with particle sizes (diameters) of 26±3,

41±6, 100±8 nm as well as positively charged PS (PS+) NPs with amidine functionalization and particle sizes of 23±5, 44±6, 100±9 nm were purchased from Life Technologies (Eugene, OR). The sulfate-functionalized NPs (PS-) with sizes of 26, 41, and 100 nm had highly varying surface charge densities of 3.4, 0.6, and 0.2 $\mu C/cm^2$, respectively. On the other hand, the NPs bearing amidine functionalization (PS+) with sizes of 23, 44, and 100 nm had nearly the same surface charge densities of 3.0, 3.4, and 3.2 $\mu C/cm^2$, respectively. The surface charge densities and particle sizes were obtained from the manufacturer.[29] KCl was obtained from Sigma Aldrich to study the effect of salinity on the LbL growth. All other materials were purchased from Sigma Aldrich. No additional purifications were performed on the materials.

3.2.2. Quartz crystal microbalance measurements

The growth of PE/NP multilayers deposited on quartz crystals was monitored in the dry condition with a quartz crystal microbalance (QCM-200, Stanford Research Systems Inc., Sunnyvale, CA). Chrome/gold coated quartz crystals were obtained from Stanford Research Systems and had a resonance frequency of around 5 MHz. Initially, crystals were treated using piranha solution (a mixture of sulfuric acid and 30 % hydrogen peroxide at 3 to 1 volumetric ratio) for 2.5 minutes. Note that piranha solution is very reactive and dangerous and considerable care should be taken when handling it. Piranha treatment not only cleans the substrate, but it also makes it negatively charged. Such a negatively charged substrate is needed for the subsequent PE deposition step. Next, the crystals were rinsed thoroughly with DI water and dried with airflow. HPLC water (Fisher Scientific, Waltham, MA) was used for preparing PE or PS solutions. PE solutions employed in this research all have the same monomer concentration of 0.23 M. Also, PS suspensions were used at a concentration of 0.1 wt% unless specified otherwise. PS suspensions were sonicated with a probe sonicator (Ultrasonic Processor, Cole-Parmer Inc., Vernon Hills, IL) for 33 seconds prior to use in order to avoid agglomeration of NPs. To adjust the pH value of the

PE/PS solutions, HCl and KOH were used and pH values were measured with an Orion 3Star Benchtop pH and conductivity meter (Thermo Scientific). In each plot in the results and discussion section, the pH for each solution used during multilayer growth is expressed in parentheses. The pH of deposition solutions was adjusted at the beginning of the LbL growth experiments. It was observed that for rinsing waters and NP suspensions, the pH drifts over time. For the case of rinsing water and NP suspension at a pH value of 7, pH drift was not significant and was typically below 0.5 units. However, for rinsing water with pH = 9.9, the variation in pH could be larger (even more than 1 pH unit). A similar pH variation during LbL growth has been reported by Peng et al.[24] In the Appendix B (Fig. B.1), the effect of pH drift on LbL growth are compared. We believe that such a drift does not have a significant influence on the trend of the results as all of the experiments were performed in relatively similar condition and time duration. For the PE solution, pH drift was not found to be an issue, as the pH was stable over several days. To commence the LbL growth, the PE solution was poured onto the crystal surface and was left there for 15 minutes unless specified otherwise. Subsequently, using DI water with the pH of the deposition solution, the crystal was rinsed to remove excess PE chains that are not attached to the surface electrostatically. Next, the crystal was dried with a mild airflow. Afterwards, the variation in vibration frequency was recorded using the QCM. Subsequently, the above-mentioned procedure was repeated for the PS suspension to deposit a PS layer on top of the deposited PE layer. The deposition of PE/PS layers was continued until 8 bilayers were grown on the quartz substrate.

As mentioned before, the resonance frequency shifts of the chrome/gold crystal oscillator were recorded after each deposition step in each experiment. According to the Sauerbrey equation for rigid films,[24,30,31] the deposited mass per unit area (or thickness) is linearly related to the shift in resonance frequency as shown in Eq. (3.1).

$$\Delta f = -C(\Delta m) \tag{3.1}$$

Where Δf is variation of vibration frequency of the QCM crystal, Δm represents the deposited mass per unit area, and C is crystal's sensitivity factor which is 56.6 Hz.cm^2/μg for the chrome/gold-coated quartz crystals as reported by the manufacturer.[31]

Prior to the growth of a PAA/PS+ composite, a layer of PEI with a MW of 750 kg/mol and pH of 7 was deposited onto the substrate as the precursor, or primer layer. However, PEI/PS- multilayers were directly grown on the crystal without needing a precursor layer. All the experiments were performed at room temperature of 22±3. It should be noted that in all the plots shown in the results and discussion section, odd-numbered and even-numbered steps represent PE and PS depositions, respectively.

3.2.3. Growing thick multilayer films

To grow films of several LBL assembled PE/PS double layers, an LbL robot (StratoSequence, nanoStrata Inc., Tallahassee, Fl) was used. The films were grown by dipping a microscope glass slide (Fisher Scientific, Waltham, MA) into PE/PS solutions for 10 minutes. For QCM experiments, a deposition time of 15 minutes was used. The effect of deposition time on LbL growth was studied using QCM and there was negligible variation in film growth between 10 and 15 minutes deposition times (results shown in the Appendix B, Fig. B.2). Thus, a 10-minute deposition time was chosen for growing very thick films with the robot to reduce LBL buildup time while ensuring maximum film growth. After each deposition step, the glass slides were dipped successively into two beakers containing DI water with the pH set the same as in the preceding deposition solution. Subsequent to the rinsing steps, the film was blown dry with a flow of air for 3 minutes. The film buildup was continued until 59 double layers of PE/PS were deposited onto the surface. The glass slide was treated with piranha solution prior to the film growth. The amount of each dipping solution was constantly monitored to ensure that the solution volume remained at nearly 120 ml throughout the experiments. The PS suspension was sonicated

each time considerable agglomeration of NPs was seen due to dipping of the glass slide and possible complexation formation of free NPs with film ingredients. Fresh particle suspensions used for thick multilayer growth looked clear. When the PS suspension seemed too cloudy and contaminated by multiple dipping steps, the entire suspension was changed to a fresh one. For the PE solution, however, no noticeable change was observable in solution quality after the dipping steps. Nevertheless, as a precaution, the PE solution was changed after every 20-bilayer buildup, or so. Further, the rinsing waters were changed with fresh ones after every 4-double layer growth.

3.2.4. Atomic force microscopy studies

An atomic force microscope (Dimension Icon, Bruker Nano Inc., Santa Barbara, CA) was employed to study the surface morphology of the films during LbL growth. AFM tips (OTESPA, Bruker Nano Inc., Santa Barbara, CA) with a nominal resonant frequency of 300 kHz, spring constant of 26 N/m, and nominal tip radius of 7 nm were used. AFM measurements were carried out with a scan rate of 1 Hz and in tapping mode.

In each LbL experiment, a fresh quartz crystal was employed. It should be noted that the surface of the LbL films was composed of some rough and smooth regions. As more layers were deposited onto the surface, the proportion of rougher areas increased. A sample photo taken by the optical microscope of AFM is shown in the Appendix B (Fig. B.3). The roughness of these areas could reach as high as a couple of microns for films with 8 PE/NP double layers, which was beyond the AFM measurable range. Thus, AFM analysis was done on relatively smooth areas only. For each sample, 8 different smooth areas were randomly selected for doing AFM and roughness values were averaged to increase measurement accuracy. We did not try to measure precisely the fraction of “smooth” surface present, but did notice that it decreased with increasing numbers of layers, from perhaps 60% “smooth” by the end of first double layer growth to around 20% “smooth” after deposition of 8 double layers.

3.2.5. Scanning electron microscopy studies

The surface of LbL films was imaged with a FEI XL30FEG scanning electron microscope, with an accelerating voltage of 10 kV, and magnifications of 400 and 80,000. A magnification of 8,000 was chosen to obtain SEM cross section micrographs. As investigated LbL films were not conductive, prior to doing SEM, their surfaces were coated with a thin layer of gold.

3.2.6. Error analysis

The standard error for each parameter studied is calculated via Eq. (3.2). These parameters include frequency shift of QCM crystal (Δf), thickness (t) (determined using the Sauerbrey equation (Eq. 3.1) and converting the mass per unit area into thickness), and rms roughness values (R) obtained from AFM measurements.

$$e_X = \sqrt{\frac{1}{N(N-1)}\sum_{i=1}^{N}(x-\bar{x})^2} \tag{3.2}$$

Where e is standard error, x is each parameter mentioned above, $\bar{x}$ represents average value of x, and N is the number of replicate experiments done to assess the reproducibility of the results. For determining standard error in frequency shift or thickness, two or three replicate tests were performed for a few of the experiments. Due to time-consuming nature of LbL growth tests, it was practically impossible to repeat all the results reported in this research, and so the error bars given in some of the figures can be taken to be representative. To determine the roughness values, 8 different areas of film were tested to ensure accuracy. The standard errors in LbL growth measurements based on variation of frequency shift were typically below ~15 %, as determined by replicate runs. The errors could be attributed mainly to small variations in properties of initial layers that are propagated and amplified in subsequently deposited layers. When salt was added to the solutions, the standard error could reach as high as 30 %. Increasing ionic strength is

known to reduce the stability of multilayer films[27] and that might have caused the relatively higher error values in these cases.

The standard errors in determining thickness and rms surface roughness of LbL films were generally less than 15 and 10%, respectively. Knowing the errors associated with thickness (t) and rms roughness (R), one can determine the error of the ratio of roughness to thickness using Eq. (3.3), which is a standard formula for propagation of errors. The calculated error was below 18 % for the worst case studied.

$$e(\frac{R}{t}) = \frac{R}{t}\sqrt{(\frac{e(t)}{t})^2 + (\frac{e(R)}{R})^2} \qquad (3.3)$$

A number of LbL deposition experiments were carried out involving no polyelectrolytes, but only PS NPs, with opposite charges in alternating layers, the results of which were entirely irreproducible. Insufficient contact area between rigid spherical PS NPs is presumably to blame for the low inter-particle cohesion that compromises the integrity of the whole film. Whatever NPs managed to be deposited were likely washed off during the rinsing steps. Nonetheless, fairly reproducible growth kinetic data (with errors discussed above) were obtained upon replacing one of the two oppositely charged NP solutions with a like-charged PE solution. PEs seem to act as a glue between the PS NPs, stabilizing the resultant composites.

3.3. Results and discussion

3.3.1. PEI/PS- system

Initially a multilayer system composed of positively charged PEI as the polyelectrolyte and negatively charged PS (PS- hereafter) NPs carrying strongly charged sulfate functional groups were chosen. The effects of deposition time, NP concentration, solution pH, and PEI MW on growth were studied. It will be shown that variation of these parameters enables one to tune the

growth kinetics of PEI/PS- composites. Results for the effect of deposition time on film buildup are shown in the Appendix B (Fig. B.2) for brevity.

3.3.1.1. Effect of nanoparticle concentration

Figure 3.1 indicates the effect of NP concentration on the growth kinetics of a PEI/PS- composite.

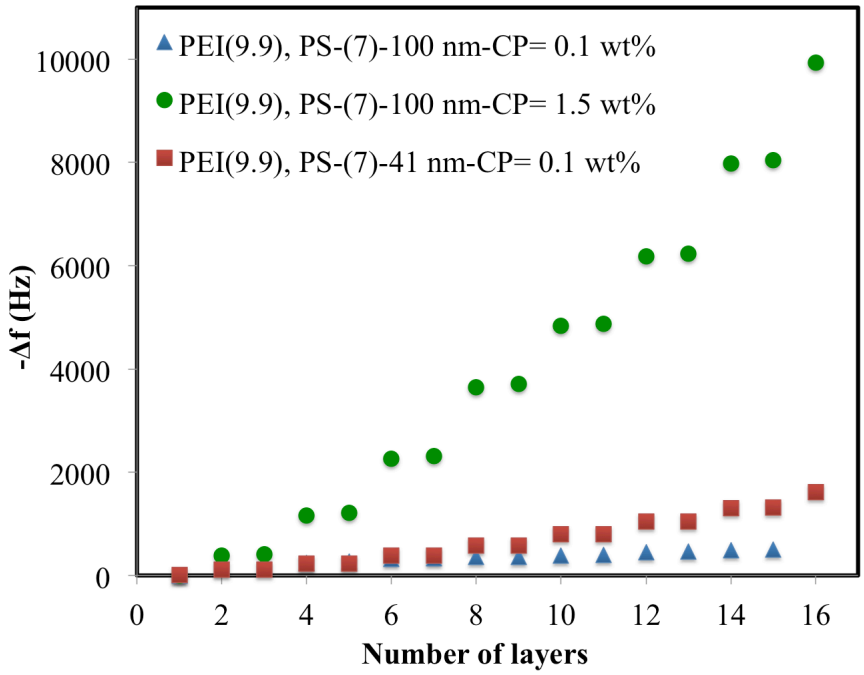

Fig. 3.1. The effect of NP concentration and size on the growth kinetics of a PEI/PS- thin film. PS- NPs are deposited during the even-numbered steps. PEI with a MW of 750 kg/mol is used. In the legend, the numbers in the parentheses indicate the pH value of the solutions. For each case, the diameter of the employed NPs is given in nm in the figure legend. "CP" stands for concentration of particles. In this and all figures, the polymer monomer concentration used in the solutions is 0.23 M.

As shown in Fig. 3.1, for the same mass concentration of 0.1 wt%, smaller NPs (41 nm-sized ones) lead to larger frequency shifts and thus greater mass depositions in the PEI/PS- film, which may seem counter-intuitive. However, for the same mass concentration, larger NPs have a lower number density in the solution than do smaller ones. Due to their much slower diffusion, it is therefore less likely for the larger NPs to get adsorbed into the PEI/PS- composite.

To find the proper basis for assessing particle concentration, the growth of films with 100 nm-sized particles was studied at the same particle number density as that for 41 nm-sized ones. A dense suspension of 100 nm-sized particles with a concentration of 1.5 wt% (which has the same number density as a 0.1 wt% suspension of 41-nm particles) was therefore used in combination with a PEI solution of the same concentration as before to grow PEI/PS- multilayers. For this case, the deposition rate of PS- NPs was so fast that the entire chrome/gold crystal was instantly coated by a visibly thick layer of NPs. At the same number density, the larger 100 nm particle suspension produces an LbL film with a frequency shift that is at least five times greater than that of the smaller 41 nm-sized particles. Thus, there does not seem to be an obvious choice for a concentration basis at which composite films of different NP sizes yield the same growth rate. Consequently, for simplicity, the rest of the experiments are carried out with PS NPs of 0.1 wt% concentration. It is also evident from Fig. 3.1 that for the same NP size of 100 nm, increasing the suspension concentration boosts the growth kinetics of PEI/PS- thin films.

Finally, the data of Fig. 3.1 indicates that PEI/PS- thin films grow through a cooperation between PEI and PS- deposition steps. The more PEI that is deposited in an LbL step, the more PS- NPs are deposited in the subsequent step. Also, the "stepped" appearance of the growth or "odd-even" effect in this figure, with a relatively small mass added in the odd steps, shows that contribution of the PEs to the frequency shift was much less than that of the NPs. This trend was observable for all growth study experiments. This phenomenon has already been reported in the literature.[28]

3.3.1.2. Effect of solution pH

Figure 3.2 depicts the influence of pH on the buildup of PEI/PS- multilayers. PS- NPs are functionalized with sulfate groups, so their surface charge is independent of pH and they are stable over a wide range of pH. On the other hand, PEI is a weak PE ($pK_b \sim 10^{24}$) whose charge density is dependent on pH. At pH = 9.9, PEI should be nearly 50 % charged, while decreasing

the pH to 7 renders PEI chains nearly fully charged. PS- NPs with a diameter of 41 nm were chosen, as their diameter was an intermediate value among the group of PS- NPs studied.

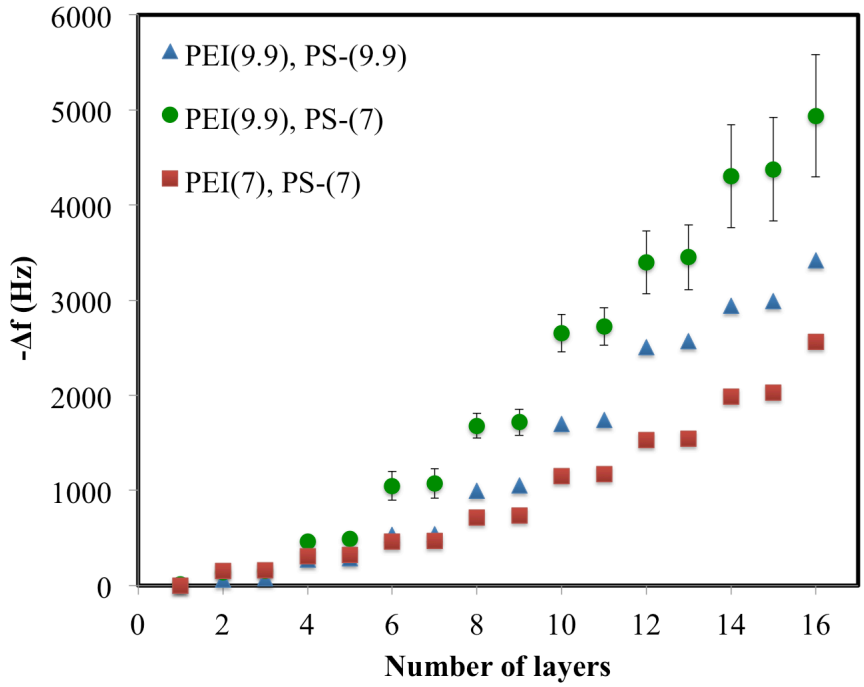

Fig. 3.2. The effect of pH on LbL growth of a PEI/PS- composite. PEI with a MW of 70 kg/mol and 41 nm-sized PS- particles are employed. The concentration of PS- NPs is 0.1 wt%.

As shown in Fig. 3.2, the pH values of both the PEI solution and of the PS- suspension have considerable influence on the growth kinetics of the PEI/PS- composite. Furthermore, the growth rate of the PEI/PS- film is fastest when PEI and PS- solutions have pH values of 9.9 and 7, respectively.

The degree of ionization has a dramatic influence on the growth rate of a PEI/PS- composite. When PEI and negatively charged PS solutions are deposited at the same pH (= 7.0), PEI chains are expected to be fully charged. When PEI chains are deposited at pH = 9.9, however, their charge is less than it is at pH = 7.0, and more chains need to deposit atop the underlying NPs to compensate the opposite charge on the film. Based on the pK_b of PEI in the bulk, the charge density of PEI at pH 7 should be roughly twice as high as it is at pH 9.9. It should be noted, however, that weakly dissociating PEs of oppositely charged functional groups inside PE/PE

multilayer films have long been shown to be more highly charged than in solution via the charge regulation effect.[32,33] The surface functional groups on PS- NPs can thus induce further charging in PEI chains at pH 9.9 once they are fully embedded in the film. However, since the growth is markedly faster for PEI chains depositing at pH 9.9 with PS- NPs at pH 7, as compared to the other two conditions studied in Fig. 3.2, the PEI chains depositing at pH 9.9 are likely far from being fully charged. Therefore, the PS- NPs need to absorb more PEI chains at pH 9.9 than they do at pH 7 to achieve charge compensation, leading to faster growth.

The degrees of charge compensation for three different LbL growth experiments studied in this section are presented in the Appendix B (Fig. B.4). From the QCM data shown in Fig. 3.2, it is clear that the frequency shift ratio (or equivalently the mass per unit area ratio) of deposited NPs to that of PEs in each double layer is on the order of 10, while the charge compensation factor (defined as the ratio of charges associated with NPs to those of PEs) for each double layer for these experiments is on the order of only 0.01 (see Fig. B.4 in the Appendix B), indicating that the charges on the NP's deposited in a layer fall far below that needed to compensate the charge on the PE layer deposited in the layer just beneath it. (The important caveat that the difference in total film mass between deposition of each layer is taken as a measure of the mass actually deposited from the solution should be noted. It is possible that mass of NP's deposited is much greater than this, if an equivalent mass of PE is washed off the film as the NP's are deposited.) The lack of strong charge regulation can thus be rationalized by fewer encounters between neutral PEI repeat units with particle surface functional groups in PE/NP films than would be expected in PE/PE films assembled under similar conditions. The NPs evidently serve as a sufficiently thick spacer between two alternating PEI layers that render a continuous film build-up feasible despite the very low charge compensation ratios observed. Such excess of charge on PE chains in conventional PE/PE LbL assembly is unsustainable owing to a huge electrostatic repulsion that would be created between narrowly spaced layers of PE present in excess. Evidently, in PE/NP

deposition, accumulation of PE charge from one bilayer to the next is possible. This is an unusual feature that to our knowledge is unique to PE/NP assemblies.

Upon deposition of NPs at pH = 7 following PEI deposition at pH = 9.9, the neutral primary amine groups absorb a proton from the solution as a result of the sudden pH drop, thus creating a sudden jump in areal charge density of the chains decorating the surface. The higher charge density of the PEI-covered surface requires more sulfate-functionalized PS NPs to compensate, as compared to the cases without the abrupt pH change. Consistently, PEI and PS- NPs deposited at the same pH, either both at 7 or both at 9.9, yield thinner films than when the solutions are deposited at the two different pH values considered (Fig. 3.2). Such a sudden charging of PEI chains is lacking when the solutions are deposited at the same pH.

Moreover, the film growth benefits from the high diffusivity of PEI chains into the film during the PEI deposition at pH = 9.9 due to lower charge density of PEI chains, which should lead to weaker binding to PS- particles, and hence faster diffusion.[22] The higher diffusivity of PEI chains at pH = 9.9 is probably another reason for the faster growth kinetics of PEI/PS- composite at this pH compared to the case where both solutions are deposited at a pH of 7, despite the stronger electrostatic interactions in the latter case.

As discussed in the experimental section, the pH of the rinsing water and of the PS NP suspension drift during the deposition. The result is that when the PS particles and PE polymer are deposited at different pH values, nominally pH = 7 for PS- and nominally pH = 9.9 for PEI, the actual pH values differ less from each other as more layers are deposited. As shown in the Appendix B (Fig. B.1), when the pH values of the rinsing water and of the PS- suspension were constantly monitored and maintained at their initial values, the film growth was improved. This observation further bolsters the argument that larger difference between pH values of deposition solutions and rinsing waters leads to faster LbL film buildup.

The effect of pH on the growth kinetics of PEI/PS- composites observed here is similar to that observed by Peng et al. for the multilayer buildup of SiO_2 inorganic NPs and PEI.[24] Here, it is shown that even though the interactions are not exactly the same, a similar trend holds.

3.3.1.3. Effect of molecular weight

Figures 3.3-3.5 indicate the role of PEI MW on the growth kinetics of PEI/PS- composites for different NP sizes. The NP concentration is set to 0.1 wt%.

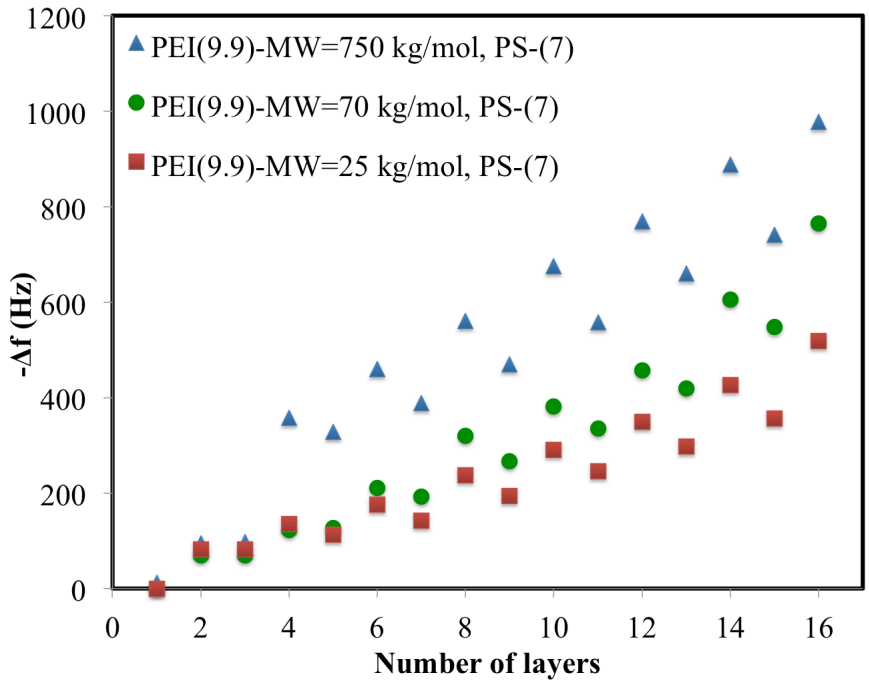

Fig. 3.3. The role of MW of PEI on growth of PEI/PS- LbL film, for PS- NP size of 26 nm.

Conspicuous in Fig. 3.3 is the saw-tooth growth behavior of the films involving the 26 nm PS- particles. It seems that some of the deposited PS- NPs are washed off of the film during the deposition of the PEI (odd numbered steps). Some PEI must have been deposited during these steps to explain the continued growth of the film in the subsequent steps. Moreover, Fig. 3.3 indicates that for 26-nm PS- particles, a higher MW of 750 kg/mol leads to a thicker PEI/PS- composite.

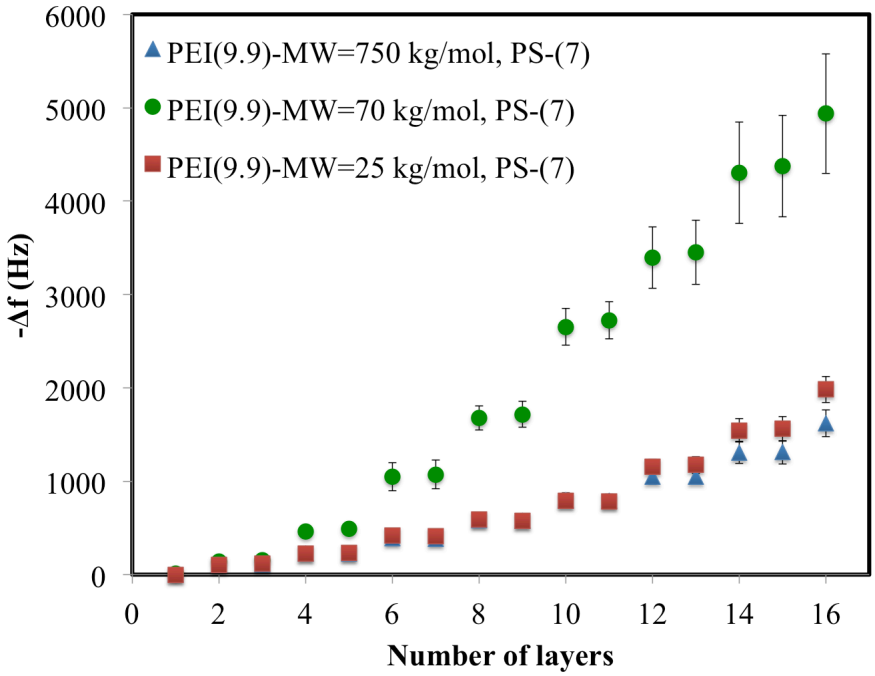

Fig. 3.4. The same as Fig. 3.3, except for a particle size of 41 nm.

Figure 3.4 shows that for the 41 nm PS- particles, the PEI/PS- LbL buildup is maximum at an intermediate PEI MW of 70 kg/mol. Also, unlike the growth kinetics of the 26 nm-sized PS- particles, for 41 nm-sized PS- particles, out-diffusion of ingredients from the film is not observed. Moreover, all three data sets depicted in Fig. 3.4 show accelerating, or "exponential" growth for the particle deposition steps, with increasing numbers of layers. This is especially noticeable for the PEI with a MW of 70 kg/mol.

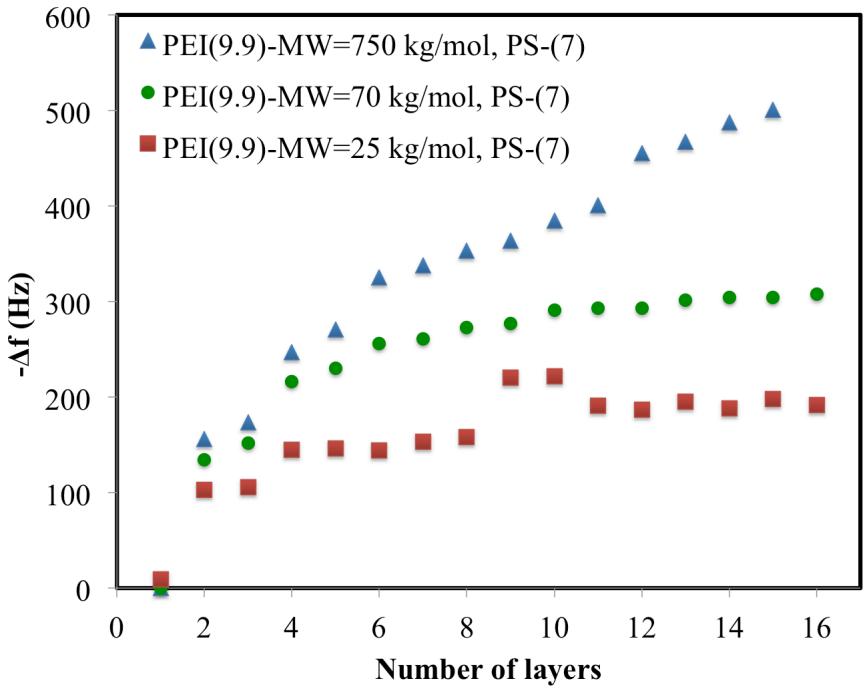

Fig. 3.5. The same as Fig. 3.3, for particle size of 100 nm.

According to Fig. 3.5, for 100 nm-sized PS- particles, the PEI with the highest MW leads to the thickest film.

3.3.2. PAA/PS+ system

In the next set of experiments, another composite system composed of negatively charged PAA as the PE and positively charged PS (PS+ hereafter) NPs carrying amidine functional groups was selected. PAA is a weak PE (pK_a of around 5-5.5[22]). It is approximately 50 % charged at pH = 5, and therefore almost completely charged at a pH of 7.

If the PE/NP LbL growth were entirely driven by electrostatic interactions, it would be plausible to expect that switching the sign of charges on both components should not alter the trends. The LbL experiments with PAA/PS+(amidine) system will thus establish whether the trends observed for the effect of MW on the growth of PEI/PS-(sulfate) multilayers discussed in the previous section are general, i.e. chemistry-independent. Similar to the PEI/PS- system, for the PAA/PS+

composite, increasing the PS+ concentration boosts the growth rate, as shown in the Appendix B (Fig. B.5).

3.3.2.1. Effect of molecular weight

Figures 3.6-3.8 show the growth kinetics of PAA/PS+ LbL assemblies for different MWs of PAA and various NP sizes. Throughout this section, concentration of PS+ NPs was set to 0.1 wt%.

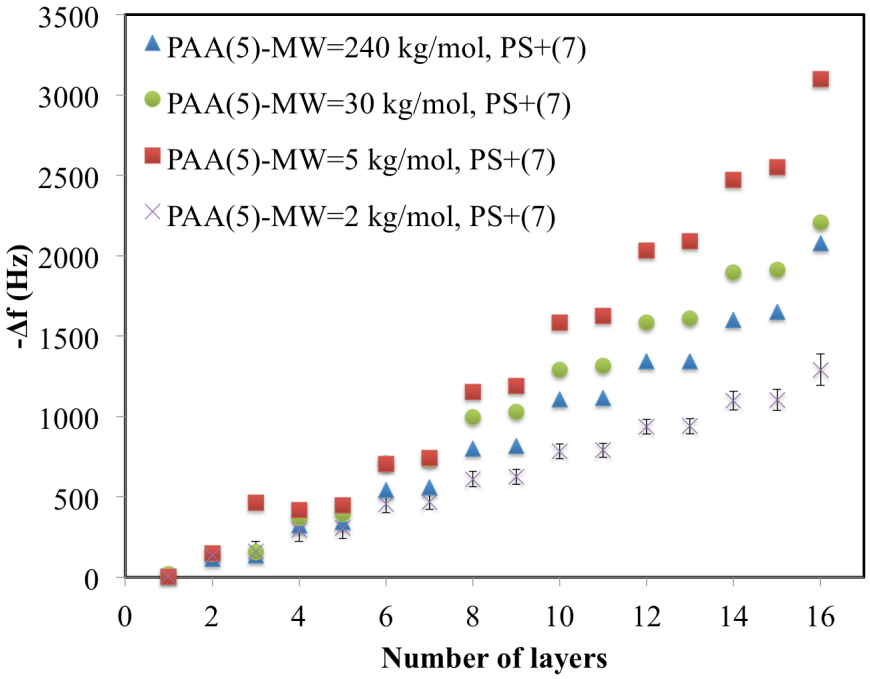

Fig. 3.6. Effect of MW of PAA on PAA/PS+ LbL buildup with 23 nm-sized PS+ particles. For this and subsequent figures, the pH values for each deposition solution (PAA or PS+) is indicated in parenthesis in the figure legend. Note the small value of error bars for PAA with MW of 2 kg/mol.

Unlike the PEI/PS- system with 26 nm-sized particles (Fig. 3.3), out-diffusion of the PS+ NPs of similar size, 23 nm, is not observed for the PAA/PS+ counterpart shown in Fig. 3.6.

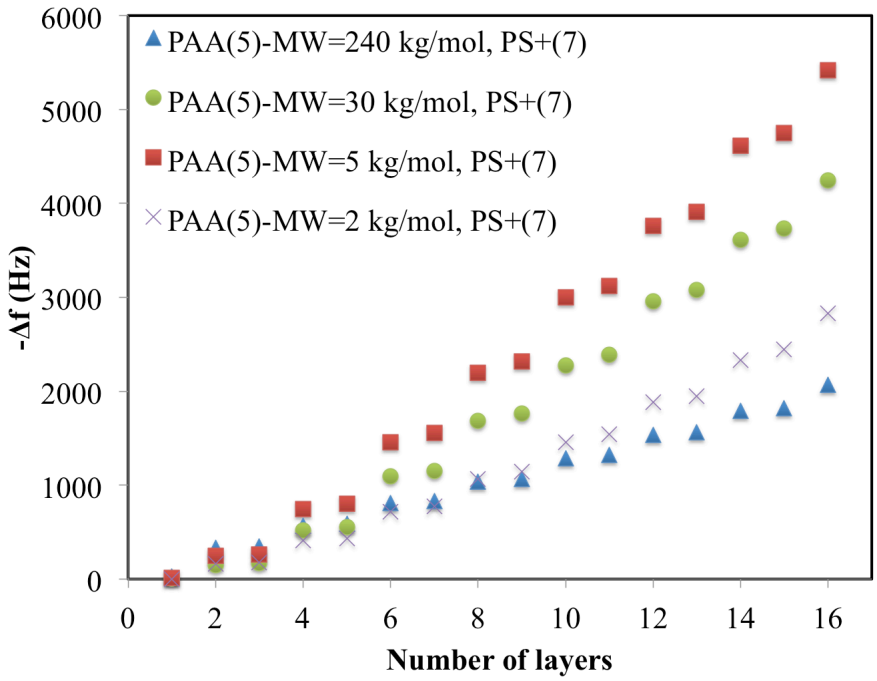

Fig. 3.7. The same as Fig. 3.6, for 44 nm-sized PS+ particles. Data for PAA with a MW of 30 kg/mol have error bars, but these are too small to be visible.

According to Figs. 3.6 and 3.7, the MW has a non-monotonic effect on the LbL buildup of PS+ particle of sizes 23 and 44 nm. Decreasing the MW from 240 to 5 kg/mol boosts the LbL growth rate, but a further decrease in MW leads to a slower growth rate. Evidently a further decrease in the MW to 2 kg/mol lowers the capability of chains to immobilize the PS+ NPs in the composite film. Therefore, there is an optimum MW for the growth of PAA/PS+ multilayers, which is 5 kg/mol for both 23 and 44 nm-sized PS+ particles.

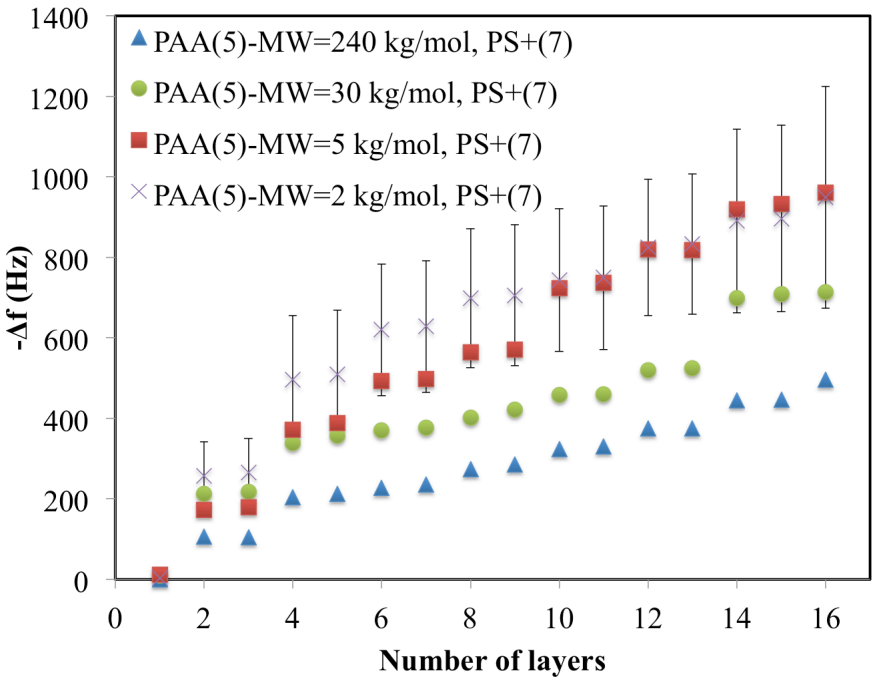

Fig. 3.8. The same as Fig. 3.6, for 100 nm-sized PS+ particles.

Given the margin of error in Fig. 3.8, however, the growth of PAA and 100 nm-sized NP film is virtually insensitive to a further decrease of MW from 5 to 2 kg/mol. We speculate that, similar to behavior of the PS+ NPs of sizes 23 and 44 nm, for 100-nm particles there should be an intermediate MW that leads to the fastest growth of PAA/PS+ films, even though the optimal MW in the case of 100 nm-sized NPs is less than or equal to 2 kg/mol. Given that it is impossible to use AA acid monomers as building blocks in LbL assembly, one would intuitively expect there to be an optimum MW equal or less than 2 kg/mol for 100 nm-sized PS+ NPs.

Table 3.1 summarizes the optimum growth behavior for the different NP sizes and PE MWs studied. For both PAA/PS+ composites with either 23 or 44 nm-sized particles (Figs. 3.6 and 3.7) and for PEI/PS- thin films with 41 nm-sized particles (Fig. 3.4), there is an intermediate MW that leads to the fastest LbL growth. However, the growth rate of PEI/PS- multilayers with 26-nm and 100-nm sized particles does not show an optimal MW over the range of MWs considered (Figs. 3.3 and 3.5). Consequently, one can conclude that the effect of MW on growth kinetics of PE/NP

thin films strongly depends on the specific chemistry of the ingredients as well as on the size of NPs employed. It should be noted that the surface charge density of the sulfate-functionalized particles (PS-) used in growth of PEI films varies greatly with particle size while the amidine-charged particles (PS+) have nearly the same charge density for all three particle-sizes, and this may also play a role in the different behavior observed for the two systems. Further, as mentioned in the experimental section, PEIs had greater polydispersity indices compared to the PAAs. This could also contribute to the different growth kinetics seen for the two systems studied. Even though it is beyond the scope of the current study, the polydispersity of the polymer solutions employed could have a considerable effect on the growth behavior and is worth future investigation.

Table 3.1. Optimum LbL buildup for different PE/NP composites studied as a function of NP size and MW of PE.

PEI/PS- NPs multilayers		PAA/PS+ NPs multilayers	
NP size	Optimum MW	NP size	Optimum MW
26	Large (750 kg/mol)	23	Intermediate (5 kg/mol)
41	Intermediate (70 kg/mol)	44	Intermediate (5 kg/mol)
100	Large (750 kg/mol)	100	Intermediate (2 and 5 kg/mol)

Chain diffusion, particle and chain redissolution, specific chemistry involved in the complexation of opposite charges, surface overcompensation and interparticle bridging are some of the major factors whose relative influence controls the overall LbL growth rate. MW, in particular, affects each of the latter factors in different and even opposite ways. For instance, chain diffusion is enhanced while interparticle bridging is adversely impacted as MW decreases. The obtained

results demonstrate that flipping the sign of the charges borne by PEs and NPs leads to two distinct trends in dependence of LbL growth on MW.

For neutral polymers, the self-diffusivity decreases as the MW increases.[34] Decreasing the MW of the PE at otherwise identical conditions therefore increases the effective chain diffusivity, which tends to increase chain deposition into the film. On the other hand, we speculate that each deposited PE layer bridges the former and subsequent NP deposits. Longer chains can bridge the NPs more easily and the chain entanglement would strengthen such interparticle bridges, boosting the film mechanical integrity. A trade-off between the chain diffusivity and bridging could explain the intermediate optimum MW found for PEI/PS- composites with 41 nm-sized PS- particles, as well as PAA/PS+ LbL films. However, the reverse trend is observed for two of the particle sizes employed in PEI/PS- system (Table 3.1), where for 26 nm-sized particles, appreciable redissolution appears to control the deposition rate (Fig. 3.3). During chain deposition, the film surface charges arising from sulfate groups are compensated by the amine groups along PEI chains. The incoming chains generally overcompensate the surface charges, reversing the sign of the surface charge. Longer chains have been shown to lead to greater charge overcompensation.[35] Even though a better charge overcompensation for the PEI with the highest MW can explain the deviation from the observed trend for PAA/PS+ NP system, further detailed experimental techniques are needed to definitively elucidate this observation and better understand the underlying physics. It might be possible, for example, to use confocal laser scanning microscopy or neutron reflectometry to track the diffusion of polymer in the LbL film which could shed light on the reason for different growth behaviors.[36] Also, single-molecule force spectroscopy experiments could be done wherein a polymer chain is detached from the film and the detachment force profile is measured. This has been proven to be a useful method to determine polymer chain adhesion forces in films.[37]

For larger PS NPs, it is more difficult for PEs to create interparticle bridges and LbL films become unstable in this case. Interparticle bridging becomes even more difficult for shorter PE chains. This might be the reason for larger error bars seen in Fig. 3.8.

3.3.2.2. Effect of salinity

Salt screens the electrostatic interactions between charged functional groups and also impacts the PE diffusivity in the multilayer film. The effect of the salinity of the deposition solutions for PAA/PS+ films composed of 44 nm-sized PS+ particles and PAA with MWs of 5 and 240 kg/mol are shown in Figs. 3.9 and 3.10, respectively. PS+ NPs with diameter of 44 nm were chosen, as this size was an intermediate nanoparticle size among different PS+ nanoparticle sizes studied. According to Fig. 3.7, for this nanoparticle size, PAA with MWs of 5 and 240 kg/mol showed the fastest and slowest growth rates, respectively. Therefore these MWs were chosen to study the effect of salinity for both fast and slow growing films. For the PS+ suspension, even 100 mM salt content did not compromise the suspension stability as verified by dynamic light scattering.

It should be noted that pH of PE and PS solutions were adjusted by the addition of KOH and HCl for different cases studied. This introduced additional K^+ and Cl^- ions to the solutions on top of those introduced by adding KCl. In this section, the term "salinity" refers to the K^+ and/or Cl^- added to the solutions via KCl salt, not including any ions contained in the pH buffer, KOH or HCl. To enhance clarity, the values of ionic strength of the deposition solutions (considering both ions introduced by addition of salt as well as pH buffers) are reported in figure captions. For the case of PS+ NPs, the concentration of ions added to the system for the pH adjustment was far lower than the amount of K^+ and Cl^- ions added to the system to study salinity, so their effect on ionic strength was negligible. For PAAs, however, that was not the case and the higher the salt concentration (KCl), the greater was the concentration of K^- ions needed for pH adjustment. All in all, PAA solutions with higher salt contents needed more ions for pH adjustment too.

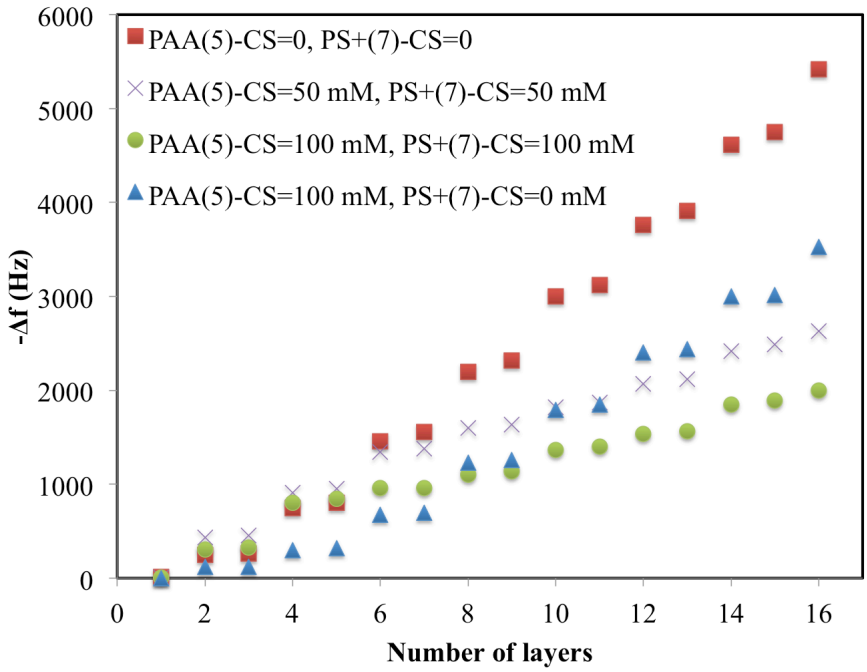

Fig. 3.9. The effect of KCl concentration on growth kinetics of PAA/PS+ multilayers, for PAA with a MW of 5 kg/mol, and 44 nm-sized PS+ particles. Concentration of NPs was 0.1 wt%. The concentrations of salt (CS) in the PAA and PS+ solutions are shown in the legend. The ionic strength was 37, 93, and 147 mM for PAA solutions with salt concentrations of 0, 50, and 100 mM, respectively. For PS+ suspensions however, pH adjustment did not change the ionic strength of the suspensions. Thus, the ionic strength values were the same as salt concentration reported.

As shown in Fig. 3.9, the addition of KCl to solution of PAA with a MW of 5 kg/mol has a detrimental effect on the buildup of the PAA/PS+ composite film, with the growth rate decreasing when 50 mM salt is added to both PAA and PS+ solutions, and a further decrease when the salt concentration is increased to 100 mM. Also, introducing KCl to the PAA solution only leads to a weaker degradation than when it is added to both solutions. Finally, Fig. 3.9 also demonstrates that with the addition of KCl, composite films still grow linearly.

The effect of salinity on the growth rate of multilayer films composed of PAA (M_W= 240 kg/mol) and PS+ NPs (44 nm in size) is indicated in Fig. 3.10.

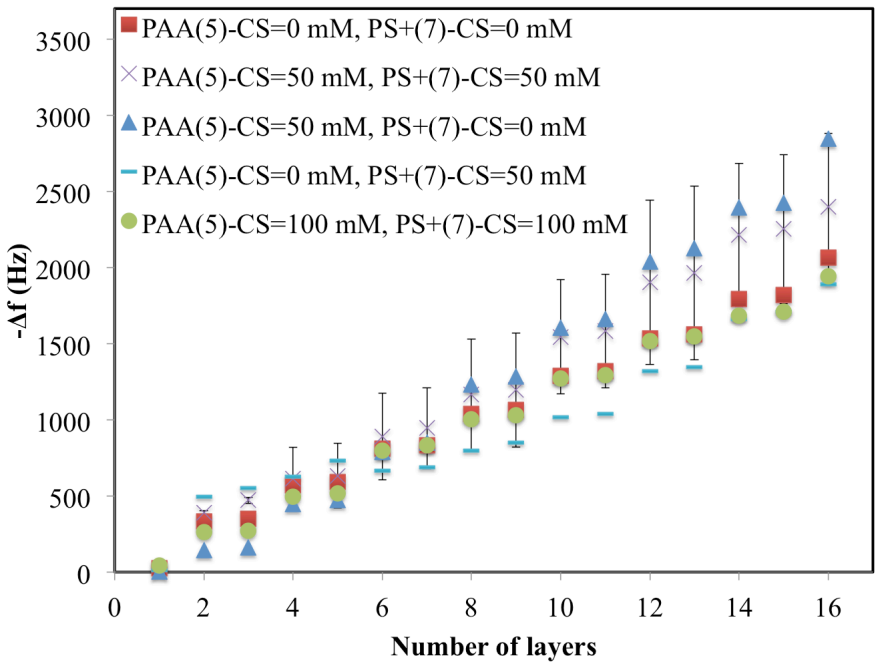

Fig. 3.10. The same as Fig. 3.9 except for PAA with a MW of 240 kg/mol. The concentration of PS+ NPs was set to 0.1 wt%. The ionic strength for PS+ suspensions with salt content of 0, 50, and 100 mM was 0, 50, and 100 mM, respectively. Also, the ionic strength for PE solutions with salt concentrations of 0, 50, and 100 mM was 34, 92, 149 mM, respectively.

Based on Fig. 3.10, for PAA with a MW of 240 kg/mol, the addition of KCl to both PAA and PS+ solutions or to PAA solution alone boosts the LbL growth kinetics. However, the LbL growth is slightly degraded when KCl is only introduced into the PS+ suspension.

Figure 3.10 also illustrates that increasing the salt concentration from 50 mM to 100 mM decreases the growth rate of the PAA/PS+ composite film, for PAA with a MW of 240 kg/mol. Comparing Figs. 3.9 and 3.10, one can clearly observe that salinity of the medium has a stronger effect on frequency shifts of PAA/PS+ films for the smaller MW of 5 kg/mol than for MW of 240 kg/mol. 240 kg/mol was the largest MW of PAA investigated in this study because for much higher MW values, the higher viscosity made it practically impossible to study their film growth kinetics.

Although in the work presented here the PEs interact with surface functionalized NPs rather than with other polymers, as is the case for ordinary PE/PE deposition, the key interactions in both

cases are electrostatic, and can be screened by mobile salt ions. In both cases, increasing the ionic strength decreases the thermodynamic driving force for complexation of PE and NP functional groups, and enhances the diffusivity of PE chains inside the films, a competition that has been shown to affect PE/PE multilayer formation profoundly.[22] Which of these two factors is dominant thus determines whether the film growth is enhanced or degraded by the addition of salt. The relative importance of these two factors in the present study is affected by the MW of the PE. The diffusivity of the PE with low MW is already so high that salt should have only a marginal effect on chain diffusivity. Consequently, for low MW PEs, the reduction of the driving force is the dominant factor, which progressively slows down the growth kinetics of low MW PAA/PS+ NP composites as the salt concentration increases (Fig. 3.9). Interestingly, adding salt only during PAA deposition (while using a salt free NP suspension) leads to an intermediate growth rate.

For the PE with a higher MW, the boost in diffusivity due to the addition of salt apparently outweighs the reduced electrostatic attraction between the oppositely charged components, for salt concentrations up to 50 mM KCl, leading to a boost to LbL growth rate visible in Fig. 3.10. However, a further increase of salt concentration from 50 to 100 mM and the consequent reduction in the electrostatic driving force degrade the growth kinetics of PAA/PS+ composite. Unlike PEs, the deposition of NPs in Fig. 3.10 is weakly affected by KCl whereas changing the salt concentration in the PAA solution while holding that of the NP dispersion fixed appreciably alters the growth kinetics. In contrast with spherical NPs, PE chain conformation, thermodynamics and diffusivity are all drastically altered by the ionic strength of the media and LbL growth rate is thus more sensitive to salinity of the PAA solution than to that of the NP dispersion.

3.3.3. Film characterization

3.3.3.1. Atomic force microscopy study

To study the surface morphology, the PEI/PS- composites with 41 nm-sized PS- particles were selected. These composites are similar to most of the cases studied in that the intermediate value of MW led to the fastest growth rate (Fig. 3.4). Other than ions added to the solutions for pH adjustment, no extra salt ions were added to the either of the ingredients for the LbL buildup. Further, PEI and PS- solutions were deposited at pH values of 9.9 and 7, respectively. Figure 3.11 depicts surface characteristics of composites with different PEI MWs. Instead of performing localized AFM on a very small area, which is a common practice in the literature, a larger area (30 μm×30 μm) was studied to obtain a more representative assessment of the surface morphology. As mentioned previously, 8 different areas of each sample were imaged, but a single image most typical in the range of roughness for each sample is shown in Fig. 3.11. The inset for each AFM image in Fig. 3.11 is in fact the same image as in the corresponding main figure, except with the color scale bar fixed to a range of 700 nm, while in the main figures the scale bars are adjusted to keep the contrast fixed. Thus, the insets allow one to compare the uniformity of roughness from sample to sample, with a uniform color and darkness indicating a film with relatively uniform roughness. The thin films, comprising a few layers, are uniformly dark in the insets because there can be little height variation on a scale of 700 nm when the films are much thinner than 700 nm. The main figures, with variable scale bars and fixed contrast, allow one to observe the surface topology, and the variation in height can be assessed for each figure from the corresponding color scale bar.

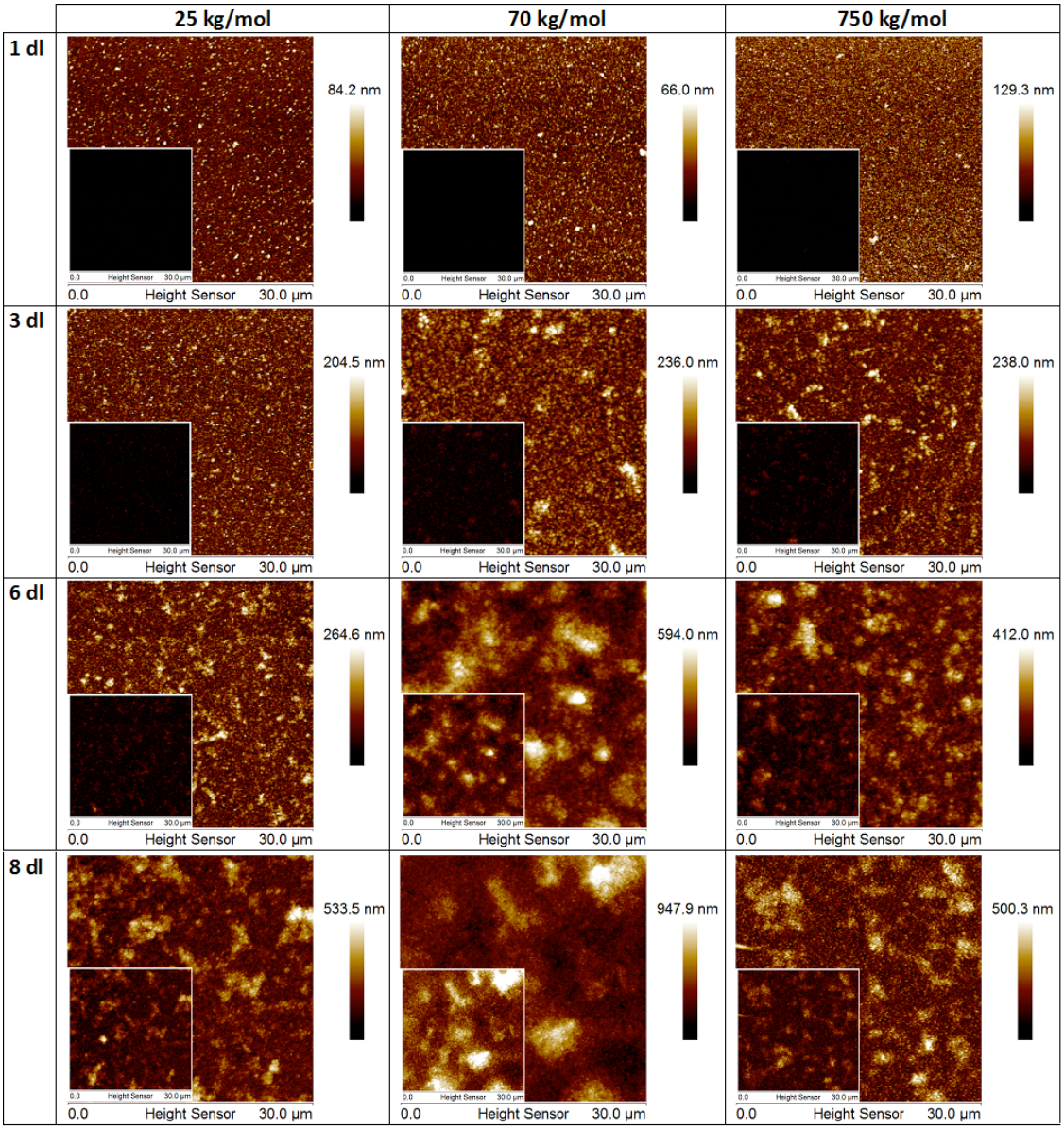

Fig. 3.11. AFM images of PEI/PS- composites with 41 nm-sized PS- particles and different MWs of PEI for different numbers of layers. All the images were obtained once PS- NPs are deposited for 1st, 3rd, 6th, and 8th bilayers. The pH values for the NP and PEI deposition steps were 7, and 9.9, respectively. No salt ions were added for the growth of these films except for the ions introduced to the system to adjust the pH. The scale bars for the main images are also shown. The insets show the corresponding images rendered using a fixed 700 nm scale bar to allow comparison of film height uniformity on an absolute scale.

As can be seen in Fig. 3.11, surface roughness during the growth of LbL films increases dramatically. This trend is seen for all PEIs with different MWs. Some studies have mentioned that LbL growth under pH-amplified condition, i.e. deposition of film ingredients at different pH

values, could lead to rougher surfaces.[18] The effect of pH-amplified deposition on the surface morphology of LbL films was studied by first depositing 8 bilayers of PEI and PS- at pH values of 9.9 and 7, respectively, and contrasting these results with those obtained by depositing the same number of layers of PEI and PS- solutions both at a pH of 7. Root-mean-squared (RMS) roughness values of film surface were determined by examining the results with Nanoscope Analysis software (Bruker Nano Inc.). AFM micrographs, in the Appendix B (Fig. B.6), show that in the latter case (equal pH), the rms surface roughness is around 32 % smaller than in the former (unequal pH). However, since the two cases produced differing total film thickness, and roughness generally increases with thickness (Fig. 3.11), rather than comparing the surface roughness for a fixed number of layers, the roughness-to-thickness ratio is a better basis for comparison, since normally one wants to achieve a layer of a given thickness. Due to much slower growth of PEI/PS- composite when both PEI and PS- solutions are deposited at a pH value of 7, in this case the ratio of roughness to thickness is around 30 % higher than in the pH amplified deposition condition. So, it seems that the amplification of LbL growth by using different pH values for different layers does not increase roughness, at least when roughness is normalized by film thickness. Another possible reason for the high surface roughness could be an uneven distribution of surface charge on the crystal surface, despite the fact that we were careful to be consistent when treating the substrates with piranha solution.

Figure 3.12 depicts the variation of both absolute roughness (shown in the inset) and roughness normalized by the film thickness for PEI/PS- thin films with different PEI MWs. Average film thicknesses of PEI/PS- films composed of PEI with MWs of 25, 70, and 750 kg/mol were estimated to be 330, 825, and 270 nm, respectively. These estimations were obtained by converting the frequency shift (data in Fig. 3.4) of the QCM measurements to mass per unit area using the Sauerbrey equation (Eq. (1) shown in the experimental section). Knowing the mass per unit area and the density of film ingredients, one can estimate average film thickness. Because of the much greater mass deposition of NPs than of PE's, the density of the PS (1.05 gm/cm^3) is

used to convert the mass of film into thickness. This way, the effect of the small density difference between the PS and the PE's is neglected. This makes calculations much easier, and generates minimal error (~0.3% in the worst case) in the final results.

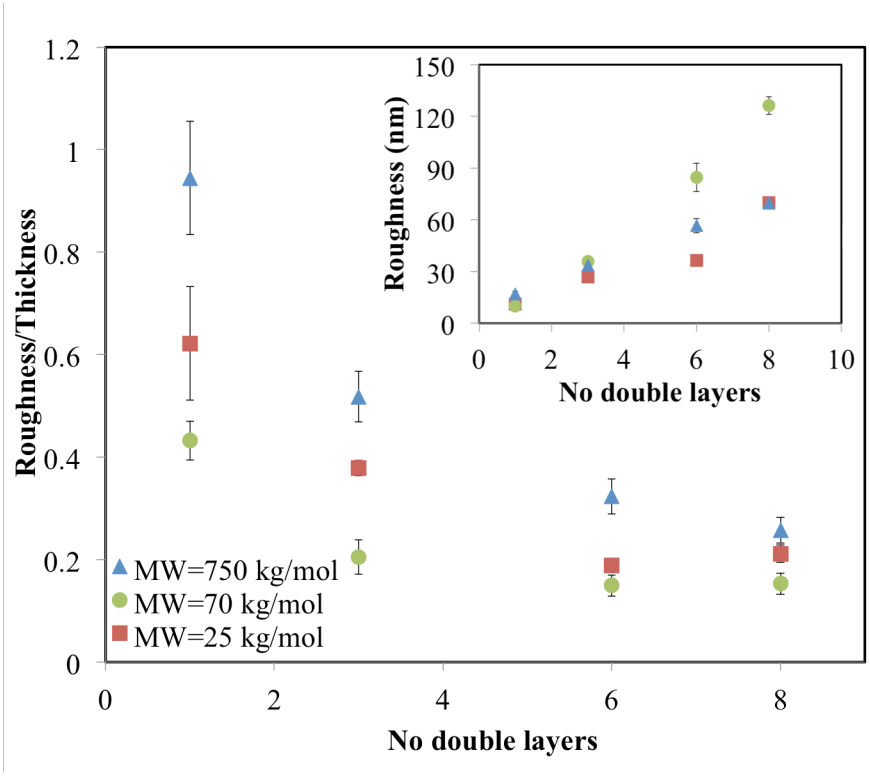

Fig. 3.12. Ratio of roughness to thickness, extracted from AFM images, for the PEI/PS- multilayers depicted in Fig. 3.11. The inset shows the variation of absolute roughness. For some data points, the error bar is too small to be visible.

Figure 3.12 shows that regardless of the MW of the PEI, as more layers are deposited onto the films, the ratio of roughness to thickness decreases while the absolute roughness increases. Further, Fig. 3.12 shows that PEI with intermediate MW has the least roughness to thickness ratio, perhaps due to the fast growth of its thickness. As can be seen in the inset to Fig. 3.12, LbL films composed of PEI with MWs of 25 and 750 kg/mol have comparable roughness values. Interestingly, these films had a similar rate of multilayer buildup (Fig. 3.4).

3.3.3.2. Scanning electron microscopy study

3.3.3.2.1. Effect of molecular weight

Figure 3.13 shows SEM micrographs of the surfaces of LbL films with different molecular weights of PEI, grown with the same materials and under the same conditions as for the AFM images in Fig. 3.11. At least five different regions of the samples were randomly selected to obtain the micrographs with magnifications of 400. Those chosen for Fig. 3.13 represent the typical features observed in the images. For micrographs with a magnification of 80,000, however, only three different parts of the samples were imaged, since different micrographs looked very similar to each other at this magnification.

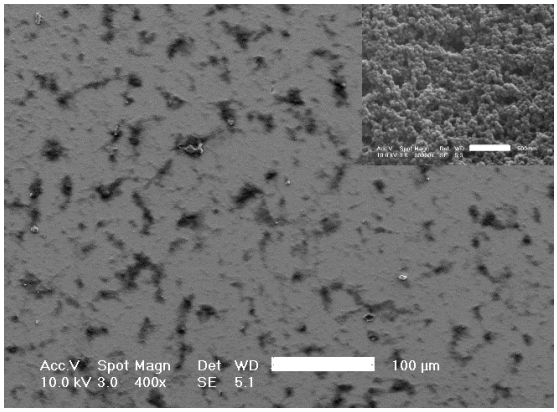

(a)

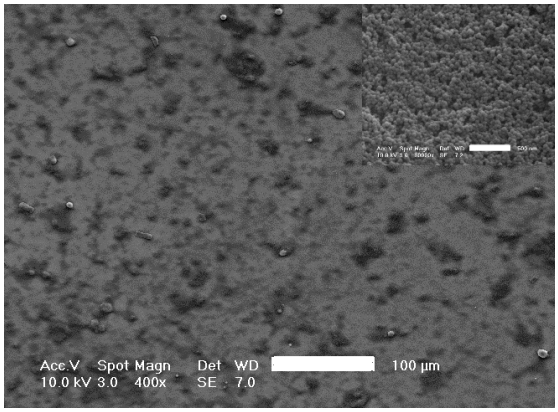

(b)

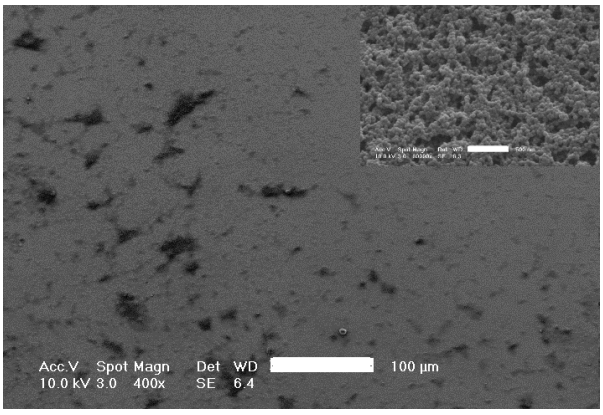

(c)

Fig. 3.13. Surface morphology of LbL films composed of 8 double layers of PEI and PS-, with the same materials and the same conditions as for Fig. 3.11, with PEI MWs of 25 kg/mol (a), 70 kg/mol (b), and 750 kg/mol (c). The main figures have a magnification of 400 while the insets have a magnification of 80,000.

The scale bars represent a length of 100 μm in the main figures, while those of insets indicate a length of 500 nm.

Figure 3.13 shows that the PEI/PS- multilayer film composed of PEI with MW of 70 kg/mol has a more heterogeneous surface than do the films for the other two molecular weights studied, which is consistent with the AFM results.

3.3.3.2.2. Thick film growth

PEI with a MW of 70 kg/mol and 41 nm sized PS- particles led to the thickest LbL film among different PEI/PS- composites studied in the previous sections. Thus, for this multilayer film, the LbL growth was continued until 59 double layers of PEI/PS- NPs were deposited on the glass substrate. Then, the surface morphology and thickness of the film were studied. Figure 3.14 depicts the characteristics of such composite obtained by SEM.

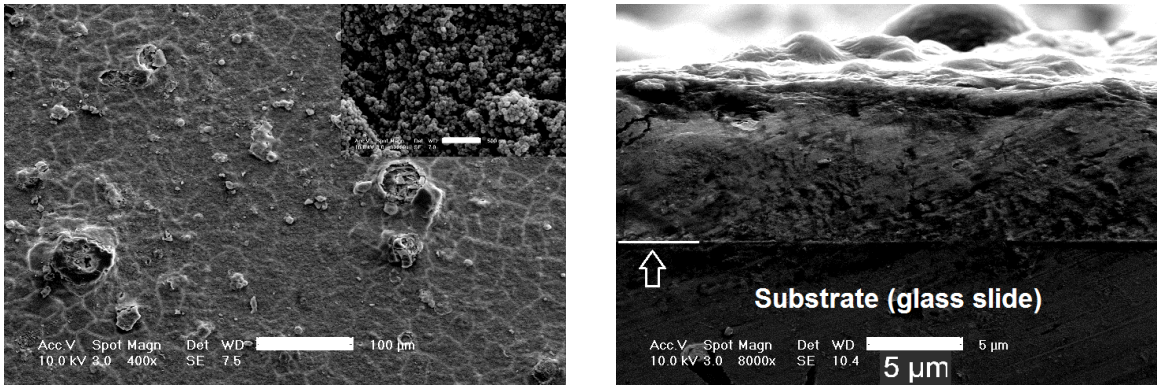

(a) (b)

Fig. 3.14. Characteristics of LbL film composed of 59 double layers of PEI and PS- NPs, with PEI MW of 70 kg/mol. PEI and PS- solutions were deposited at pH values of 9.9 and 7, respectively. No salt was used in either of the film ingredients except for the addition of HCl or KOH for pH adjustment. (a) Surface of the film with a magnification of 400 in the main figure and 80,000 in the inset. The scale bars show a length of 100 μm for the main figure and 500 nm for the inset. (b) Cross sectional view of the film with a magnification of 8,000. The arrow indicates the interface between the substrate and the film.

As can be seen in the surface micrograph (Fig. 3.14 (a)), the glass slide is completely covered by the film ingredients. There were some cracks and uneven features noticeable on the surface of the film however. Comparing the insets of Fig. 3.13 and Fig. 3.14 (a), more dark regions are observed in the latter, possibly indicating that the films are more disorganized and particles are more aggregated for the thicker film shown in Fig. 3.14 (a). Moreover, Fig. 3.14 (b) shows that a relatively thick film with thickness of few microns is deposited on the substrate. Film thickness was not uniform throughout the cross section and could have drastic variations. To be able to do SEM on the film cross section, the substrate was broken. As can be seen in Fig. 3.14 (b), film cross section is slightly scratched as a result of breaking the glass slide.

3.4. Conclusions

The effect of molecular weight (MW) of polyelectrolytes (PEs), type and charge of PE, nanoparticle size, pH, and salinity on the growth kinetics of polyelectrolyte (PE)/organic nanoparticle (NP) multilayer films were studied. First, it was found out that oppositely charged NPs alternately on top of each other could not be deposited in a manner that could survive rinsing steps, unless there are intervening polyelectrolyte layers. This shows that the polyelectrolyte and its binding and bridging of NPs is an essential mechanism for LbL film growth involving NPs. For both cationic poly(ethyleneimine) (PEI) deposited alternately with anionic polystyrene (PS-) NPs and for anionic poly(acrylic acid) (PAA) deposited alternately with cationic PS (PS+) NPs, an intermediate value of MW can (with some exceptions) lead to the fastest film buildup. This behavior can be explained as a trade-off between faster diffusivity for smaller chains during the deposition step at the expense of weaker adhesion and wash-off of particles during the deposition or rinse step when the MW becomes too low. However, for films composed of PEI with 26 or 100 nm sized particles, the PEI with the highest MW led to the thickest film.

The pH of PEI and PS- solutions had a dramatic influence on the LbL growth; in general, reducing the charge on the PEI by depositing it at higher pH caused greater deposition of PEI and of subsequent layers of PEI and NPs. Especially fast film growth was obtained by depositing PEI at pH = 9.9 and oppositely charged PS- NPs at 7.0. It was shown that salinity affects the growth kinetics of LbL films differently depending on MW of the PE. For low MW PEs, increasing the salt concentration decreased the film growth rate monotonically, while for larger PE MW, addition of salt first improved and then degraded the multilayer buildup.

3.5. Changing direction for drug delivery application

The overall goal of this PhD research was to develop a multidrug delivery implant. The initial plan was to synthesize such an implant with LbL assembly of drug loaded NPs and polyelectrolytes (Fig. 3.15-a). We hypothesized that once the implant is administered, the layers in the proximity of biological media degrade faster (Fig. 3.15-b), thus, by programming layers with different drug loaded NPs, drug release could be finely tuned (Fig. 3.15-c).

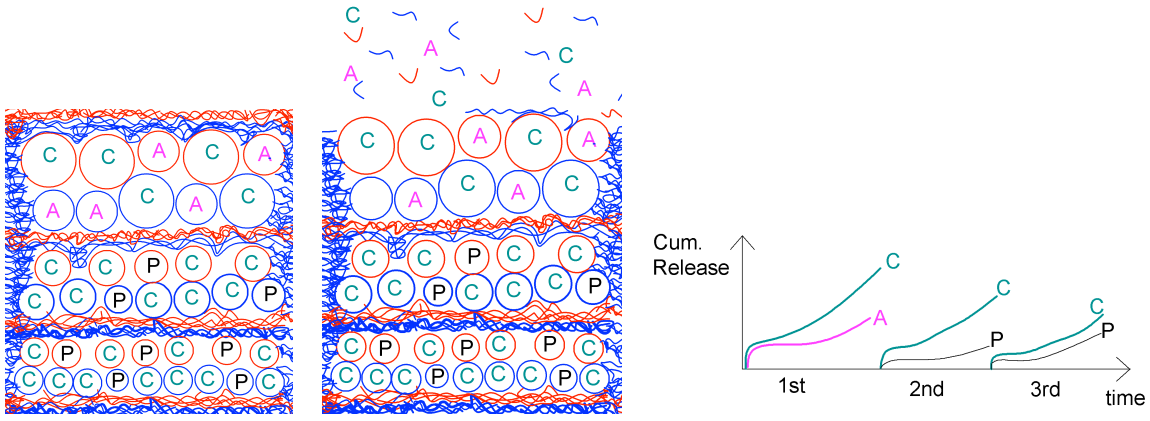

Fig. 3.15. a) Preliminary design of a colloidal LBL drug carrier. Letters of A, C, and P represent antibiotics, corticosteroid and IOP regulating agents, respectively that were planned to be loaded in the drug carrier. b) Schematic depiction of layered release of drug content, c) Desired cumulative drug release profile for each layer of drug delivery implant over time required by clinicians.

To achieve the goal of multidrug LbL implant, the plan was to perform layer growth optimization experiments with inexpensive polystyrene NPs, and to find the right parameters to achieve high film thickness. Then, the polystyrene particles would be replaced with valuable drug loaded NPs. Based on the results presented in this chapter, a comprehensive understanding of mechanism of growth of LbL films using polystyrene NPs was achieved. Results clearly showed that as NP size increase (around 100 nm), the growth of LbL films is considerably slowed down. It will be shown in the subsequent chapters that drug loaded particles should be large enough to have considerable loading and extended drug release duration. Jianshan Liao, a member of Larson Group took the lead on growing LbL films with biodegradable NPs, and she noticed that the growth of LbL films is much slower in this case.[38]

In addition, AFM and SEM micrographs presented in this chapter clearly showed very high surface roughness and irregularities and made us realize that programming layers of LbL films to fine tune the drug release profile is not a viable strategy. In chapter 4, using thermoresponsive hydrogels to formulate multidrug delivery vehicle is explained.

3.6. Acknowledgments

I would like to thank Ali Salehi for his valuable intellectual input, and help with designing the experiment and interpreting the results. Ryan Branch and Lucas Cygan are gratefully acknowledged for their contribution in performing the experiments. I would like to thank Prof. Nicholas A. Kotov for providing quartz crystal microbalance, and layer-by-layer assembly robot, and Dr. Cagri Besirli, Prof. Steven Schwendeman, and Douglas Montjoy for fruitful discussions. I would like to express gratitude to Dr. Kai Sun and Dr. Haiping Sun from Michigan Center for Materials Characterization for their assistance with AFM and SEM characterization. In addition, the support of the National Science Foundation, under grant DMR 1403335 is gratefully acknowledged. Any opinions, findings, and conclusions or recommendations expressed in this

material are those of the author and do not necessarily reflect the views of the National Science Foundation (NSF). I was a Howard Hughes Medical Institute International Student Research fellow while accomplishing this project and I am very grateful for this support. Moreover, the support provided by Paul R. Lichter, M.D. Research Discovery Fund is greatly appreciated.

3.7. References

1 Tokarev, I. & Minko, S. Stimuli-responsive hydrogel thin films. *Soft Matter* **5**, 511-524 (2009).

2 Kayaoglu, B. K., Gocek, İ., Kizil, H. & Trabzon, L. Functional nano and micro-scale thin film deposition on textiles: emerging technologies and applications. *Journal of Textiles and Engineer* **19**, 39-47 (2012).

3 Rahman, M. & Taghavinia, N. Layer-by-layer self assembly deposition and characterization of TiO2 nanoparticles by using a short chain polycation. *The European Physical Journal-Applied Physics* **48**, 10602 (2009).

4 De Villiers, M. M., Otto, D. P., Strydom, S. J. & Lvov, Y. M. Introduction to nanocoatings produced by layer-by-layer (LbL) self-assembly. *Advanced Drug Delivery Reviews* **63**, 701-715 (2011).

5 Kniprath, R. *et al.* Internal structure of nanoporous TiO2/polyion thin films prepared by layer-by-layer deposition. *Langmuir* **23**, 9860-9865 (2007).

6 Borges, J. & Mano, J. F. Molecular interactions driving the layer-by-layer assembly of multilayers. *Chemical Reviews* **114**, 8883-8942 (2014).

7 Chapel, J. P. & Berret, J. F. Versatile electrostatic assembly of nanoparticles and polyelectrolytes: Coating, clustering and layer-by-layer processes. *Current Opinion in Colloid & Interface Science* **17**, 97-105 (2012).

8 Costa, R. R. & Mano, J. F. Polyelectrolyte multilayered assemblies in biomedical technologies. *Chemical Society Reviews* **43**, 3453-3479, doi:10.1039/C3CS60393H (2014).

9 Liang, C. *et al.* Dual delivery for stem cell differentiation using dexamethasone and bFGF in/on polymeric microspheres as a cell carrier for nucleus pulposus regeneration. *Journal of Materials Science: Materials in Medicine* **23**, 1097-1107 (2012).

10 Na, K. *et al.* Heparin/poly (l-lysine) nanoparticle-coated polymeric microspheres for stem-cell therapy. *Journal of the American Chemical Society* **129**, 5788-5789 (2007).

11 Vrana, N. *et al.* Double entrapment of growth factors by nanoparticles loaded into polyelectrolyte multilayer films. *Journal of Materials Chemistry B* **2**, 999-1008 (2014).

12 Zhao, W., Xu, J. J., Shi, C. G. & Chen, H. Y. Multilayer membranes via layer-by-layer deposition of organic polymer protected Prussian blue nanoparticles and glucose oxidase for glucose biosensing. *Langmuir* **21**, 9630-9634 (2005).

13 Ma, J., Cai, P., Qi, W., Kong, D. & Wang, H. The layer-by-layer assembly of polyelectrolyte functionalized graphene sheets: a potential tool for biosensing. *Colloids and Surfaces A: Physicochemical and Engineering Aspects* **426**, 6-11 (2013).

14 Knowles, K. R., Hanson, C. C., Fogel, A. L., Warhol, B. & Rider, D. A. Layer-by-layer assembled multilayers of polyethylenimine-stabilized platinum nanoparticles and PEDOT: PSS as anodes for the methanol oxidation reaction. *ACS Applied Materials & Interfaces* **4**, 3575-3583 (2012).

15 Dubas, S. T., Kumlangdudsana, P. & Potiyaraj, P. Layer-by-layer deposition of antimicrobial silver nanoparticles on textile fibers. *Colloids and Surfaces A: Physicochemical and Engineering Aspects* **289**, 105-109 (2006).

16 Dubas, S. T., Wacharanad, S. & Potiyaraj, P. Tunning of the antimicrobial activity of surgical sutures coated with silver nanoparticles. *Colloids and Surfaces A: Physicochemical and Engineering Aspects* **380**, 25-28 (2011).

17 Nestler, P., Paßvogel, M. & Helm, C. A. Influence of polymer molecular weight on the parabolic and linear growth regime of PDADMAC/PSS multilayers. *Macromolecules* **46**, 5622-5629 (2013).

18 Shen, L., Chaudouet, P., Ji, J. & Picart, C. pH-amplified multilayer films based on hyaluronan: influence of HA molecular weight and concentration on film growth and stability. *Biomacromolecules* **12**, 1322-1331 (2011).

19 Yu, J., Sanyal, O., Izbicki, A. P. & Lee, I. Development of layered multiscale porous thin films by tuning deposition time and molecular weight of polyelectrolytes. *Macromolecular Rapid Communications* **36**, 1669-1674 (2015).

20 Zan, X., Hoagland, D. A., Wang, T., Peng, B. & Su, Z. Polyelectrolyte uptake by PEMs: Impacts of molecular weight and counterion. *Polymer* **53**, 5109-5115 (2012).

21 Rahman, M., Tajabadi, F., Shooshtari, L. & Taghavinia, N. Nanoparticulate hollow TiO2 fibers as light scatterers in dye-sensitized solar cells: Layer-by-layer self-assembly parameters and mechanism. *ChemPhysChem* **12**, 966-973 (2011).

22 Salehi, A., Desai, P. S., Li, J., Steele, C. A. & Larson, R. G. Relationship between polyelectrolyte bulk complexation and kinetics of their layer-by-layer assembly. *Macromolecules* **48**, 400-409 (2015).

23 Bieker, P. & Schönhoff, M. Linear and exponential growth regimes of multilayers of weak polyelectrolytes in dependence on pH. *Macromolecules* **43**, 5052-5059 (2010).

24 Peng, C., Thio, Y. S., Gerhardt, R. A., Ambaye, H. & Lauter, V. pH-promoted exponential layer-by-layer assembly of bicomponent polyelectrolyte/nanoparticle multilayers. *Chemistry of Materials* **23**, 4548-4556 (2011).

25 Ghannoum, S., Xin, Y., Jaber, J. & Halaoui, L. I. Self-assembly of polyacrylate-capped platinum nanoparticles on a polyelectrolyte surface: Kinetics of adsorption and effect of ionic strength and deposition protocol. *Langmuir* **19**, 4804-4811 (2003).

26 Ostendorf, A., Cramer, C., Decher, G. & Schönhoff, M. Humidity-tunable electronic conductivity of polyelectrolyte multilayers containing gold nanoparticles. *The Journal of Physical Chemistry C* **119**, 9543-9549 (2015).

27 Sennerfors, T., Bogdanovic, G. & Tiberg, F. Formation, chemical composition, and structure of polyelectrolyte-nanoparticle multilayer films. *Langmuir* **18**, 6410-6415 (2002).

28 Lvov, Y., Ariga, K., Onda, M., Ichinose, I. & Kunitake, T. Alternate assembly of ordered multilayers of SiO2 and other nanoparticles and polyions. *Langmuir* **13**, 6195-6203 (1997).

29 *Supplier, private communication* (2016).

30 Sauerbrey, G. Verwendung von schwingquarzen zur wägung dünner schichten und zur mikrowägung. *Zeitschrift für Physik* **155**, 206-222 (1959).

31 QCM200 Quartz Crystal Microbalance Digital Controller QCM225, 205 MHz Crystal Oscillator, Stanford Research Systems.

32 Choi, J. & Rubner, M. F. Influence of the degree of ionization on weak polyelectrolyte multilayer assembly. *Macromolecules* **38**, 116-124 (2005).

33 Petrov, A. I., Antipov, A. A. & Sukhorukov, G. B. Base-acid equilibria in polyelectrolyte systems: From weak polyelectrolytes to interpolyelectrolyte complexes and multilayered polyelectrolyte shells. *Macromolecules* **36**, 10079-10086 (2003).

34 Rubinstein, M. & Colby, R. H. *Polymer physics*. (Oxford University Press 2003).

35 Wang, Q. Charge inversion by flexible polyelectrolytes on flat surfaces from self-consistent field calculations. *Macromolecules* **38**, 8911-8922 (2005).

36 Picart, C. *et al.* Molecular basis for the explanation of the exponential growth of polyelectrolyte multilayers. *Proceedings of the National Academy of Sciences* **99**, 12531-12535 (2002).

37 Rief, M., Oesterhelt, F., Heymann, B. & Gaub, H. E. Single molecule force spectroscopy on polysaccharides by atomic force microscopy. *Science* **275**, 1295-1297 (1997).

38 Liao, J., Undergraduate research report, Unpublished document, (2016).

Chapter 4

Injectable Multi-drug Formulation for Postoperative Treatment Following Ocular Surgery

4.1. Introduction

More than 4 million ocular surgeries are performed every year in the US.[1] Careful management with topical medications is crucial for preventing post-operative complications including vision loss after ocular surgery.[2] Successful surgical outcome requires frequent applications of one or more ophthalmic drops over several days to several weeks and this process depends heavily on patient compliance. Similar to most other surgical procedures, incisional ophthalmic procedures carry a small risk of infection[3,4] and a more common physiologic reaction of inflammation in the immediate post-operative period.[5,6] Post-surgical inflammation as well as corticosteroid treatment may induce intraocular pressure (IOP) increase in many patients.[2,7-9] Increase in IOP may require additional topical treatment with ocular hypotensives, adding to the overall burden of treatment and decreasing patient adherence. In the later stages of surgical recovery, secondary complications including rebound inflammation and elevated intraocular pressure may cause morbidity, suboptimal vision, and on rare occasions may lead to vision loss and further surgery. Strict medication adherence in the post-operative period is necessary for preventing complications from inflammation, infection, and IOP elevation.[10-12] Numerous studies have shown that side effects of topically applied ocular agents and patient non-compliance are major contributing factors of therapeutic failure in ophthalmic diseases.[13]

The vast majority of ophthalmic drugs are marketed as topical formulations. The delivery of topical drug formulations is greatly hindered by the ocular surface barrier and availability is limited by rapid clearance from the ocular surface by the tear flow.[14,15] Despite these inherent

shortcomings, the most critical barrier for ophthalmic drug delivery continues to be poor patient adherence, limiting effective dosing and causing suboptimal therapy.[13,16,17] Patient adherence is affected by numerous factors, including decreased cognitive and motor function of geriatric patients, ocular surface irritation and allergic reaction with pain and discomfort caused by topical ophthalmic agents.[13,17-19]

Alternative ocular drug delivery mechanisms have been developed to replace topical drop administration, improving drug dosing and reducing side effects. These mechanisms employ distinct approaches to the drug delivery problem and include contact lenses, implants and hydrogels.[14,17,20-23] Although most are still in the pre-clinical development phase, a handful of products have received FDA approval and are available for patient use.[14,17]

Ocular drug implants can be categorized into different groups based on several characteristics including release duration, location of administration, and type of molecule delivered. The first FDA approved implant for ocular indications was Vitrasert® (Bausch & Lomb, Rochester, NY). It provided slow release of ganciclovir and was used to treat patients with cytomegalovirus retinitis.[14] Being a non-biodegradable implant, Vitrasert® uses two polymeric layers composed of poly vinyl alcohol (PVA) and ethylene vinyl alcohol (EVA) to deliver ganciclovir at a constant rate with therapeutic effectiveness for five to eight months.[14] This system had several disadvantages due to non-biodegradable design, including suboptimal biocompatibility and immunogenicity compared with a biodegradable system, and the need for vitreoretinal surgery for implantation and removal.[24,25] The next implant that was approved by FDA was Retisert® (Bausch & Lomb, Rochester, NY). This implant is not biodegradable and is composed of silicon and PVA layers. Retisert delivers fluocinolone acetonide for up to 2.5 years and is used to treat chronic non-infectious uveitis.[14] Similar to Vitrasert, Retisert® is inserted into the vitreous cavity via a transscleral route during vitreoretinal surgery. Some of the implant and surgical procedure-related complications of Retisert® include elevated IOP, detachment of retina, and formation of cataract.[14,26,27]

Ozurdex® (Allergan, Irvine, CA) is an implant for delivering dexamethasone to treat non-infectious posterior uveitis as well as macular edema secondary to diabetes and retinal vein occlusion.[14] Being the first FDA-approved biodegradable implant for ocular indications, dexamethasone is encapsulated in a poly(lactide-co-glycolide) (PLGA) matrix, and the implant is administered via intravitreal injection. Steroid is released from the implant for up to six months.[14] The adverse effects of Ozurdex® is similar to other implants releasing corticosteroid agents and include cataract formation and elevated IOP.[28,29]

Iluvien® (Alimera Sciences, Alpharetta, GA) is a next generation non-biodegradable intravitreal corticosteroid implant which was recently approved by FDA. Unlike Retisert®, Iluvien® does not require surgical implantation and is delivered into the vitreous cavity via transscleral injection. The implant releases fluocinolone acetonide to treat diabetic macular edema up to 3 years.[14] Similar to other corticosteroids, Iluvien® causes cataract formation and leads to elevated IOP.[30,31] Although this implant is not biodegradable, surgical removal is typically not required once the drug is depleted.

Other biodegradable implants are currently under development, including Verisome® (Icon Bioscience, Sunnyvale, CA). This drug delivery technology encapsulates different drug molecules and can maintain drug release up to a year after intravitreal injection.[14] A Dexycu® implant based on Verisome® technology releases dexamethasone and is currently being tested in a phase III clinical trial to treat post-operative inflammation after cataract surgery.[32]

The above-mentioned drug delivery systems are limited to a single agent and there is a need to develop a multi-drug delivery system. Thermoresponsive hydrogels are attractive solutions for long-term release of one or more therapeutics to the eye. In their optimal formulation, they are liquid at room temperature to ensure injectability while they form a depot for drug molecules once they are warmed up to body temperature. A-B-A triblock copolymers are particularly desirable for ocular drug delivery due to their biocompatibility and biodegradability. In these triblock copolymers, block A is a hydrophobic polymer such as PLGA, Poly(lactic acid) (PLA),

Poly(lactide-co-caprolactone) (PLCL), or Poly(caprolactone) (PCL) while block B is a hydrophilic polymer such as poly(ethylene glycol) (PEG). These triblock copolymers form micelles in the solutions with hydrophobic polymer forming the core, while the hydrophilic block will form the outer layer of the micelle that is in contact with water. With elevation of temperature, the number of micelles, and the association between them is augmented, leading to formation of a hydrogel network.[33]

Gervais reported the use of cyclosporine A-loaded PLGA-PEG-PLGA thermogels for the treatment of posterior capsule opacification, one of the sequelae of cataract surgery.[34] By dissolving their hydrophobic drug in ethanol at 100 mg/ml concentration and adding a small volume of that solution to a triblock copolymer solution, the authors were able to load the drug into the hydrogel. To study the drug release, they incubated 250 µl of hydrogel and used 250 µl of Dulbecco's modified Eagle medium as the release media. Their results showed a large burst release of drug one minute after initiation of the drug release experiment, with reduction in drug concentration over the next 24 hrs, albeit with drug level remaining detectable for up to a week after release. They noted that drug-releasing hydrogel should be modified to maintain drug concentration acceptable for longer duration and this will enable optimum therapeutic outcomes.

Xie et al. loaded Avastin®, a large monoclonal antibody in PLGA-PEG-PLGA hydrogels for the treatment of vitreoretinal diseases.[35] Fast drug release from the hydrogel appeared to occur despite large drug size. Even though Avastin® is orders of magnitude larger (molecular weight: 149 kDa) than other small molecules discussed above, the majority of it was nevertheless released within 8 hours post incubation. In general, the initial burst release of drug molecule followed by rapid reduction in drug concentration is not favorable for the long-term treatment of ocular diseases. The takeaway message from these valuable studies is that when relying on A-B-A thermogels, one cannot achieve a controlled drug release profile for a sustained period (i.e., longer than a month) and as a result additional resistance against premature drug leakage is

needed. In addition, A-B-A thermogels alone cannot be used to release multiple drug molecules with different drug release rates and durations.

Zhang et al. employed PLGA-PEG-PLGA hydrogels to prolong the release of dexamethasone.[36] Since the concentration of dexamethasone in the triblock copolymer solution was much higher than the drug solubility limit, it seems that dexamethasone "particles" were maintained within the polymer network. In addition, dexamethasone is very hydrophobic with low tendency to diffuse into aqueous media. These factors enabled enhancement of the release duration of dexamethasone for up to 18 days. They showed that by combining different triblock copolymer solutions, they were able to adjust the gelation temperature of the hydrogel and the dexamethasone release rate. However, still there is a therapeutic need to sustain the release of dexamethasone beyond even this period.

Hirani et al. synthesized PEG-PLGA nanoparticles loaded with triamcinolone acetonide and added the resulting nanoparticles to a PLGA-PEG-PLGA hydrogel network for the treatment of age-related macular degeneration (AMD).[37] Similar to previous studies, the majority of the reported release happened in the first 10 hours post incubation. However, since the drug molecule was encapsulated in the nanoparticles, Hirani et al. did not observe the huge burst release minutes after incubation reported by Gervais.[34] Since drug release is governed by the diffusion of molecules from the particles, nanoparticles are generally too small to control the release of the drug beyond a few hours or days. In addition, nanoparticles can aggregate easily which could alter their drug-release kinetics, and they are in general harder to lyophilize and store for the long term compared to microparticles (MPs).

Duvvuri et al. synthesized PLGA MPs encapsulating ganciclovir and loaded these into PLGA-PEG-PLGA hydrogels.[38] This enabled them to achieve sustained release of drug for more than a month. They programmed the drug release profile by blending the polymers used to make PLGA MPs as well as by mixing the particles made with different polymers. Microparticles synthesized in this study were more than 200 μm in size.

Polymers that are more hydrophobic than PLGA, e.g. PLA, PLCL, or PCL, will generally degrade more slowly. Thus, using those more hydrophoblic polymers to make thermoresponsive hydrogels could potentially lead to slower and more linear drug release over time. There have been only limited studies focusing on the use of these types of polymers to make thermoresponsive hydrogels for ocular drug delivery.[39,40] In addition, none of the current drug delivery technologies discussed above are designed to release multiple drug molecules while regulating release durations. A *multi-drug* delivery platform that temporally regulates drug release would be ideal for the treatment of many ophthalmic conditions, including post-operative management requiring multiple topical agents for inflammation, infection, and elevated IOP. For other ocular diseases including age-related macular degeneration, previous studies have shown that combination therapy using multiple drug molecules, benefiting from their synergistic effects, is more effective than single-drug therapy in many patients.[14,41] To address the shortcomings of existing technologies and fulfill an unmet need in ocular drug delivery, a novel drug delivery platform designed to release multiple drug molecules with precise temporal regulation is reported. This drug delivery system is administered via intraocular injection, and is composed of biocompatible and biodegradable materials for optimal ocular safety.

As an initial therapeutic target, the drug delivery system designed here is intended to address the challenges of multi-drug delivery during postoperative management of cataract surgery. In routine care after cataract surgery, topical antibiotics are administered for 7 days to reduce the risk of infection, whereas topical corticosteroids are applied up to a month with decreasing frequency to reduce inflammation.[10-12] Often an ocular hypotensive is added to the post-operative treatment regimen to reduce IOP increase secondary to inflammation and/or corticosteroid use.[2,7-9] Our drug delivery platform is designed to replace this topical treatment paradigm. In this formulation, a broad-spectrum antibiotic, 4th generation fluoroquinolone moxifloxacin, is designed to be delivered over a period of 7 days by adding it directly to the hydrogel network (Fig. 4.1-a). In addition, a potent corticosteroid, dexamethasone, is released from the drug

delivery system for more than a month to suppress inflammation. Because increased IOP is seen commonly with intraocular steroid implants, an ocular hypotensive agent, beta-blocker levobunolol,[42,43] is delivered to control IOP. The anti-inflammatory and hypotensive drugs are encapsulated in PLGA MPs, which act as barriers by which drug release can be controlled and made significantly slower than release from the hydrogel alone. The particles are embedded into hydrogels to further regulate the control of drug release (Fig. 4.1-a). With our innovative design, drug release rate and time for each agent (regardless of their hydrophobicity) can be individually controlled for specific ocular indications. This can be done by changing the amount and loading of MPs and the composition of the triblock copolymers as well as polymer used to synthesize the particles. Since this drug delivery platform is in liquid phase at room temperature (Fig. 4.1-b) and forms a hydrogel network at body temperature (Fig. 4.1-c), implantation is accomplished through direct injection into the anterior chamber or vitreous cavity after a surgical procedure or in office (Fig. 4.1-d)

Fig. 4.1. a) Our drug delivery platform enables delivery of at least three drug molecules. A broad-spectrum antibiotic (A) is added directly to the hydrogel network, while a potent corticosteroid (C) and ocular hypotensive agent (H) are encapsulated within the MPs and thereafter loaded into the hydrogel. b) The thermosensitive hydrogels are engineered to be liquids at room temperature, c) While they form a hydrogel network at body temperature. d) This eases the implantation via intraocular injections with a very small-guage needle and thus provides minimal invasiveness.

4.2. Description of the experiment

4.2.1. Materials

To make the hydrogels of the optimum formulation (liquid at room temperature and a hydrogel at body temperature), the following triblock copolymers were purchased from PolySciTech (West Lafayette, IN) and are called throughout this chapter with the product number:

AK12: PLGA-PEG-PLGA (with MWs of 1000:1000:1000 Da, ratio of lactic to glycolic acid (LA/GA): 1/1).

Ak91: PLGA-PEG-PLGA (with MWs of 1500:1500:1500 Da, LA/GA: 6/1).

AK100: PLA-PEG-PLA (with MWs of 1700:1500:1700 Da)

AK108: PLCL-PEG-PLCL (with MWs of 1600:1500:1600 Da, caprolactone (CL)/LA: 3/1).

AK109: PLCL-PEG-PLCL (with MWs of 1700:1500:1700 Da, CL/LA: 3/2).

Different types of PLGA were used to make drug loaded MPs. For levobunolol loaded MPs, PLGA (with LA/GA of 60/40 (Product number: AP43), 75/25 (Product number: AP18), or 85/15 (AP87), all with number averaged molecular weight of 45-55kDa) was purchased from PolySciTech. For dexamethasone-loaded MPs, PLGA (Resomer 503H with LA/GA ratio of 50/50 and weight averaged molecular weight of 24-38 kDa) was purchased from Evonik Corporation (Essen, Germany). Dexamethasone (Product number: 46165) and moxifloxacin (Product number: PHR1542) were obtained from Sigma Aldrich (St. Louis, MO), while levobunolol hydrochloride (HCl) (Product number: 1359801) was purchased from United States Pharmacopeia (Rockville, MD). Poly(vinyl alcohol) (PVA, with molecular weight of 13-23 kDa, product number: 363170) was obtained from Sigma Aldrich. All other materials were obtained from Sigma Aldrich. Unless noted otherwise, the materials were used as received without further purification.

4.2.2. Synthesis of microparticles

4.2.2.1. Deprotonation of levobunolol hydrochloride

To remove the HCl salt from levobunolol HCl, 30 mg of the drug was dissolved in dimethyl sulfoxide (DMSO) at a concentration of 97 mg/ml. A one-to-one mole ratio of triethylamine (TEA) was added to that and the solution was constantly inverted at a speed of 11 rpm for 3 hrs to obtain deprotonated levobunolol. The resulting drug solution was kept at room temperature protected from light and was used to make the MPs the next day.

4.2.2.2. Levobunolol loaded microparticles

100 mg PLGA (60/40, 75/25 or 85/15) was dissolved in dichloromethane (DCM) at a concentration of 61 mg/ml. This solution was added to 10.7 mg levobunolol previously dissolved in DMSO and deprotonated in the presence of TEA (total DMSO plus TEA volume: 115 ul). The polymer-drug solutions were then mixed and sonicated with a bath sonicator for 45 seconds and split in half. Each half was transferred to a 40 ml aqueous solution of 0.75% PVA during homogenization at a speed of 15,000 rpm for 1 minute. The resulting MPs were transferred to a larger bath of PVA (80 ml at a concentration of 0.5%) while stirring at a speed of 990 rpm for 3.5 hours. The MPs were pelleted by centrifugation at a speed of 3300 RCF for 5 mins, and washed three times with miliQ water. The MPs were then lyophilized and stored at -20 ^{o}C. To synthesize blank MPs, the same DMSO/TEA volume (115 ul) with no drug was mixed with PLGA solution in DCM.

4.2.2.3. Levobunolol hydrochloride-loaded microparticles

To make MPs loaded with levobunolol HCl, all the steps mentioned in the previous section were followed except that 10.7 mg of levobunolol HCl dissolved in DMSO at a concentration of 97 mg/ml was used as the drug solution, in place of deprotonated levobunolol.

4.2.2.4. Dexamethasone-loaded microparticles

Dexamethasone-loaded MPs were made following the same protocol as described for levobunolol, except that PLGA (50/50) was dissolved in DCM at a higher concentration of 68 mg/ml. In addition, 20 mg of dexamethasone was dissolved in DMSO at a concentration of 250 mg/ml and used as the drug solution.

4.2.3. Preparation of the hydrogel

To make the thermogels, the polymer solution is dissolved at a higher concentration than the intended concentration, so that liquid used to dilute the polymer solution to the right concentration, can also be used to add other components (e.g., addition of a drug molecule to polymer network or tonicity adjustment). Thus, even though the intended triblock copolymer concentration was 20 % wt/vol, the triblock copolymers were dissolved in milliQ water at a concentration of 28.6 % wt/vol by shaking while cold (2-8^{o}C) for 3 days. The triblock copolymer solutions were then diluted to reach the intended polymer concentration by addition of excess water and 10X PBS. The volume of 10X PBS addition was chosen so that the final formulations were at 1X PBS concentration to minimize any osmotic pressure difference with the biological environment (isotonic concentration).

Three different hydrogel types were developed, namely, PLGA-PEG-PLGA, PLA-PEG-PLA and PLCL-PEG-PLCL hydrogels by blending different triblock copolymers. The ideal triblock copolymer solution is one that is a liquid at room temperature to ensure injectability but forms a hydrogel network at body temperature. To achieve this, different polymer solutions need to be blended so that the gelation temperature is at around 37°C. The PLGA-PEG-PLGA was a 3/1 blend of AK91 and AK12 triblock copolymer solutions. The PLA-PEG-PLA hydrogel was made with AK100 triblock copolymer solution only, as its gelation temperature was in the right range.

Furthermore, PLCL-PEG-PLCL hydrogels were a 6/1 blend of AK108/AK109 triblock copolymer solutions. By blending different amounts of triblock copolymers, the gelation temperature can be finely tuned.

4.2.4. Hydrogel characterization

To characterize the hydrogels, two different schemes were implemented, namely a qualitative vial inversion test to determine the gelation temperature for each triblock copolymer solution and quantitative rheological measurements to determine the mechanical strength of the hydrogel at different temperatures.

To determine the phase diagram, copolymer solution at different concentrations of 10, 15, 20, and 25 % wt/vol was incubated at each set temperature point for 15 minutes. Subsequently, the vial was placed upside-down for 30 seconds and the triblock copolymer solution was visually inspected. If the polymer solution was not able to flow during this time, it was considered a gel. Otherwise, it was a liquid or precipitate. The precipitate could be clearly identified by eye in that the polymer had crashed out of the solution and solution was transparent.

Rheological experiments were performed using an ARES-G2 rheometer (TA Instruments, New Castle, DE) with a stainless steel rheometer plate with a diameter of 40 mm. This rheometer plate with a large diameter was chosen to maximize the torque signal generated by the triblock copolymer solution and enhance the accuracy of the data. Rheological experiments were performed with a temperature step of 3^{o}C. At each specific temperature, a strain sweep experiment was done at a frequency of 0.1 Hz to determine the linear viscoelastic region of the material. Afterwards, a frequency sweep was performed in the linear viscoelastic region to determine the values of moduli at different frequencies. The elastic modulus (G') is a measure of elasticity of the material (solid like behavior), while the viscose modulus (G") is a measure of viscosity of the material (viscose liquid like behavior).

4.2.5. Drug release studies

For the moxifloxacin, fast release of the drug in a week was desired, and as a result 500 μg of moxifloxacin was directly added to the hydrogel network. To do so, moxifloxacin solution at 12.5 mg/ml was prepared and 40 ul was added to the triblock copolymer solution. A longer duration of release is desired for dexamethasone and levobunolol. In addition, for each of these two drug molecules a different release profile is required. For dexamethasone, the amount of drug release should be high initially and gradually decrease over time. However, levobunolol release should be low initially and increase later on to suppress any ocular pressure increase in the postoperative treatment period.[44] To achieve this goal, these small drug molecules are encapsulated in MPs first and then the MPs are loaded in the hydrogel network. This provides two barriers against burst release and premature escape of the drug molecules. Unless noted otherwise, 7 mg of dexamethasone-loaded MPs and 17 mg of levobunolol-loaded MPs were loaded into the hydrogel network for drug release studies.

Hydrogels were made with 200 μl triblock copolymer solution and were kept in a 1.5 ml centrifuge tube. After incubation of hydrogel at 37^{o}C for half an hour, 1.2 ml of "pre-warmed" PBS was poured on it as the release media and the drug release was initiated. 1 ml of PBS was replaced with fresh PBS at certain intervals to make sure hydrogel was exposed to an effectively infinite-volume bath to release the drugs and to determine the released amount over time.

To assess the effectiveness of hydrogels in sustaining the release of drugs, the drug release from the MP-loaded hydrogels was compared with that of MPs alone. To do so, drug release from MPs was studied by incubating the same amount of MPs (7 mg of dexamethasone-loaded MPs and 17 mg of levobunolol-loaded MPs) in 1.2 ml 1X PBS. At certain timepoints, the tubes were centrifuged at 3000 RCF and 1 ml of PBS was replaced with fresh PBS. For the microparticle release samples, release media could evaporate over time (less than 7% in the worst case), even though the tubes were sealed with parafilm. The effect of evaporation of media on the release

results was taken into account. All drug-releasing hydrogels and MPs were shaken in a 37 ^{o}C incubator.

In addition to drug-releasing hydrogels and MPs, three hydrogel samples representing PLGA-PEG-PLGA, PLA-PEG-PLA, and PLCL-PEG-PLCL hydrogels loaded with blank MPs as well as a blank MP sample without hydrogel were made and incubated to serve as the negative controls and any signal from them (which was very small in most cases) was subtracted from that of drug-releasing samples.

4.2.6. Drug loading and release characterization

To determine the loading of dexamethasone and levobunolol, PLGA encapsulating the drug molecules in MPs was degraded by incubation of particles in a basic environment (1M NaOH) for 15 minutes at 37 ^{o}C. The resulting solutions were neutralized by addition of acid (1M HCl) and lyophilized. Next, the dried drug molecules were dissolved in DMSO, diluted by addition of excess methanol (DMSO/methanol: 1/10 volumetric ratio), centrifuged at a speed of 4,000 RCF for 5 mins and the supernatants were analyzed with high performance liquid chromatography (HPLC) in order to quantify the amount of drug loaded in the MPs. Loading was determined based on standard curves for each drug molecule with zero intercept. In this regard, dexamethasone was dissolved in water while levobunolol already in DMSO after deprotonation was diluted by addition of excess water. The drug solutions were turned into 1M basic environment by addition of same base volume at 2M concentration. Subsequently, the drug solutions were incubated at 37^{o}C for 15 minutes (to simulate the steps taken to measure drug loading) and were subsequently neutralized by addition of acid (1M HCl). The samples were lyophilized, and reconstituted in DMSO/Methanol (1/10 volumetric ratio), and analyzed with HPLC to determine the standard curve for drug loading.

The release media taken from hydrogels or MP-containing samples were lyophilized and drug molecules were reconstituted in DMSO/methanol (at 1/10 volumetric ratio). The resulting solution was centrifuged at 21,000 RCF and supernatant was analyzed with HPLC to quantify the amount of released drug. To determine the standard curve for the analysis of release samples, moxifloxacin and dexamethasone were dissolved in PBS. However, a small volume of levobunolol in DMSO solution (because of deprotonation) was diluted with excess PBS. Next, the drug solutions in PBS at different concentrations were incubated at 37 ^{o}C for 24 hrs (to mimic exposure of released drugs to 37 ^{o}C environment during drug release experiments), lyophilized and reconstituted in DMSO/methanol (1/10 volumetric ratio) and analyzed with HPLC to determine standard curve for drug release with zero intercept.

The mobile phase for HPLC was composed of mixture of acetonitrile (20%) and water (80%) for the first 9.5 minutes to elute levobunolol and moxifloxacin. Then a linear compositional ramp was induced and the proportion of acetonitrile was raised to 34% in 1 minute. The acetonitrile was then kept at 34% for 6.5 minutes to elute dexamethasone, which was a more hydrophobic compound than the other drugs studied. Levobunolol, moxifloxacin and dexamethasone signals were read at 221, 295 and 240 nm, respectively. The drug content was always checked with its UV absorption spectra to distinguish drug content from baseline oscillations. The flow rate of solvent was set to 1 ml/min, and injection volume of the drug solution was 25 µl.

4.2.7. Scanning electron microscopy

To determine the relative size of MPs and their surface morphology, a LEO/Zeiss scanning electron microscope (SEM) was utilized. In this regard, MPs were deposited on a SEM mount, and were coated with a thin (<20 nm) layer of gold-palladium during 2 minutes deposition at a pressure of 200 mTorr. Operating voltage was set to 1kV to minimize sample damage during

microscopy. At least four SEM micrographs from different parts of the samples at a magnification of 1000X were taken and the results shown are chosen to be representatives.

4.2.8. Error analysis

The drug release experiments were performed in duplicate. Error bars represent the standard deviations between replicate measurements.

4.3. Results

4.3.1. Particle characterization

Figure 4.2 illustrates the SEM micrographs taken from the MPs loaded with levobunolol or dexamethasone in this research.

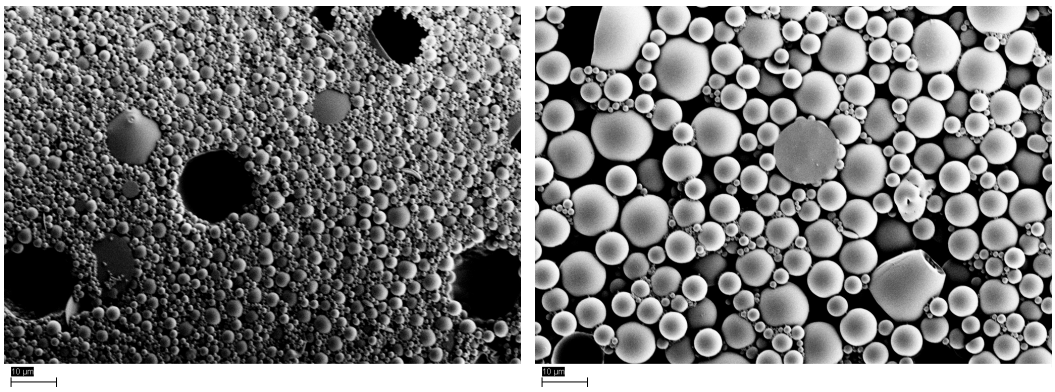

(a) (b)

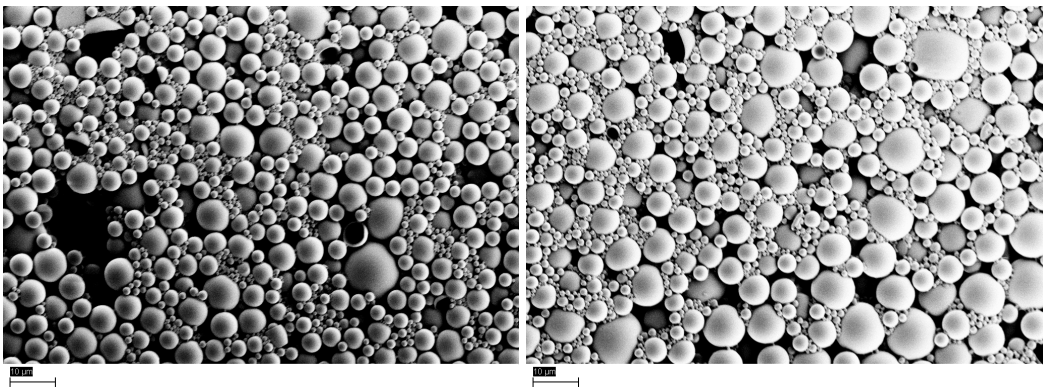

(c) (d)

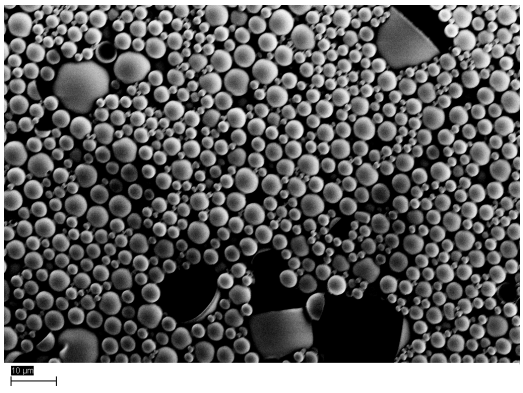

(e)

Fig. 4.2. SEM micrographs on a) levobunolol HCl-loaded MPs with 75/25 (lactic/glycolic acid ratio) PLGA, deprotonated levobunolol-loaded MPs with b) 60/40, c) 75/25 and d) 85/15 PLGA and e) dexamethasone-loaded MPs with 50/50 PLGA. All of the images were taken at a magnification of 1000, and scale bar shows a distance of 10 μm.

Figure 4.2 confirms the presence of spherical particles after loading different drug molecules and using different polymer types. There are some minor irregularities in the particle shapes that are mainly due to high polymer concentration in DCM to achieve high loading. There is a trade-off between smooth isotropic spherical shape and drug loading and it was found out that the selected polymer concentrations (68 mg/ml for dexamethasone and 61 for levobunolol loaded MPs) are compromise values to achieve high enough drug loading while ensuring acceptable particle morphology.

The loading of dexamethasone in MPs was found to be 3.2 μg/mg of MPs. In addition, the loadings of deprotonated levobunolol in MPs synthesized with 60/40, 75/25, and 85/15 PLGA were determined to be 6.9, 6.4, and 3.4 μg/mg of MPs, respectively. The loading of levobunolol HCl in MPs made with 75/25 PLGA was less than with the deprotonated version and was found to be 2.5 μg/mg of MPs. Levobunolol was a somewhat hydrophilic drug molecule (water solubility: 0.25 mg/ml[45]); thus, it is not naturally encapsulated in hydrophobic PLGA. Thus, the higher the hydrophobicity of the polymer, the less will be the loading of the levobunolol. In the subsequent sections, effect of deprotonating levobunolol on enhancing its hydrophobicity and increasing its loading in MPs is described.

4.3.2. Hydrogel characterization

Figure 4.3 illustrates the phase diagram for different triblock copolymers used in this study. All the formulations tested were at 1X PBS concentration.

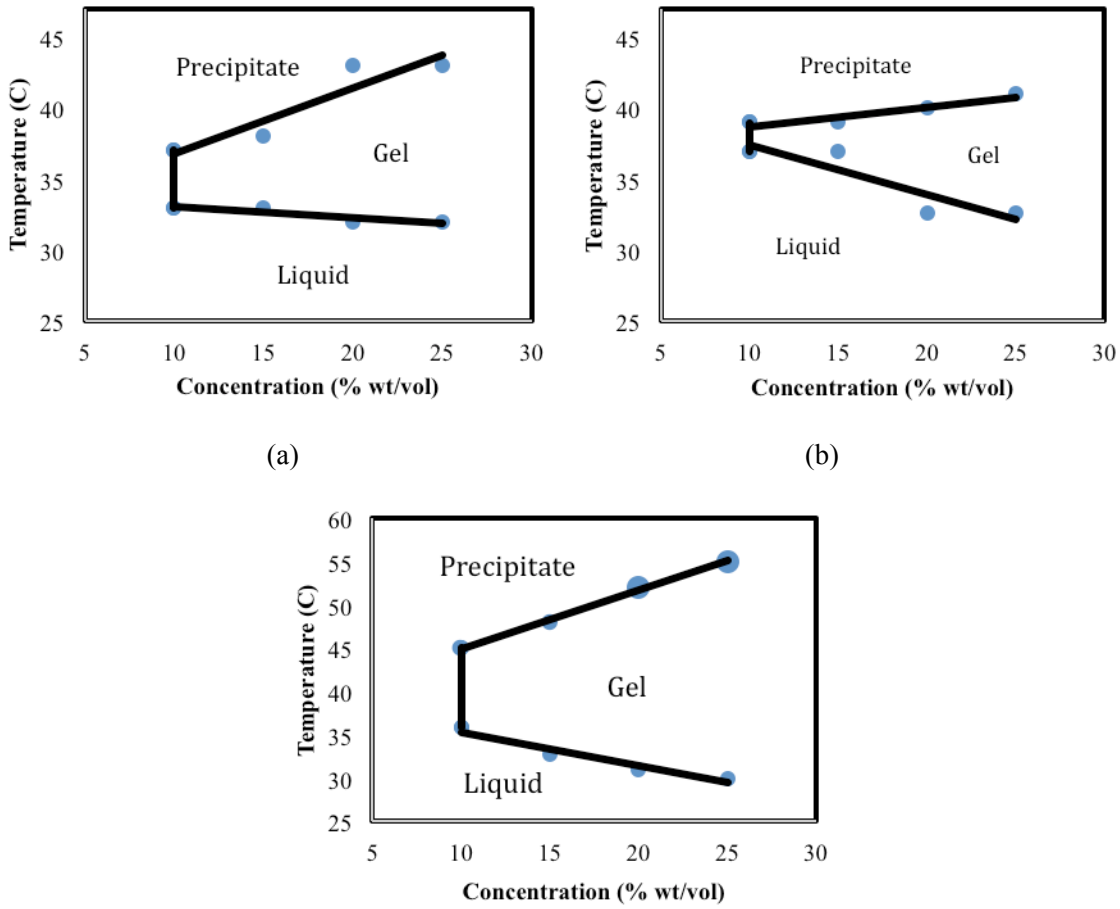

Fig. 4.3. Phase diagram for different triblock copolymers used in this research, a) PLGA-PEG-PLGA, b) PLA-PEG-PLA, c) PLCL-PEG-PLCL.

For PLGA-PEG-PLGA and PLCL-PEG-PLCL, two different triblock copolymers with different molecular weight and ratio of LA/GA, or CL/LA (as discussed in the Materials section) were blended to make sure that the resulting polymer solution was a liquid at room temperature and a gel at body temperature. PLA-PEG-PLA polymer solutions already possessed this property. Figure 4.3 confirms this and shows that at lower temperatures all of the polymer solutions are liquid. However, they will change into the gel form at around body temperature. Figure 4.3 also indicates that at very high temperatures, the polymers precipitate out of solution and can no longer form a gel network. According to Fig. 4.3, for each triblock copolymer concentration, there is a gelation temperature window. When the polymer concentration is increased, this

gelation window becomes wider. At very high polymer concentrations, there are enough micelles associated with each other that the triblock copolymer solution could form a hydrogel network even at room temperature. On the other hand, at lower polymer concentrations, the gelation window is too narrow to work with. As a result, in this research, the polymer concentration for all the hydrogels was set to 20% wt/vol. Interestingly, PLCL-PEG-PLCL polymer solutions have a much wider gelation window at each concentration, compared to PLGA-PEG-PLGA and PLA-PEG-PLA polymer solutions.

Figure 4.4 depicts the variation of storage and loss moduli for different triblock copolymers blended in this study. The polymer solution was formulated at 20% wt/vol in 1X PBS.

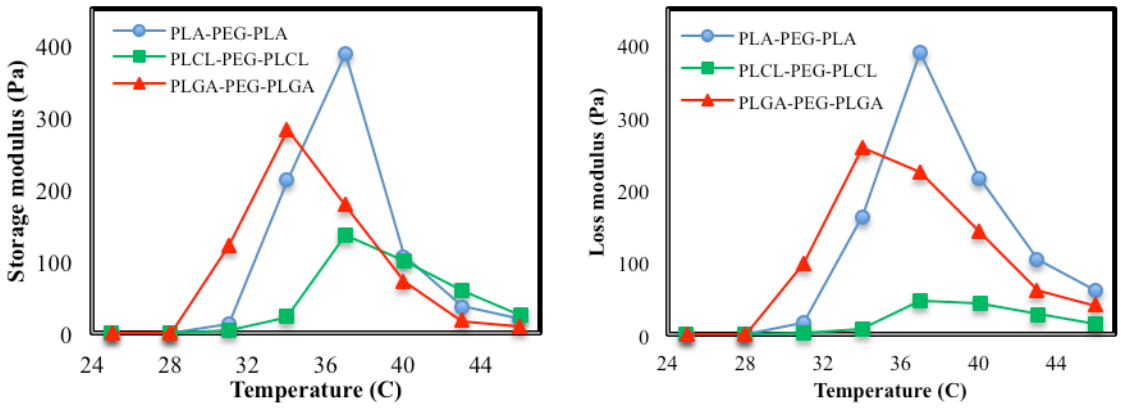

Fig. 4.4. Rheological results for different triblock copolymers; a) Storage modulus, b) Loss modulus. Results were obtained at 1Hz oscillation frequency. The PLGA-PEG-PLGA triblock copolymer was a 3/1 blend of AK91 and AK12. The PLA-PEG-PLA was AK100 only. The PLCL-PEG-PLCL was a 6/1 blend of AK108 and AK109.

Figure 4.4 shows that the resulting blend of triblock copolymers had a low value for both the storage and loss moduli at room temperature, indicating liquid-like behavior. However, with increasing temperatures, the mechanical properties of the gels shift as gelation occurs and the moduli are maximized near body temperature (37^{o}C). As temperature is further increased, the polymer precipitates and the desirable mechanical properties decrease. Quantitative rheological observations support the qualitative observations depicted in phase diagrams. Figure 4.5 depicts

the variations of the moduli with frequency at different temperatures for the PLCL-PEG-PLCL triblock copolymer solution.

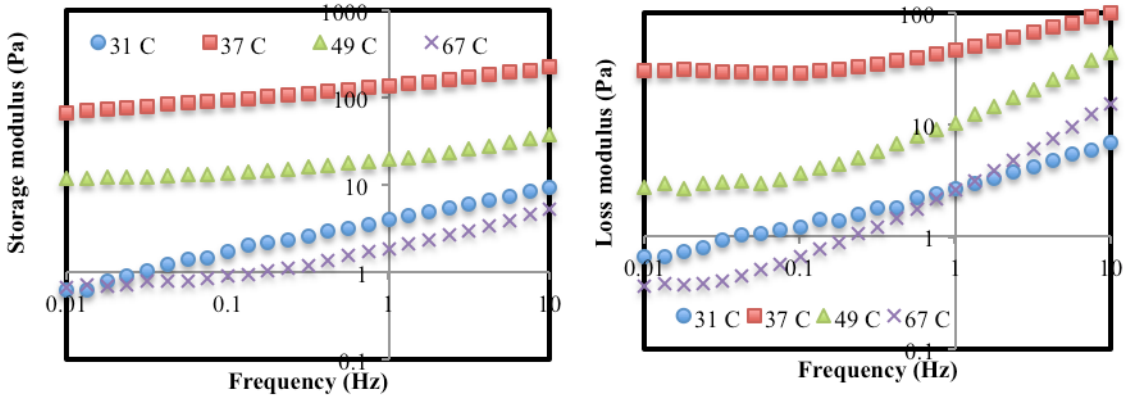

(a) (b)

Fig. 4.5. Variations of a) storage and b) loss moduli with oscillation frequency at different temperatures for PLCL-PEG-PLCL polymer solutions.

According to Fig. 4.5, regardless of oscillation frequency, the moduli are maximum at body temperature.

4.3.3. Effect of deprotonation on levobunolol loading and release

For ocular hypotensives, daily release on the order of 1 µg is required to ensure effectiveness of the molecule in reducing the ocular pressure.[46,47] Thus, a high loading of levobunolol in MPs was required to ensure the proper effect. To enhance the loading, levobunolol was deprotonated in the presence of TEA. A strong base like TEA attracts H+ ions, thus removing the HCl salt from the levobunolol and making it more hydrophobic due to removal of charged species. Deprotonation of levobunolol led to around 2.6-fold increase in its loading relative to the levobunolol HCl. To determine the effect of deprotonation on the drug release profile, two samples were made: one with 17 mg levobunolol-loaded MPs and the other with 17 mg of levobunolol HCl-loaded MPs both made with 75/25 PLGA. Both samples had 7 mg of dexamethasone-loaded MPs made with 50/50 PLGA added to them to check whether the presence of levobunolol would impact the

release of dexamethasone. Release results from these samples are compared in Fig. 4.6. As can be seen, the daily release of deprotonated levobunolol and its cumulative release is roughly 2.5 fold higher than the sample with levobunolol HCl. Thus, deprotonation enabled enhancing the daily release of levobunolol from the MPs.

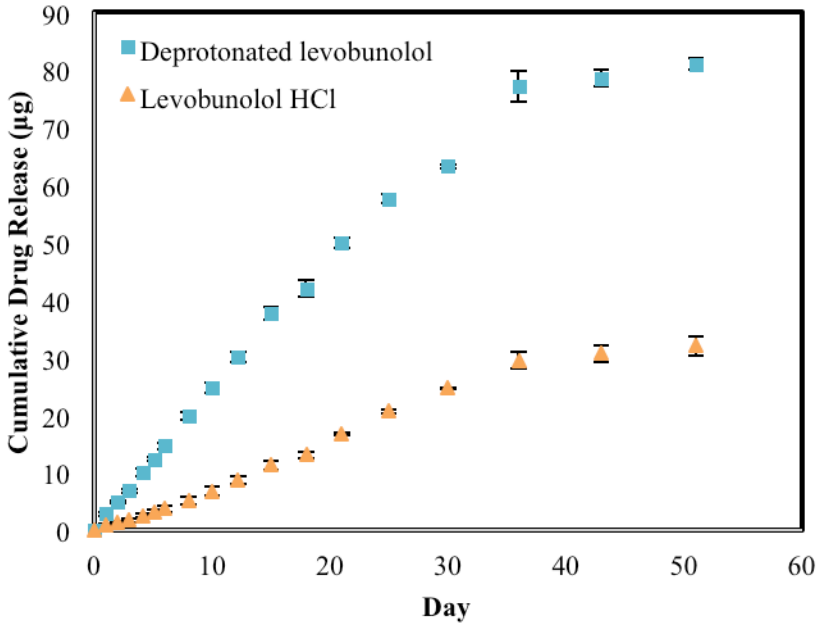

(a)

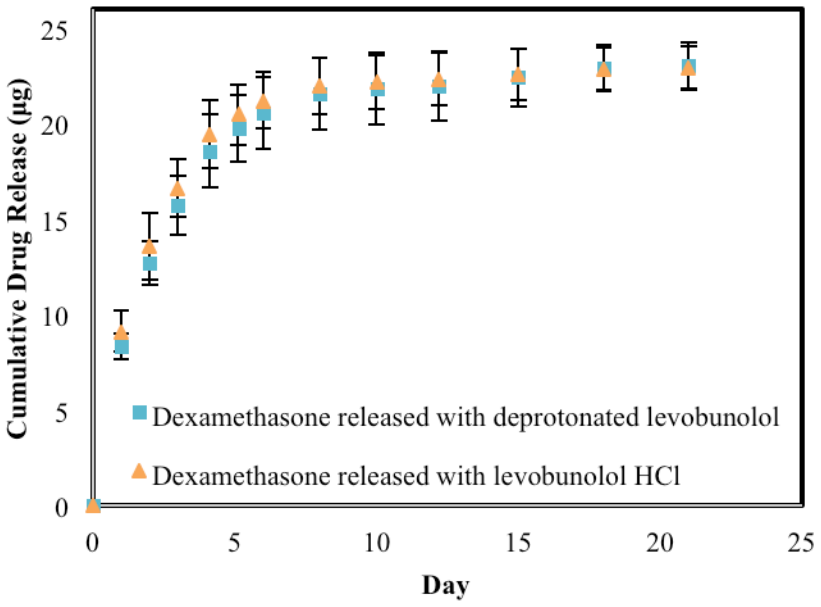

(b)

Fig. 4.6. (a) Comparison of release of levobunolol with levobunolol HCl from MPs. (b) Release of dexamethasone from samples containing different levobunolol type. For these samples no hydrogel was present and drug release from MPs alone was compared. In this and all of the subsequent figures, error bars represent standard deviations between duplicate measurements and data points represent average values of duplicate measurements.

Figure 4.6 also shows that daily release of dexamethasone from the two samples is the same, indicating that the presence of levobunolol MPs doesn't impact the dexamethasone release.

4.3.4. Effect of hydrogel on sustaining drug release

Next, the effect of the hydrogel network on sustaining the drug release from MPs was determined by comparing results of MPs in hydrogel with those for MPs alone. To do so, two samples were made: one containing 17 mg of deprotonated levobunolol MPs with 75/25 PLGA and 7 mg of dexamethasone loaded MPs with 50/50 PLGA, and the other a PLCL-PEG-PLCL hydrogel containing the same amount and type of microparticles plus 500 µg of moxifloxacin added directly to the hydrogel network. Figure 4.7 compares the amount of levobunolol and dexamethasone released from each sample.

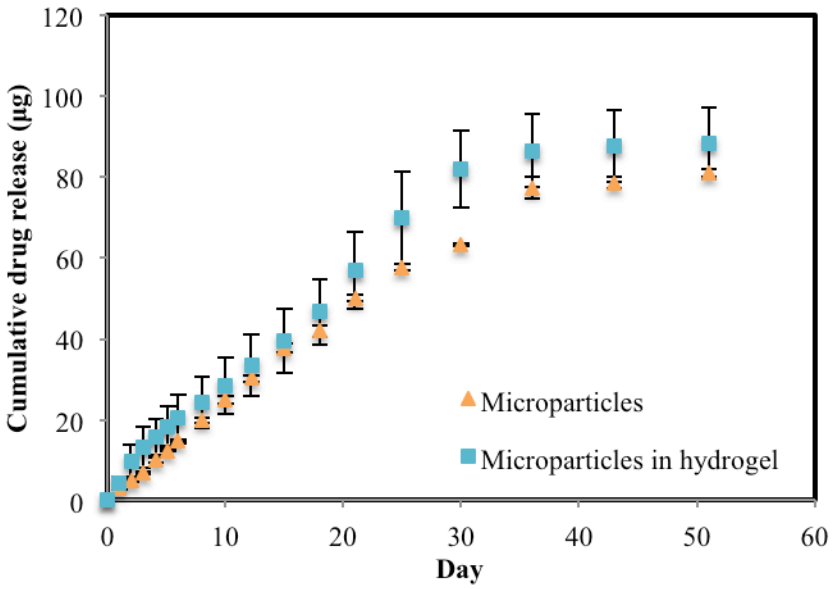

(a)

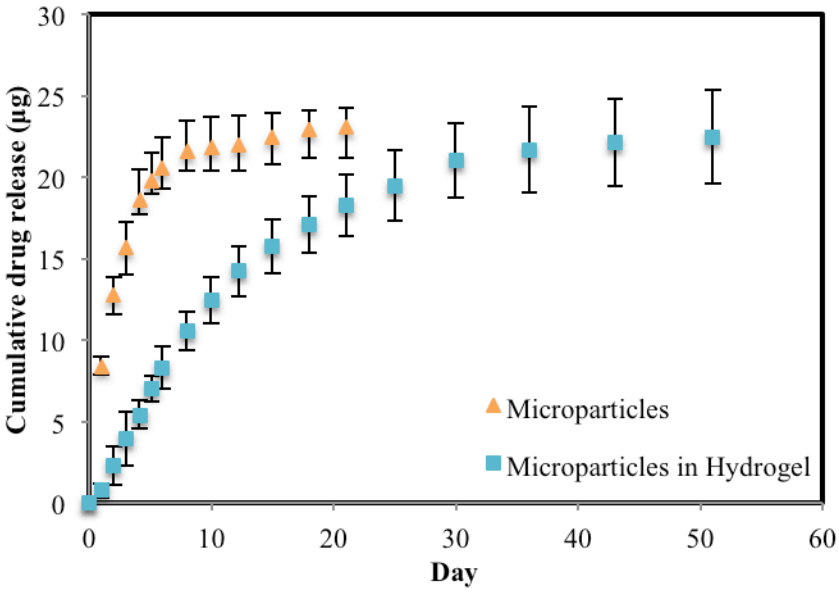

(b)

Fig. 4.7. Comparison of drug released from MP-loaded in PLCL-PEG-PLCL hydrogels with that from MPs alone, a) levobunolol, b) dexamethasone.

As can be seen in Fig. 4.7a, levobunolol release from MPs loaded in the hydrogel is nearly the same as that from MPs alone. Thus, the hydrogel does not seem to have much influence on the

release profile of levobunolol. On the other hand, release of dexamethasone from MPs in the hydrogel is considerably slowed down compared to release from MPs alone. Evident in Fig. 4.7b is the huge burst release of dexamethasone from MPs on day 1, which might be toxic for ocular cells. Also, for MPs, daily dexamethasone release is decreased abruptly over time and most of the drug is released within the first 5 days. However, for the MPs loaded in the hydrogel, burst drug release is eliminated and daily release of dexamethasone is constant for at least a week. Beyond the first week, daily drug release decreases gradually over time (which is greatly favorable for the clinical application). Dexamethasone release from MPs was detectable for up to 21 days, while for MPs in the hydrogel, the drug release was detectable for up to 51 days. As will be described in the subsequent section, if required, the drug release profile could be manipulated by varying the hydrophobicity of the polymer encapsulating the drug molecules. However, throughout the first month, daily release of dexamethasone was enough to have a therapeutically significant effect in accordance with literature. Notably, the amount of dexamethasone released to the vitreous cavity by implants should be between 0.2-1.2 ug daily initially, and the amount of drug should decrease gradually over time for postoperative management following cataract surgeries.[44,48]

The mechanism behind sustaining the dexamethasone release by the hydrogel mainly stems from their chemical interaction. Dexamethasone has a fluorine and several hydroxyl and double bonded oxygen groups that could form hydrogen bonds with excess water content in the hydrogel or with its PEG block. However, levobunolol does not have as many groups capable of forming hydrogen bonds. In addition, dexamethasone is very hydrophobic compared to levobunolol, and the tendency of dexamethasone to diffuse out of the hydrogel network and go into release media is therefore low. A-B-A triblock copolymers form a hydrogel network with large pore sizes (~50-100 μm),[35] and therefore can't physically avoid or slow down the release of small drug molecules studied in this research. As will be discussed in the subsequent section, the mechanical properties of the hydrogel network do not seem to effect the drug release kinetics, since drug release kinetics were found to be similar in hydrogels with significantly different moduli (Fig. 4.8-a).

Even though the PLCL-PEG-PLCL hydrogel did not have any effect on sustaining the release of levobunolol, still having the MPs in the hydrogel is more advantageous than administering MPs alone in the eye, since the hydrogel could hold the MPs in place, while the free MPs could potentially diffuse throughout the eye especially to the lens, interfere with vision and induce inflammation.

4.3.5. Effect of hydrogel type on drug release profile

Figure 4.8 depicts the effect of different hydrogel types on the release kinetics of moxifloxacin, dexamethasone and levobunolol, respectively.

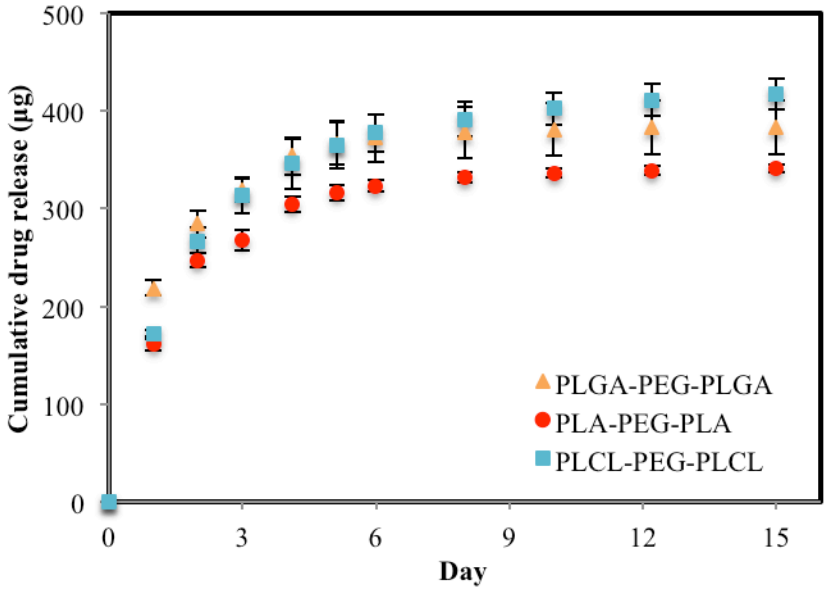

(a)

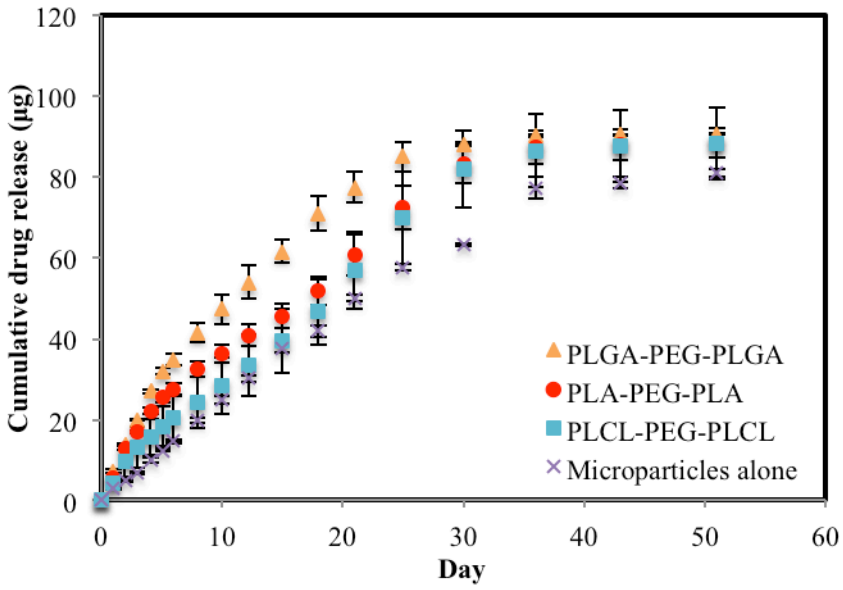

(b)

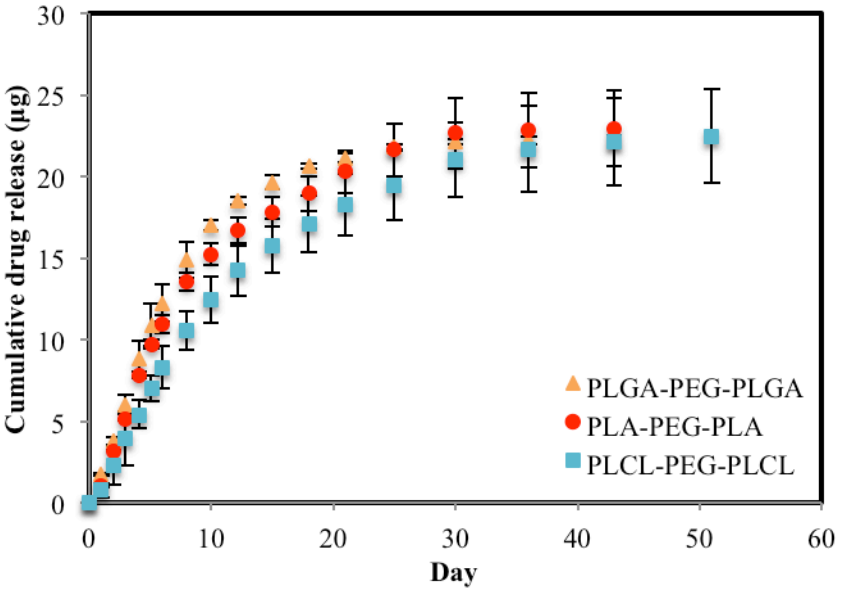

(c)

Fig. 4.8. Drug release kinetics for different types of hydrogels, a) Moxifloxacin, b) Levobunolol and c) Dexamethasone. Data points are the average between duplicate measurements and error bars represent standard deviation.

Moxifloxacin is a hydrophilic drug molecule (water solubility: 24 mg/ml), and was added directly to the polymer solution, and upon hydrogel formation, it will be held "loosely" within the

hydrogel network. Its release profile as shown in Fig. 4.8-a contains a high burst release followed by gradual decrease in daily drug release amount with the majority of the drug being released within a week. To explain the release requiring a week despite the absence of microparticles, we suggest that there might be some chemical interactions between the drug and hydrogel network such as hydrogen bonding between fluorine, hydroxyl and double-bonded oxygen groups in Moxifloxacin with excess water content in hydrogel or its PEG part that has slowed down the release of this drug. This release profile was favorable for meeting clinical requirements to avoid infection.[44,49] Figure 4.8-a also shows that there is not much difference in release kinetics of moxifloxacin between different hydrogel types. This is expected, as moxifloxacin was added directly to the hydrogel network and there was not a strong barrier against its release.

On the other hand, for levobunolol and dexamethasone, drug release from PLGA-PEG-PLGA hydrogels is faster than from PLA-PEG-PLA for the first three weeks. Also, the drug release from PLA-PEG-PLA seems to be faster than from PLCL-PEG-PLCL hydrogels over this period of time. This trend is more noticeable for levobunolol. Compared with release from microparticles alone, it seems that the PLGA-PEG-PLGA hydrogels have accelerated the release of levobunolol (Fig. 4.8b). This seems counter-intuitive, since the hydrogels are a barrier and if anything they should slow down the drug release rate. However, this trend makes sense when one considers the fact that by hydrolysis and cleavage of ester bonds of PLGA in PLGA-PEG-PLGA hydrogels, the degradation products make the environment acidic, leading to faster degradation of microparticles that are embedded in the hydrogel network.[50] The same phenomenon should happen by degradation of PLA-PEG-PLA and PLCL-PEG-PLCL hydrogels, but due to their higher hydrophobicity and slower degradation rate, it takes those hydrogels a longer time to make the environment acidic and thus their impact on acceleration of drug release is less pronounced.

4.3.6. Use of polymer type to fine-tune the drug release profile

Depending on the specific disease model and its progression, ophthalmologists might be interested in having different release durations of a specific drug molecule. To do so, the drug delivery platform should have the ability to finely tune the drug release profile. One way to achieve this goal is to vary the type of polymer encapsulating the drug molecule. To demonstrate this, deprotonated levobunolol loaded MPs were made out of PLGA with differing hydrophobicity and degradation rate with LA/GA ratios of 60/40, 75/25, and 85/15. A higher ratio of lactic to glycolic acid leads to greater hydrophobicity and slower degradation rate. Three hydrogel release samples were prepared each containing 17 mg levobunolol-loaded MPs with different PLGA polymer types mentioned above, plus 7 mg dexamethasone-loaded MPs and 500 µg moxifloxacin. PLCL-PEG-PLCL hydrogels were used for this experiment. Figure 4.9 depicts the levobunolol release profile from these hydrogels.

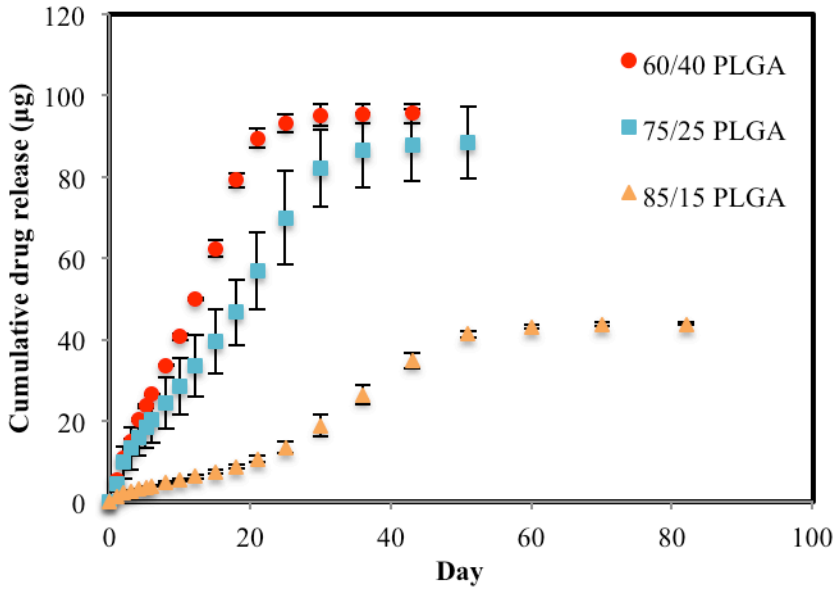

Fig. 4.9. Effect of polymer encapsulating levobunolol on regulation of release duration from the drug delivery system.

Evident in Figure 4.9 is the ability of the drug delivery platform to finely tune the drug release profile by simple variation of polymer used to encapsulate the drug molecule. PLGA with a

LA/GA ratio of 60/40 degrades faster and thus enables rapid and linear drug release kinetics. For this polymer, the majority of levobunolol release happens within 25 days. On the other hand, 85/15 PLGA is the most hydrophobic polymer and releases the drug molecule more slowly and sustain the drug release for up to 60 days. Interestingly, for this polymer an increase in the drug release content was observable on the fourth week of drug release. It is probably because by 4-week incubation at 37 ^{o}C, this highly hydrophobic PLGA has developed enough porous structure through degradation to allow the encapsulated drug molecules to escape the particles. Drug release from 75/25 PLGA is somewhere in between 60/40 and 85/15 PLGA with a slight increase in the drug release content in the second week. During the postoperative treatment period, elevation of ocular pressure as a side effect of steroids could happen during the second week for the patients.[7,44,51] Therefore, it is highly desirable to have a boost in release of levobunolol in this window for the proper postoperative management of ocular surgeries.

4.3.7. Varying the microparticle or moxifloxacin mass to tune the daily drug release

In the previous section, the ability to finely tune the drug release profile by varying the type of polymer encapsulating levobunolol was highlighted. Another flexibility of the presented drug delivery system is the freedom to vary the mass of dexamethasone or levobunolol loaded MPs or moxifloxacin encapsulated in the same amount of hydrogel to change the daily drug release while keeping the overall release profile relatively constant. In this regard, two PLCL-PEG-PLCL hydrogels were synthesized. In the first hydrogel group, 17 mg deprotonated levobunolol loaded MPs made with 75/25 PLGA, 7 mg dexamethasone loaded MPs made with 50/50 PLGA and 500 µg moxifloxacin were loaded. This group will be regarded as “full drug dosage.” While, in the second hydrogel category, half of the MPs and moxifloxacin mass were loaded in the hydrogel network and this hydrogel will be referred to as “half drug dosage.” Figure 4.10 compares the drug release from these two hydrogels.

(a)(b)

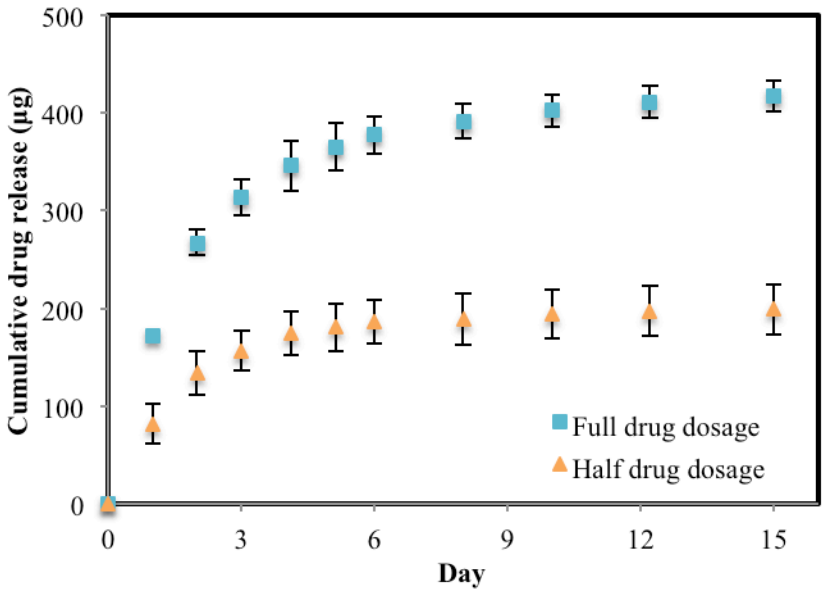
Cumulative drug release (µg)
500
400
300
200
100
0
0
3
6
9
12
15
Day
Full drug dosage
Half drug dosage

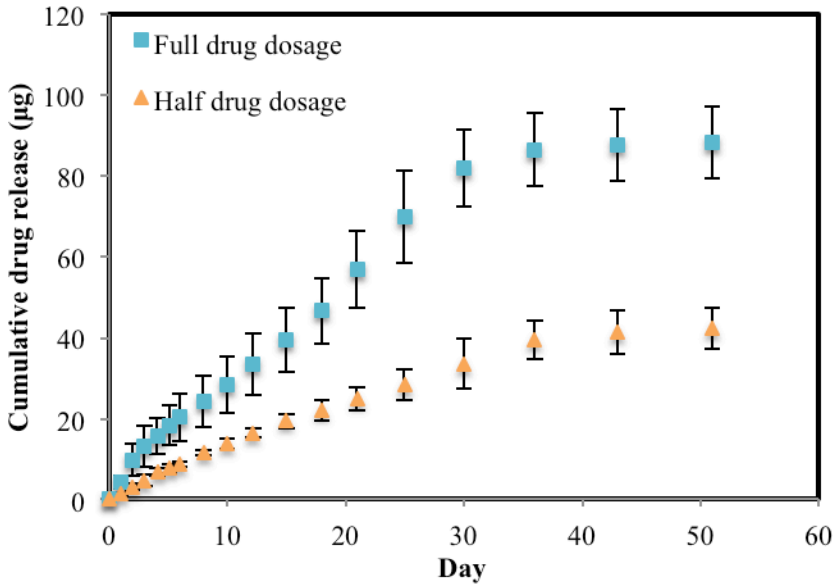
Cumulative drug release (µg)
120
100
80
60
40
20
0
0
10
20
30
40
50
60
Day
Full drug dosage
Half drug dosage

(c)

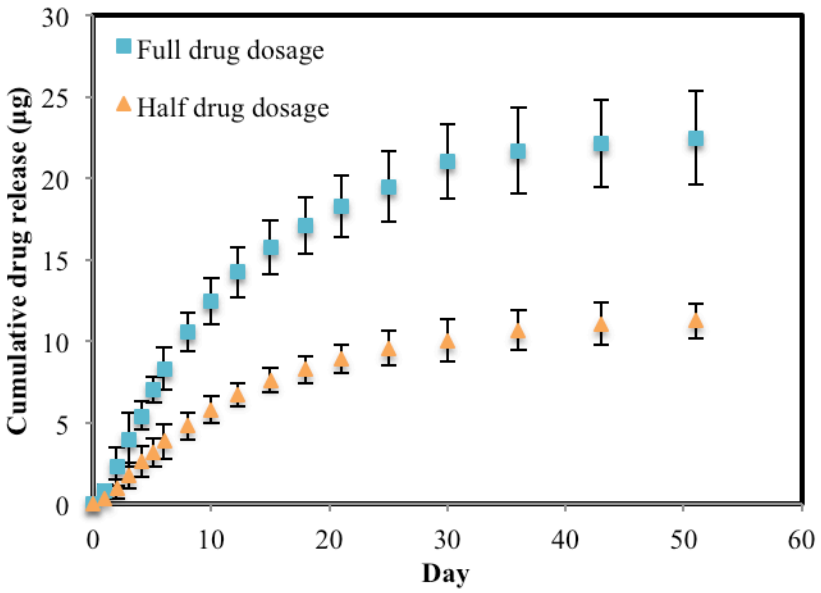

Fig. 4.10. Comparison of a) moxifloxacin, b) levobunolol and c) dexamethasone release profile when the loaded drug content is decreased by a factor of 2.

As can be seen in Fig. 4.10, by decreasing the amount of moxifloxacin dissolved in the triblock copolymer solution or by changing the mass of levobunolol or dexamethasone loaded MPs embedded in the hydrogel, one can vary the daily drug release content of each drug proportionally. However, the drug release profile remains relatively constant.

4.3.8. Multi-drug delivery hydrogel

Figure 4.11 depicts the variation in percent drug release over time for three different drug molecules loaded in the present multi-drug delivery platform. To determine the percent of drug release, drug release at each time point is divided by the maximum detected drug release from the hydrogel.

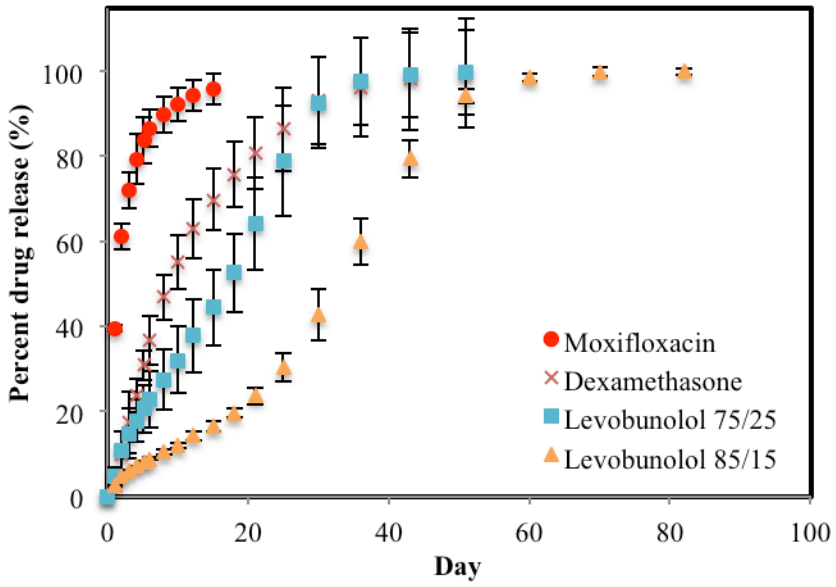

Fig. 4.11. A multi-drug delivery hydrogel capable of releasing three different drug molecules at different release rates.

Conspicuous in Figure 4.11 is the ability of the present drug delivery system to release different drug molecules regardless of their hydrophobicity over different durations chosen according to the application. Among the drug molecules chosen for this study, moxifloxacin was the most hydrophilic (water solubility: 24 mg/ml) and dexamethasone was the most hydrophobic drug (water solubility: <100 μg/ml[52]). Drug release duration could be adjusted on demand depending on the direct addition of drug to the polymer network (rapid drug release) or encapsulating the drug molecules in MPs and embedding the MPs in the hydrogel network (slow drug release). Even with the drug molecules loaded in the particles, the drug release profile could be modified depending on the polymer used to encapsulate the drug molecules. Using very hydrophobic polymer (85/15), one could achieve a slow drug release in the beginning followed by a rapid enhancement in drug release amount later on. However, with less hydrophobic polymers, more drugs could be released early on during the course of treatment.

4.4. Conclusions

In this chapter, the first hydrogel-enabled multi-drug delivery platform for the postoperative management following cataract surgery is reported. The main conclusions are highlighted below:

1) The drug delivery vehicle is a liquid at room temperature and forms a gel at body temperature. This allows delivery via simple intraocular injection, a common procedure during ocular surgery or in office patient visits.
2) An antibiotic, a steroid and an ocular hypotensive were successfully loaded in the hydrogel and were released over different periods and dosages according to clinical requirements. The antibiotic was added directly to the hydrogel network to ensure its fast release, while the steroid and ocular hypotensive were loaded in microparticles which were embedded in the hydrogel network to prolong their release duration. The complete system uses only biodegradable components.
3) By deprotonating the levobunolol hydrochloride, its loading into MPs and its daily release was enhanced considerably.
4) While there was not a significant difference between release of levobunolol from MPs compared to MPs loaded in PLCL-PEG-PLCL hydrogels, the hydrogel was able to eliminate the burst release of dexamethasone from MPs and prolong its release duration.
5) PLGA-PEG-PLGA hydrogels produce faster release of drug molecules than do PLA-PEG-PLA hydrogels. PLCL-PEG-PLCL hydrogels lead to the slowest and most linear drug release profile.
6) Depending on the type of polymer encapsulating the ocular hypotensive, drug release can be designed to be slow in the beginning, but increase later on to help reduce the elevated ocular pressure due to inflammation or the use of steroids. The transition point in between these two release stages can be tuned by varying the type of polymer and its degradation rate.

7) To change the daily release of drug molecules but not altering the drug release profile, one can vary the mass of dexamethasone or levobunolol loaded microparticles or moxifloxacin loaded in the hydrogel network.

4.5. Acknowledgements

I am grateful to Kisha K. Patel and Seyedeh P. Alaie for their assistance with the experiments. In addition, I would like thank Dr. Cagri Besirli and Stephany Tzeng for the fruitful discussions. I was supported by Howard Hughes Medical Institute International Student Research fellow and I am very grateful for this. The support of the National Science Foundation, under grant DMR 1403335 is gratefully acknowledged. Any opinions, findings, and conclusions or recommendations expressed in this material are those of the authors and do not necessarily reflect the views of the National Science Foundation (NSF). The support from National Institutes of Health under grant R21EY026148 is appreciated. The support provided by Paul R. Lichter, M.D. Research Discovery Fund is gratefully acknowledged.

4.6. References

1 http://ois.net/what-happened-at-spotlight-on-the-premium-channel-at-oisascrs.

2 Tyson, S. L., Bailey, R., Roman, J. S., Zhan, T., Hark, L. A., & Haller, J. A. Clinical outcomes after injection of a compounded pharmaceutical for prophylaxis after cataract surgery: a large-scale review. *Current Opinion in Ophthalmology* **28**, 73-80 (2017).

3 Garg, P., Roy, A., & Sharma, S. Endophthalmitis after cataract surgery: epidemiology, risk factors, and evidence on protection. *Current Opinion in Ophthalmology* **28**, 67-72 (2017).

4 Lundström, M., Friling, E., & Montan, P. Risk factors for endophthalmitis after cataract surgery: Predictors for causative organisms and visual outcomes. *Journal of Cataract & Refractive Surgery* **41**, 2410-2416 (2015).

5 Kessel, L., Tendal, B., Jørgensen, K. J., Erngaard, D., Flesner, P., Andresen, J. L., & Hjortdal, J. Post-cataract prevention of inflammation and macular edema by steroid and nonsteroidal anti-inflammatory eye drops: a systematic review. *Ophthalmology* **121**, 1915-1924 (2014).

6 Taravati, P., Lam, D. L., Leveque, T., & Van Gelder, R. N. Postcataract surgical inflammation. *Current Opinion in Ophthalmology* **23**, 12-18 (2012).

7 Pleyer, U., Ursell, P. G., & Rama, P. Intraocular pressure effects of common topical steroids for post-cataract inflammation: are they all the same? *Ophthalmology and Therapy* **2**, 55-72 (2013).

8 Chang, D. F., Tan, J. J., & Tripodis, Y. Risk factors for steroid response among cataract patients. *Journal of Cataract & Refractive Surgery* **37**, 675-681 (2011).

9 Fan, F., Luo, Y., Lu, Y., & Liu, X. Reasons for early ocular hypertension after uneventful cataract surgery. *European Journal of Ophthalmology* **24**, 712-717 (2013).

10 Shoss, B. L., & Tsai, L. M. Postoperative care in cataract surgery. *Current Opinion in Ophthalmology* **24**, 66-73 (2013).

11 Gower, E. W., Lindsley, K., Nanji, A. A., Leyngold, I., & McDonnell, P. J. Perioperative antibiotics for prevention of acute endophthalmitis after cataract surgery. *The Cochrane Library* (2013).

12 DeCroos, F. C., & Afshari, N. A. Perioperative antibiotics and anti-inflammatory agents in cataract surgery. *Current Opinion in Ophthalmology* **19**, 22-26 (2008).

13 Newman-Casey, P. A. *et al.* The most common barriers to glaucoma medication adherence: a cross-sectional survey. *Ophthalmology* **122**, 1308-1316 (2015).

14 Yasin, M. N., Svirskis, D., Seyfoddin, A., & Rupenthal, I. D. Implants for drug delivery to the posterior segment of the eye: A focus on stimuli-responsive and tunable release systems. *Journal of Controlled Release* **196**, 208-221 (2014).

15 Rawas-Qalaji, M., & Williams, C. A. Advances in ocular drug delivery *Current Eye Research* **37**, 345-356 (2012).

16 Newman-Casey, P. A. *et al.* Patterns of glaucoma medication adherence over four years of follow-up. *Ophthalmology* **122**, 2010-2021 (2015).

17 Kim, Y. C., Chiang, B., Wu, X., & Prausnitz, M. R. Ocular delivery of macromolecules. *Journal of Controlled Release* **190** 172-181 (2014).

18 Hugues, F.-C. & Le Jeunne, C. Systemic and local tolerability of ophthalmic drug formulations. *Drug Safety* **8**, 365-380 (1993).

19 Vaede, D., Baudouin, C., Warnet, J. & Brignole-Baudouin, F. Preservatives in eye drops: toward awareness of their toxicity. *Journal francais d'ophtalmologie* **33**, 505-524 (2010).

20 Maity, P., Moin, A., Gowda, D.V., Osmani, R.A.M. Ophthalmic drug delivery by contact lenses. *Journal of Chemical and Pharmaceutical Research* **8**, 644-651 (2016).

21 Hui, A., Willcox, M. In vivo studies evaluating the use of contact lenses for drug delivery. *Optometry and Vision Science* **93**, 367-376 (2016).

22 Maulvi, F. A., Soni, T.G., Shah, D.O. A review on therapeutic contact lenses for ocular drug delivery. *Drug Delivery* **23**, 3017-3026 (2016).

23 Kirchhof, S., Goepferich, A.M., Brandl, F.P. Hydrogels in ophthalmic applications *European Journal of Pharmaceutics and Biopharmaceutics* **95**, 227-238 (2015).

24 Chang, M., & Dunn, J. P. Ganciclovir implant in the treatment of cytomegalovirus retinitis. *Expert Review of Medical Devices* **2**, 421-427 (2005).

25 Kappel, P. J., Charonis, A. C., Holland, G. N., Narayanan, R., Kulkarni, A. D., Yu, F., Boyer, D.S., Engstrom, R.E., Kuppermann, B.D., Southern California HIV/Eye Consortium. Outcomes associated with ganciclovir implants in patients with AIDS-related cytomegalovirus retinitis. *Ophthalmology* **113**, 673-683 (2006).

26 Holbrook, J. T., Sugar, E. A., Burke, A. E., Vitale, A. T., Thorne, J. E., Davis, J. L., Jabs, D.A., and Multicenter Uveitis Steroid Treatment (MUST) Trial Research Group. Dissociations of the Fluocinolone Acetonide Implant: The Multicenter Uveitis Steroid Treatment (MUST) Trial and Follow-up Study. *American Journal of Ophthalmology* **164**, 29-36 (2016).

27 Jaffe, G. J., Martin, D., Callanan, D., Pearson, P. A., Levy, B., Comstock, T., & Fluocinolone Acetonide Uveitis Study Group. Fluocinolone acetonide implant (Retisert) for noninfectious posterior uveitis: thirty-four–week results of a multicenter randomized clinical study. *Ophthalmology* **113**, 1020-1027 (2006).

28 Tservakis, I., Koutsandrea, C., Papaconstantinou, D., Paraskevopoulos, T., & Georgalas, I. Safety and efficacy of dexamethasone intravitreal implant (Ozurdex) for the treatment of persistent macular edema secondary to retinal vein occlusion in eyes previously treated with anti-vascular endothelial growth factors. *Current Drug Safety* **10**, 145-151 (2015).

29 Sella, R., Oray, M., Friling, R., Umar, L., Tugal-Tutkun, I., & Kramer, M. Dexamethasone intravitreal implant (Ozurdex®) for pediatric uveitis. *Graefe's Archive for Clinical and Experimental Ophthalmology* **253**, 1777-1782 (2015).

30 Campochiaro, P. A., Brown, D. M., Pearson, A., Ciulla, T., Boyer, D., Holz, F. G., Tolentino, M., Gupta, A., Duarte, L., Madreperla, S., Gonder, J., Kapik, B., Billman, K., Kane, F., and FAME Study Group. Long-term benefit of sustained-delivery fluocinolone acetonide vitreous inserts for diabetic macular edema. *Ophthalmology* **118**, 626-635 (2011).

31 Cunha-Vaz, J., Ashton, P., Iezzi, R., Campochiaro, P., Dugel, P. U., Holz, F. G., Weber, M., Danis, R.P., Kuppermann, B.D., Bailey, C., Billman, K., Kapik, B., Kane, F., Green, K., for the FAME Study Group. Sustained delivery fluocinolone acetonide vitreous implants: long-term benefit in patients with chronic diabetic macular edema. *Ophthalmology* **121**, 1892-1903 (2014).

32 Study to Evaluate the Safety for the Treatment of Inflammation Associated With Cataract Surgery. *ClinicalTrials.gov*, Identifier:NCT02547623 (2015).

33 Shim, M.S., Lee, H.T., Shim, W.S., Park, I., Lee, H., Chang, T., Kim, S.W., Lee, D.S., Poly (D, L-lactic acid-co-glycolic acid)-b-poly (ethylene glycol)-b-poly (D, L-lactic acid-co-glycolic acid) triblock copolymer and thermoreversible phase transition in water. *Journal of Biomedical Materials Research Part A* **61**, 188-196 (2002).

34 Gervais, K. J. *Evaluation of a biodegradable thermogel polymer for intraocular delivery of cyclosporine A to prevent posterior capsule opacification* Master of Science thesis, The Ohio State University, (2017).

35 Xie, B., Jin, L., Luo, Z., Yu, J., Shi, S., Zhang, Z., Shen, M., Chen, H., Lia, X., Song, Z. An injectable thermosensitive polymeric hydrogel for sustained release of Avastin® to treat posterior segment disease. *International Journal of Pharmaceutics* **490**, 375-383 (2015).

36 Li, Z., Shen, W., Luan, J., Yang, D., Wei, G., Yu, L., Lu, W., Ding, J. Sustained intravitreal delivery of dexamethasone using an injectable and biodegradable thermogel. *Acta Biomaterialia* **23**, 271-281 (2015).

37 Hirani, A., Grover, A., Lee, Y. W., Pathak, Y., & Sutariya, V. Triamcinolone acetonide nanoparticles incorporated in thermoreversible gels for age-related macular degeneration. *Pharmaceutical Development and Technology* **21** 61-67 (2016).

38 Duvvuri, S., Janoria, K. G., Pal, D., & Mitra, A. K. Controlled delivery of ganciclovir to the retina with drug-loaded Poly (d, L-lactide-co-glycolide)(PLGA) microspheres dispersed in PLGA-PEG-PLGA Gel: a novel intravitreal delivery system for the treatment of cytomegalovirus retinitis. *Journal of Ocular Pharmacology and Therapeutics* **23**, 264-274 (2007).

39 Taich, P., Moretton, M.A., Del Sole, M.J., Winter, U., Bernabeu, E., Croxatto, J.O., Oppezzo, J., Williams, G., Chantada, G.L., Chappetta, D.A., Schaiquevich, P. Sustained-release hydrogels of topotecan for retinoblastoma. *Colloids and Surfaces B: Biointerfaces* **146**, 624-631 (2016).

40 Patel, S.P., Vaishya, R., Yang, X., Pal, D., Mitra, A.K. Novel thermosensitive pentablock copolymers for sustained delivery of proteins in the treatment of posterior segment diseases. *Protein and Peptide Letters* **21**, 1185-1200 (2014).

41 Englander, M., & Kaiser, P. K. . Combination therapy for the treatment of neovascular age-related macular degeneration. *Current Opinion in Ophthalmology* **24**, 233-238 (2013).

42 Silverstone, D. E., Novack, G. D., Kelley, E. P., & Chen, K. S. Prophylactic treatment of intraocular pressure elevations after neodymium: YAG laser posterior capsulotomies and extracapsular cataract extractions with levobunolol. *Ophthalmology* **95**, 713-718 (1988).

43 West, D. R., Lischwe, T. D., Thompson, V. M., & Ide, C. H. Comparative efficacy of the β-blockers for the prevention of increased intraocular pressure after cataract extraction. *American Journal of Ophthalmology* **106**, 168-173 (1988).

44 Besirli, C., MD PhD. Unpublished communication. (2017).

45 https://www.drugbank.ca/drugs/DB01210.

46 Tang-Liu, D.D.S., Neff, J., Sandri, R. Disposition of levobunolol after an ophthalmic dose to rabbits. *Journal of Pharmaceutical Sciences* **76**, 780-783 (1987).

47 Acheampong, A.A., Breau, A., Shackleton, M., Luo, W., Lam, S., & Tang-Liu, D. Comparison of concentration-time profiles of levobunolol and timolol in anterior and

posterior ocular tissues of albino rabbits. *Journal of Ocular Pharmacology and Therapeutics* **11**, 489-502 (1995).

48 Abdolrahimzadeh, S. *et al.* Twelve-month results of a single or multiple dexamethasone intravitreal implant for macular edema following uncomplicated phacoemulsification. *BioMed research international* **2015** (2015).

49 Lin, P., & de Juan Jr, E. *Principles and Practice of Intravitreal Application of Drugs, a chapter in Vitreous Health and Disease*. (Springer, 2014).

50 Zolnik, B. S. & Burgess, D. J. Effect of acidic pH on PLGA microsphere degradation and release. *Journal of Controlled Release* **122**, 338-344 (2007).

51 Wang, Q., Short-Term Intraocular Pressure Elevations after Combined Phacoemulsification and Implantation of Two Trabecular Micro-Bypass Stents: Prednisolone versus Loteprednol. *Journal of Ophthalmolmology* **2015**, 341450 (2015).

52 https://www.drugbank.ca/drugs/DB01234.

Chapter 5

Blocking Expression of Hypoxia Inducible Factors with Sustained Release Strategies

5.1. Introduction

In order to produce ATP and enable several reactions in the human body, cells are in need of an oxygen supply. Therefore, hypoxia (lack of oxygen) adversely impacts cellular mechanisms in the body. The response of the cells to lack of oxygen is controlled by hypoxia inducible factors (HIF).[1] HIF is a protein that has two different subunits of HIF-1α and HIF-1β. In vertebrates, HIF has two subunits of HIF-2α and HIF-1β.[1] Due to their irregular vasculature growth and proliferation of cells, solid tumors often have highly hypoxic regions. HIF is shown to be a master regulator and have a profound influence on tumor growth, metastasis, angiogenesis, ineffectiveness of chemotherapy, and ultimately patient death.[1,2] HIF has also been shown to significantly promote angiogenesis and formation of new blood vessels in the diseases of the back of the eye, including diabetic retinopathy leading to blindness.[3,4] Thus, inhibition of the HIF could improve the treatment outcomes for patients with cancers or ocular diseases.

Certain FDA-approved molecules have been identified as having HIF-1 inhibition activity, including acriflavine (Acr), and doxorubicin (Dox).[1,2,5] Depending on the molecule type, their mechanism of action is different. Acr interferes with interaction of different subdomains of HIF protein, and consequently avoids transcription of genes related to HIF. On the other hand, through binding to DNA, Dox impacts binding of HIF to cells.[1,5] Also, it has an impact on inhibition of growth factor expression related to angiogenesis.[1] Recently, limited patients' response to conventional anti-vascular endothelial growth factors (VEGF) therapies has brought about questions about their effectiveness. As a master regulator, if HIF is targeted rather than VEGF

(which is also regulated by HIF), improvement in treatment outcomes could occur. As a result, using HIF inhibitors alone or in combination with conventional anti-VEGF is a promising avenue in the treatment of patients with cancer or eye diseases.[1] There are excellent reviews about HIF and its role on disease progression for the patients with cancer or ocular diseases.[1,6-8]

The majority of HIF inhibitors are small molecules. They have a blood half-life on the order of few minutes and thus they are cleared by the body very fast. As a result, free small molecules have minimum duration of action. They require frequent drug administration and could increase the risk of patient noncompliance. In addition, since the drug molecules are cleared from body fast, higher drug dosages would need to be applied so that adequate drug reaches the target site and be effective for preventing HIF expression. However, high drug dosage could lead to serious side effects.[9-11] To overcome these challenges, the small drug molecules could be encapsulated in sustained release vehicles (e.g. nanoparticles (NPs)) and administered to the body. For the case of cancer, NPs could be accumulated in the tumor following intravenous injection. This is due to the enhanced permeability and retention (EPR) effect. Tumor has leaky vasculatures, compared to normal body organs, and thus enables higher NP accumulation.[12] As NPs biodegrade, they gradually release the drug molecules for several days. The aim of the work presented in this chapter was to synthesize NPs loaded with Acr and Dox. NPs should have a small size (<200 nm) and high drug loading (>10 μg/mg of NPs). NPs are engineered to have polyethylene glycol on their surface to reduce their interaction with blood constituents and enhance their half-life in the blood.[16] The drug release profile from the NPs and their impact on inhibition of HIF expression was evaluated *in vitro*. Finally, the impact of NPs on inhibiting HIF and reducing angiogenesis was studied *in vivo* in two animal models.

5.2. Description of the experiment:

5.2.1. Materials

Dox and Acr were purchased from Sigma Aldrich (St. Louis, MO). poly(D,L-lactic-co-glycolic acid) (PLGA, Resomer 502H with lactic acid (LA)/glycolic acid (GA) ration of 50/50 and molecular weight of 7-17 kDa) was ordered from Evonik Corporation (Essen, Germany). PEGylated PLGA (with 50/50 ratio of LA/GA for PLGA, MWs of 5 and 20 kg/mol for PEG and PLGA, respectively) was obtained from Polyscitech (West Lafayette, IN). Cye7.5 was used as near infrared dye and was obtained from Lumiprobe (Cockeysville, MD). All other chemicals were ordered from Sigma Aldrich and the materials were used as received without further purification (unless noted otherwise).

5.2.2. Doxorubicin loaded nanoparticles

5.2.2.1. Deprotonation of doxorubicin hydrochloride

The protocol to deprotonate Dox was adopted from James Shamul, a member of Green Lab.[17] Dox hydrochloride (Dox HCl in brief) was deprotonated at a concentration of 2.5 mg/ml in dimethylsulfoxide (DMSO) in the presence of three times excess moles of triethylamine (TEA). To do so, the mixture of Dox solution and TEA was stirred at 170 rpm for 3 hrs for the reaction to accomplish. Deprotonated Dox was refrigerated till it was used.

5.2.2.2. Synthesis of doxorubicin loaded NPs

The Dox loaded NPs were made with single emulsion method following previous literature[13] with several modifications to enhance Dox loading and reduce the particle size. 50 mg of PEGylated PLGA was dissolved in dichloromethane (DCM) at a concentration of 10 mg/ml. 2 ml of deprotonated Doxsolution was mixed with PEG-PLGA solution in DCM. The mass ratio of drug to polymer was 10%. The resulting solution was sonicated at 60% amplitude for 45 seconds to

ensure proper mixing of the polymer and drug solution. Subsequently, the solution was added to 10 ml of 2% polyvinyl alcohol (PVA) that was being sonicated at 60% amplitude for 3 minutes. Afterwards, the resulting Dox loaded NPs were added to 50 ml of 0.5% PVA that was being mixed at a speed of 500 rpm for 3 hrs. This ensures the evaporation of DCM and hardening of NPs. To reduce the NP size and polydispersity, the NPs were centrifuged at a speed of 8,000 RCF for 10 mins and the pellet was discarded. The NPs in the supernatant were washed three times with miliQ water. The washed NPs were resuspended in water and frozen at -80 ^{O}C. Before use, NPs were thawed, and concentrated (if required).

For some experiments blank NPs were needed as control. To synthesize those NPs, all the steps mentioned above to synthesize Dox loaded NPs were followed, except instead of Dox solution, 2ml DMSO was added to polymer solution

5.2.2.3. Synthesis of dye loaded NPs

To determine the biodistribution of the Dox loaded NPs, NPs were co-loaded with Dox and near infrared dye (Cye7.5, excitation wavelength: 800 nm, emission wavelength: 830 nm). To do so, the same steps were followed as described for the synthesis of Dox loaded NPs, except 0.5 mg dye dissolved in DMSO at a concentration of 10 mg/ml was mixed with Dox solution in DMSO.

For the biodistribution study, there was an arm with dye loaded NPs only, to assess the impact of Dox loading on biodistribution. To synthesize these NPs, all the steps to synthesize dox+dye loaded NPs were followed, except instead of 2 ml of Dox solution in DMSO, 2 ml of DMSO was used.

5.2.3. Acr loaded NPs

Unlike deprotonated Dox, Acr is extremely hydrophilic (water solubility: 330 mg/ml according to the manufacturer[14]), and it is challenging to load it in NPs with hydrophobic PLGA core. As a result, different techniques were tried to synthesize Acr loaded NPs.

5.2.3.1. Nanoprecipitation

PEGylated PLGA was dissolved in DMSO at a concentration of 10 mg/ml. To that Acr or Acr hydrochloride (Acr HCl in brief) was dissolved in the same solution to have a drug to polymer mass ratio of 0.1. The polymer-drug solution was added dropwise to a beaker containing 10 times higher volume of water that was being stirred at a speed of 500 rpm. NPs were washed after around 3 hrs, using amicon centrifuge tubes. For the case of Acr, instead of DMSO, dimethylformamide (DMF) was used as well to see its impact on NP size and loading.

5.2.3.2. Double emulsion method

20 mg of PEGylated PLGA was dissolved in DCM at a concentration of 10 mg/ml. 1 mg of Acr was dissolved in water at a concentration of 2.5 mg/ml. The two solutions were mixed and sonicated at an amplitude of 60% for 45 seconds to have small Acr in water droplets throughout the PLGA in DCM phase (water in oil emulsion). Subsequently, the mixture was poured in 4 ml of 3% PVA solution and was sonicated at an amplitude of 60% for 3 minutes to make nanoscale Acr-PLGA emulsions throughout the PVA phase (water in oil in water emulsion). The resulting NPs were transferred to a larger bath of PVA (50 ml) at a lower concentration (0.5%) and were stirred for 3 hrs so that the DCM evaporates and particles become hard. Afterwards, the NPs were washed three times with miliQ water.

5.2.3.3. Single emulsion method

To synthesize the NPs with single emulsion method, all the steps were similar to double emulsion method except instead of dissolving the Acr in water, it was dissolved in DMSO. Even though the DMSO and DCM are miscible, the polymer-drug solutions were sonicated to make sure they are mixed homogenously.

5.2.3.4. Single emulsion nanoprecipitation method

The following protocol is from Dr. Corey Bishop a former lab member of the Green lab.[15] Here, Dr. Bishop's protocol was modified, since it was for synthesizing PLGA NPs without PEGylation. For systemic delivery of NPs to target site, having a hydrophilic PEG shield around NPs enhances their half-life and effectiveness.[16] 4.7 mg Acr was dissolved in 1 ml methanol. This solution was added to a solution of 50 mg 502H PLGA and 50 mg PEG-PLGA that was dissolved in 4 ml of acetone. The resulting solution was vortexed and quickly poured in 17.0 ml of 10 mg/ml BSA solution that was being sonicated at an amplitude of 60% for 30 seconds. The resulting particles were stirred at 600 rpm in the cold condition ($4^{O}C$) overnight. Particles were stirred on ice for another 24 hrs under the vacuum. This was to ensure evaporation of the organic solvents. Subsequently, NPs were washed three times with miliQ water and were used right after synthesis. The particle leftovers were stored at the temperature of $-80^{o}C$ at a low concentration of 1 mg/ml. This way, particles could be stored for months and an aliquot could be thawed and concentrated (if required) for a subsequent use. Often during centrifugation, these NPs would aggregate, but the aggregates were separated by an additional centrifugation. The amount of particle loss by aggregate separation was taken into account by determining particle concentration afterwards.

5.2.4. Drug release characterization

Drug release from the NPs was studied by incubating the NPs in a small centrifuge tube at 37^{o}C in 1 ml PBS as the release media. At certain intervals, the NPs were centrifuged and certain amount of supernatant (900 ul for Dox NPs, and 800 ul for Acr NPs) was replaced with fresh PBS. The NP mass for drug release studies with Dox was 1.5 mg, while for Acr it was chosen to be 3.2 mg. Since Acr loading in NPs was less than that of Dox, more NPs were used for drug release studies to make sure signal from the release samples will be strong enough to have a reliable measurement. The release samples were lyophilized and reconstituted in DMSO and the fluorescence signal was read with a plate reader. All the release experiments were done in triplicate. The amount of drug detected was divided by the total detected drug release over the course of experiment to determine percent drug released.

5.2.5. Blood half-life and biodistribution determination

All of the animal preparations for biodistribution were done by Dr. Semenza's group at the Johns Hopkins University School of Medicine. MDA-MB-231 breast cancer cells were injected orthotopically in 10 mice (Type: SCID) and once the tumor size reached ~200 mm^3, the animals were treated with NPs. 5 mice were treated with Dox plus dye loaded NPs, while 5 mice received dye loaded NPs through tail vein injection. For both cases, the NP concentration was set to 50 mg/ml, in 1X PBS media. Blood was collected from the mice from the saphenous vein at 5, 10, 20, 40, 1 hr, 2hr and 24 hr timepoints and the fluorescence signal from the dye was analyzed by IVIS®. Each live animal was bled only 4 times during the course of the experiment. After 24 hrs, the animals were sacrificed, their organs were harvested and imaged with IVIS®. Images of the organs were used to determine NP biodistribution.

5.2.6. HIF assessment in cancer model *in vivo*

All of the animal preparations for functional HIF assessment were conducted by Dr. Semenza's group at the Johns Hopkins University School of Medicine. Hep3B-c1 cells were injected in the flank of 8 nude mice. Once tumor size reached approximately 100 mm^3, the treatment was started with NPs loaded with Dox or Acri. For Dox treatment group, animals received a single injection of NPs, while for Acr group animals received two injections of NPs on day 1 and 14. All the NPs had a concentration of 50 mg/ml in 1X PBS. The efficacy of NPs in inhibiting HIF expression was evaluated by measuring the luminescence from the tumor via IVIS® at certain timepoints post NP injection. The tumor cells were programmed by Dr. Semenza's group to have a HIF dependent reporter plasmid so that their luminescence was directly proportional to HIF activity.

5.2.7. *In vitro* cell studies on ocular cells

In vitro studies on ocular cells were performed by Dr. Sodhi's group at Johns Hopkins University School of Medicine. In brief, MIOM1 cells were treated with free drugs (Dox or Acr) or NPs loaded with drugs in hypoxia (1% oxygen level) at 1-5 μM drug concentrations. At certain time points, proteins were extracted from the cells and HIF expression was measured by gel electrophoresis.

5.2.8. In vivo studies for VEGF expression levels in the eye

In vivo studies were done in collaboration with Dr. Sodhi's group at Johns Hopkins University School of Medicine. 45 black mice (Type: C57bl/6) were treated through tail vein injection with free drug solutions, NP suspensions loaded with drugs. In addition, some of the animals received blank NPs or PBS as control. For Acr, two drug dosage was tested, 2.5 and 7.5 mg/Kg of body weight. While for Dox group, animals were treated with two drug dosages of 6 and 18 mg/Kg. For the case of NPs as well as high dosed free drugs, only one injection at day 0 occurred.

However, animals received free drugs at low dosages for 3 subsequent days. At certain timepoints (1, 3, and 7 days post treatment), the animals were sacrificed and Dr. Sodhi's group collected the eyes, and extracted mRNA from the retina. Subsequently, they quantified VEGF expression levels by qPCR technique.

5.2.9. Error analysis

Error bars presented in each figure represent standard deviation between replicate measurements.

5.3. Results

5.3.1. Nanoparticle characterization

5.3.1.1. Doxorubicin/dye loaded NPs

The goal was to administer the drug molecules intravenously. To make sure NPs won't lead to embolism in the small blood vessels of mice, NPs size should be small and stable. Small size (<200 nm) also lead to higher accumulation of the NPs in the tumors due to enhanced permeability and retention effect.[12] On the other hand, reduction in NP size could adversely impact the drug loading. Thus, the goal was to be able to synthesize drug loaded NPs with high drug loading and small particle size. Figure 5.1 shows the intensity-based particle size distribution for dox, Dox plus dye, and dye loaded NPs, synthesized in this research. In addition, intensity-based average NPs size (Z-average in brief), polydispersity index (PDI) and loading of NPs is illustrated in table 5.1.

(a) (c) (b)

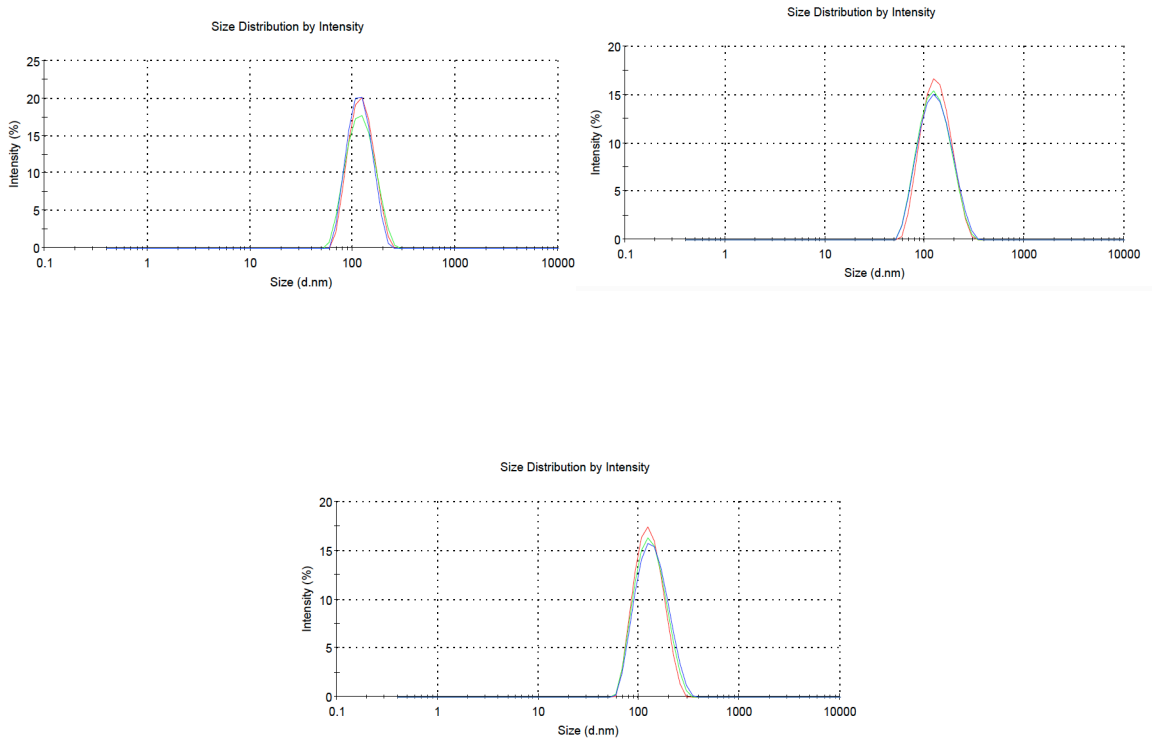

Fig. 5.1. Dox/dye loaded NPs size distribution, a) Dox loaded NPs, b) dye plus Dox loaded NPs, c) dye loaded NPs.

Table 5.1: Characteristics of dox, Dox plus dye and dye loaded NPs.

Parameter / NP type	Z-average (nm)	PDI	Dox loading (µg/mg NPs)
Dox loaded NPs	111	0.074	38
Dox plus dye loaded NPs	120	0.125	26
Dye loaded NPs	127	0.108	-

According to Fig. 5.1 and Table 5.1, all the NPs synthesized had narrow size distribution and small PDI. In addition, Z-average for all the NPs was below 200 nm which is acceptable for intravenous drug delivery. Table 5.1 also demonstrates that Dox loaded NPs had a drug loading of around 38 μg/mg of NPs which is acceptable (i.e. >10 μg/mg of NPs). An important contributor to enhancement of Dox loading was deprotonation of Dox in the presence of TEA[17] (This method of loading enhancement by removal of HCl salt was discussed in Chapter 4 as well to synthesize levobunolol loaded MPs). By removing the HCl salt from Dox in the presence of TEA, it becomes more hydrophobic, thereby its tendency to be encapsulated in hydrophobic PLGA increases. There was more than 4x enhancement in Dox loading by deprotonation. Finally, Table 1 indicates that Dox loading decreases by co-encapsulation of Dox and dye in NPs.

5.3.1.2. Acriflavine loaded nanoparticles:

As mentioned before, Acr is a hydrophilic drug molecule and thus had low encapsulation efficiency in hydrophobic PLGA NPs. As a result, several techniques were evaluated to see their impact on NPs' characteristics. Figure 5.2 compares the size distribution of Acr loaded NPs synthesized with different methods obtained by dynamic light scattering (DLS) technique. Further, Table 5.2 highlights characteristics of these NPs.

(a) (e) (b)

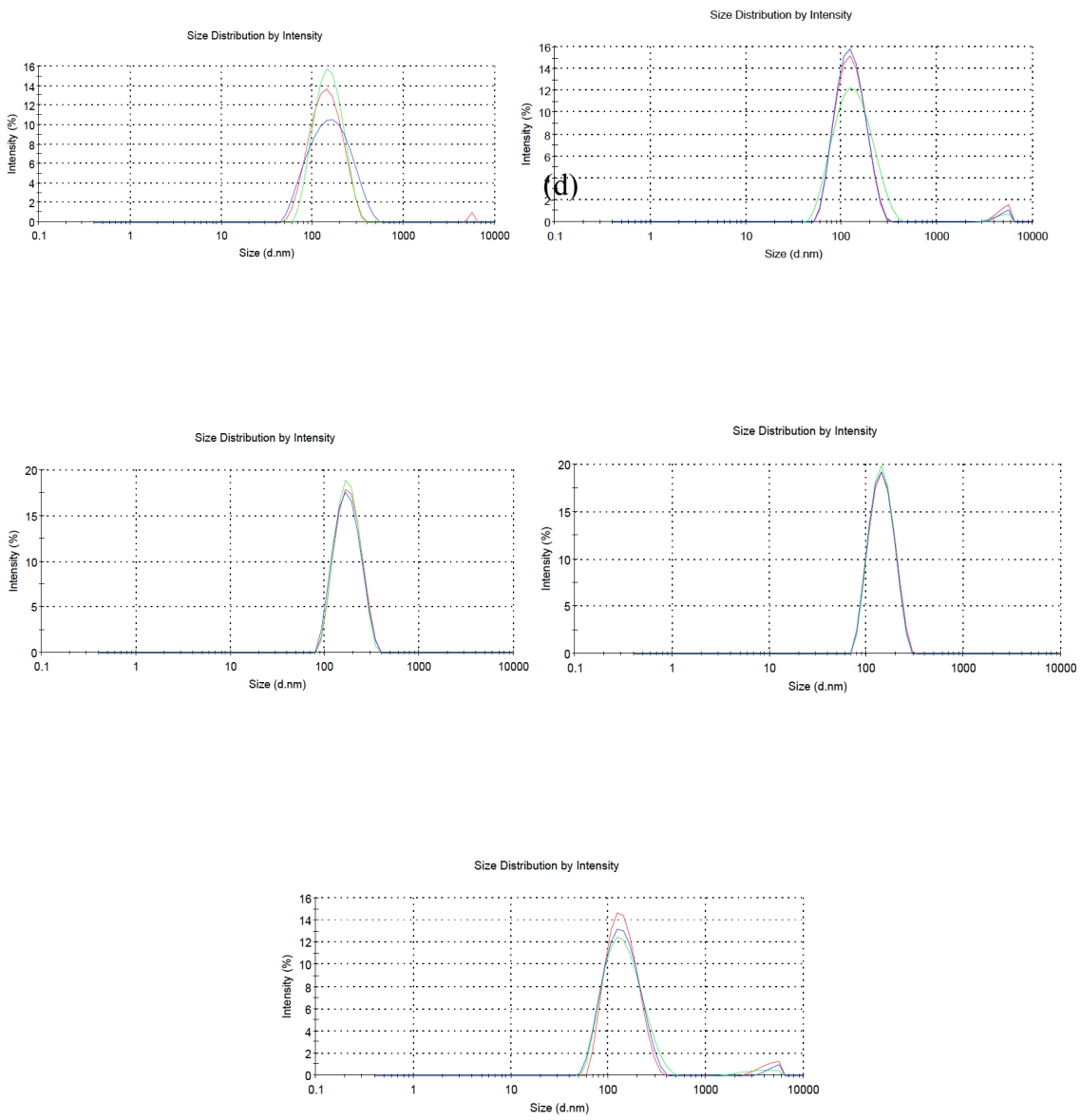

Fig. 5.2. Z-average for Acr loaded NPs synthesized with a) nanoprecipitation (Acr.HCl), b) nanoprecipitation, c) double emulsion, d) single emulsion, e) single emulsion nanoprecipitation. Plots b-e are for NPs loaded with Acr.

Table 5.2: Z-average, PDI and Acr loading for NPs synthesized with different schemes.

Parameter / NP type	Z-average (nm)	PDI	Acr loading (μg/mg polymer)
Acr.HCl, nanoprecipitation	141	0.224	0.4
Acr, nanoprecipitation	123	0.192	2.4
Double emulsion	163	0.080	2.1
Single emulsion	137	0.063	1.1
Single emulsion nanoprecipitation	131	0.205	15

Different Acr loaded NPs had a relatively narrow size distribution shown in Fig. 5.2 and small PDI demonstrated in Table 5.2. NPs synthesized with single/double emulsion methods had particularly low PDI indices. The smaller peaks shown in Fig. 5.2a,b, and e for more than 1000 nm size range is likely due to presence of dust in DLS cuvette. Table 5.3 also demonstrates that NPs had relatively small z-average, regardless of the method used to synthesize the NPs. However, the main challenge with Acr was to increase its loading in NPs. By switching from Acr.HCl to Acr without hydrochloride salt, the loading was enhanced significantly in nanoprecipitation method. However, the overall Acr loading was far below our target. For cancer and ocular diseases, a dosage of at least 100 μg Acr per injection in mice was required. Assuming that injection happens at a concentration of 50 mg/ml, and 200 μl NPs are injected, the loading of Acr in NPs should be at least 10 μg/mg of NPs. The effect of organic solvent used in nanprecipitation method was studied by switching from DMSO to DMF. Even though it increased Acr loading to 3.3 μg/mg of NPs, the loading was still below the target value.

For hydrophilic drug molecules, double emulsion method is particularly suitable, since the hydrophilic drug molecule is already in aqueous phase during NP synthesis, so its tendency to escape during NP formation would decrease. However, neither single nor double emulsion methods led to NPs with acceptable drug loading. The effect of polymer concentration in DCM, PVA volume and concentration were studied to probe their impact on Acr loading. However, it did not lead to a significant increase in Acr loading.

Among the different methods tested, the single-emulsion nanoprecipitation method was the only method leading to NPs with adequate drug loading, yet small enough NP size and it was therefore chosen as the method of choice to test HIF expression inhibition in the subsequent experiments.

5.3.2. Drug release characterization

Dox loaded NPs were chosen to determine the blood half-life of NPs. In this regard, dye was co-loaded with Dox to track the NPs *in vivo*. It is important to study the release kinetics of Dox plus dye from NPs and also compare it with Dox loaded NPs alone. In this regard, Fig. 5.3 compares the drug release kinetics from the two NP systems.

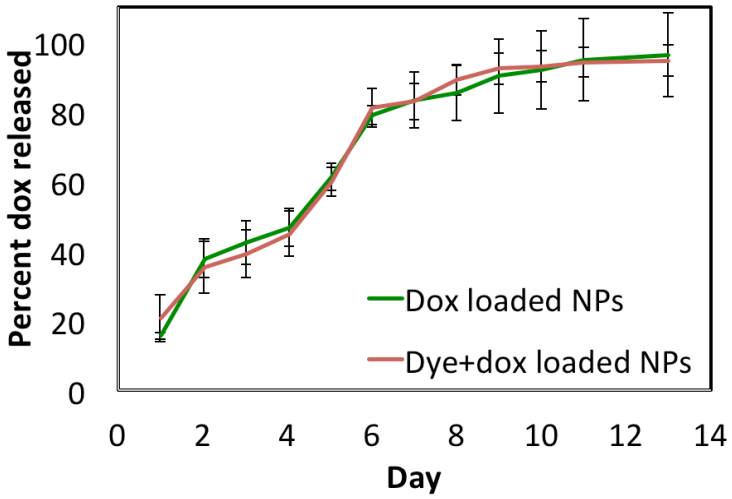

Fig. 5.3. Percent released Dox from Dox loaded NPs compared with Dox plus dye loaded NPs.

As can be seen in Fig. 5.3, Dox loaded NPs had similar Dox release kinetics compared to Dox plus dye loaded NPs. Also, this figure shows that it takes around two weeks for the NPs to release dox, with 20% burst release on day 1. Figure 5.4 depicts percent released Acr from NPs synthesized with single emulsion nanoprecipitation technique.

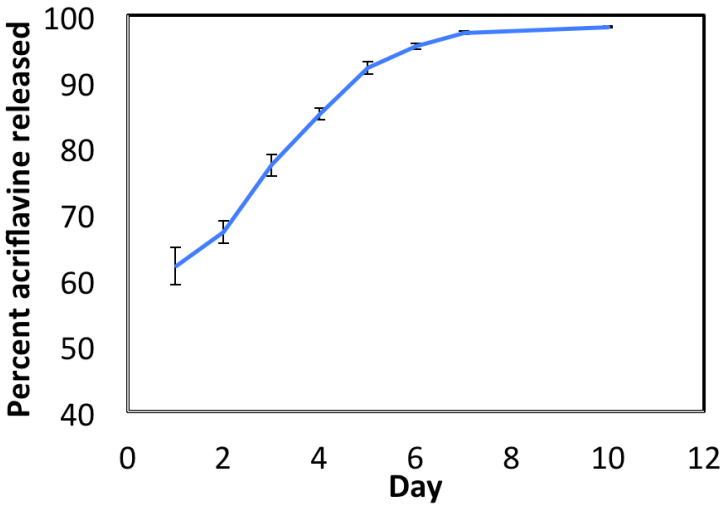

Fig. 5.4. Release kinetics of Acr from NPs, *in vitro*.

Unlike dox, Acr is released from the NPs in about a week. Furthermore, around 60% of the Acr is released from the NPs in 24 hrs post incubation at 37 ^{o}C. Considering the higher hydrophilicity of Acr compared to Dox, the trend observed is understandable. Due to its hydrophilicity, Acr does not have the tendency to be loaded in hydrophobic core of PLGA NPs, so part of loaded Acr is presumably attached to NPs surface where hydrophilic PEG part is present. This together with high tendency of Acr to diffuse into aqueous media enabled a high burst release of Acr from NPs.

5.3.3. HIF inhibition in the cancer model

5.3.3.1. Nanoparticles half-life in the blood stream and biodistribution

Figure 5.5 shows the logarithm of blood fluorescence signal normalized to blood signal at 5 minutes timepoint vs. time post NP injection for the two treatment groups of Dox plus dye loaded

NPs and dye loaded NPs. The goal for comparing these two groups was to see if the Dox loading will have any impact on blood half-life and biodistribution. Dye plus Dox loaded NPs had max Dox loading, while dye loaded NPs had no Dox. By comparing these two groups, the two ends of the spectrum (zero to max Dox loading) are compared.

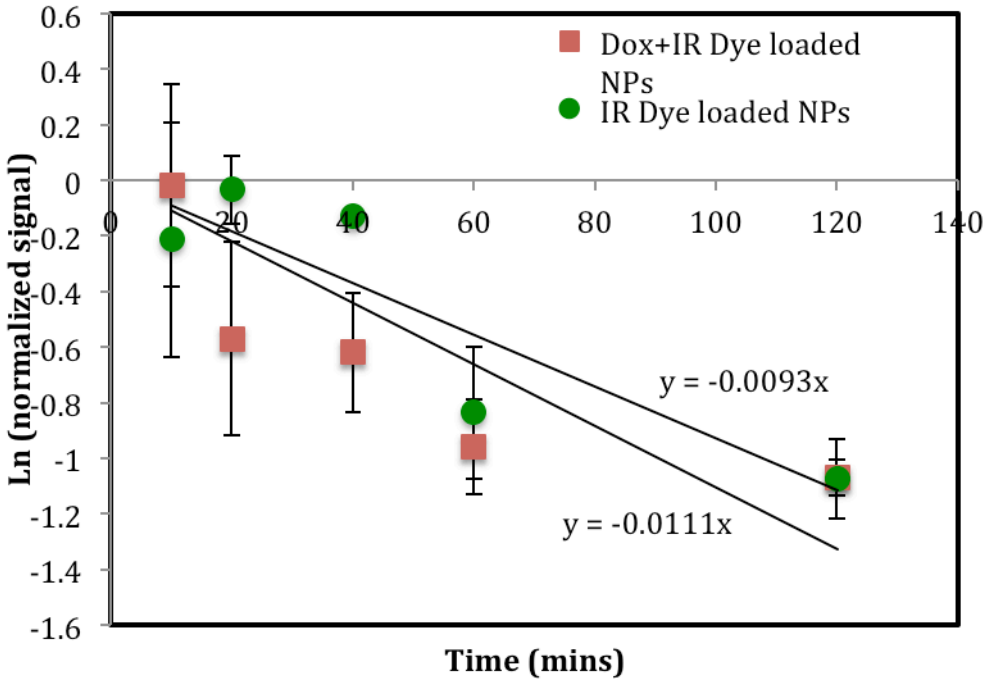

Fig. 5.5. Blood half-life for the dye loaded NPs compared to the Dox plus dye loaded NPs in mice bearing breast tumor.

The general trend observable in Fig. 5.3 (with an exception) is the decrease in the blood fluorescence intensity over time. NPs are gradually cleared from the blood stream and accumulated in different organs in the body. One should note the caveat that we are relying on the fluorescence intensity to determine blood half-life and biodistribution of NPs. This method relies on fluorescence intensity of the dye that is encapsulated in the NPs to track the NPs. Since the dye is very hydrophobic, it assumes that release of the dye from NPs is negligible. Before using the fluorescence dye, extensive experiments were performed extracting the Dox itself from organs and the blood. However, since Dox's fluorescence is in the red channel, and the body has

plenty of auto-fluorescence in this channel, it proved to be impossible to get reliable data by relying on Dox's intrinsic fluorescence.

By fitting a linear line to the results presented in Fig. 5.3 and following Eq. (5.1), blood half-life for the NPs was determined.

$$F(t) = F_0 \exp(-\frac{t}{\tau}) \tag{5.33}$$

Where F(t) is the dye fluorescence intensity in the blood at a given time, F_0 is the maximum dye fluorescence intensity after 5 mins of NP injection (to make sure NPs are circulated in the entire blood stream and there will be maximum blood fluorescence intensity), and τ is the NP half life in the blood stream. The half-life for the Dox+Dye treatment group turned out to be 62 minutes, while for the IR dye loaded particles only, it was 75 minutes. The difference between blood half-life of the two NP treatment groups is small considering the deviation between data points in Fig. 5.5 due to experimental error. Experimental errors in blood half-life could be difficulty in collecting enough blood from the animal and at required timepoint. Also, the accuracy of data could significantly increase by increasing the number of animals dedicated for the experiment.

Figure 5.6 depicts the biodistribution of the NPs in different organs of the mice. In this figure, fluorescence signal is normalized by the total fluorescence of organs of interest in each animal. Afterwards, the signal from each organ is averaged between animals of the specific treatment plan.

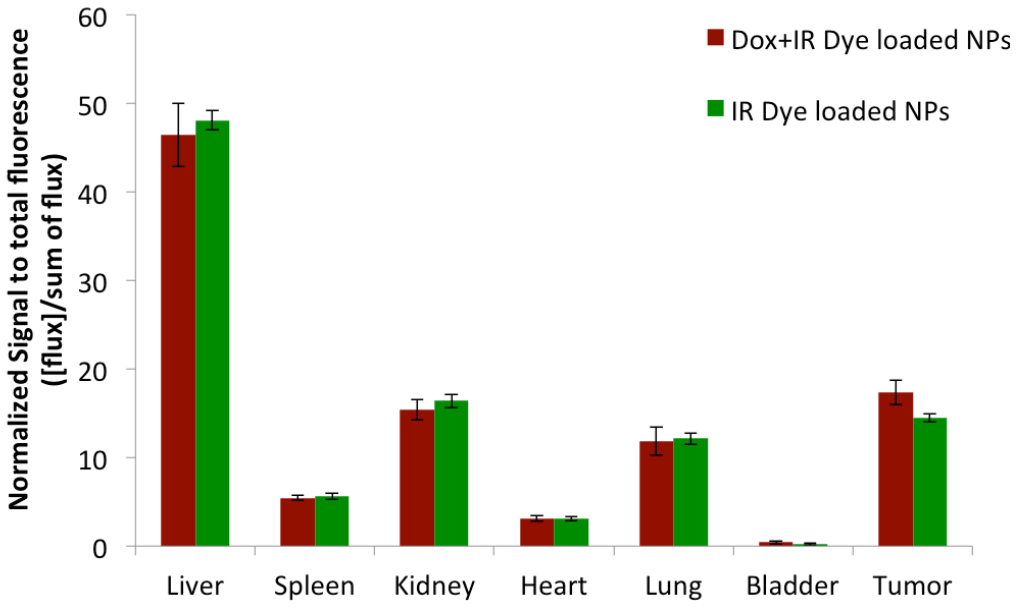

Fig. 5.6. Biodistribution of the NPs in different organs.

According to Fig. 5.6, the two treatment groups had similar biodistribution. The liver had the highest NP accumulation (~45%), which is expected considering its large size compared to other body organs. Tumor had around 15% NP accumulation. Accumulation of NPs in the tumor is very high which is favorable to enhance treatment efficacy. Small size of NPs and presence of a PEG shield around the NPs have enabled high NP accumulation in the tumor.

5.3.3.2. HIF inhibition *in vivo* in a cancer model

Figure 5.7 illustrates the variation of luminescence flux (HIF level) vs. days post NP injection.

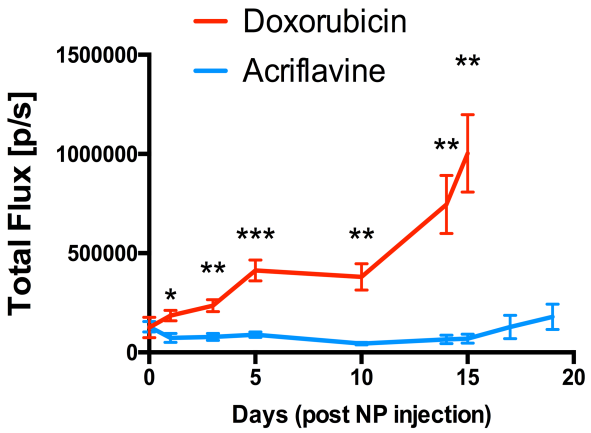

Fig. 5.7. *In vivo* efficacy of NPs on inhibiting HIF in cancer model. Imaging of animals and analysis of the results were done by Dr. Debangshu Samanta and David Wilson.

According to Fig. 5.7, for the case of Dox loaded NPs, HIF levels increases over time, and NPs were unable to inhibit HIF. On the other hand, Acr NPs were able to maintain the HIF levels for two weeks post NP injection. As a result, the Acr NP group was chosen as the treatment of choice to perform future studies.

5.3.4. Ocular drug delivery

The goal of this part of the project was to evaluate the effectiveness of Dox and Acr loaded NPs on treatment of diabetic retinopathy. This part of the project was performed in collaboration with Dr. Sodhi's group at Johns Hopkins University School of Medicine. Diabetic retinopathy is a serious ocular disorder with excessive formation of blood vessels in the back of the eye which could obstruct the patients' vision. Our collaborator had shown the effectiveness of the anti-HIF agents (e.g. Dox and Acr) on the inhibition of HIF and reduction of angiogenesis. However, free drug molecules had to be dosed daily and at a high concentration to ensure effectiveness, which were unfavorable for the translation of the idea into the clinic. NPs could release the drug molecules for at least a week, and could potentially prolong the effectiveness of treatment.

5.3.4.1. HIF inhibition *in vitro*

Figure 5.8 compares the effectiveness of drug encapsulated NPs with free drugs in preventing HIF expression, *in vitro*.

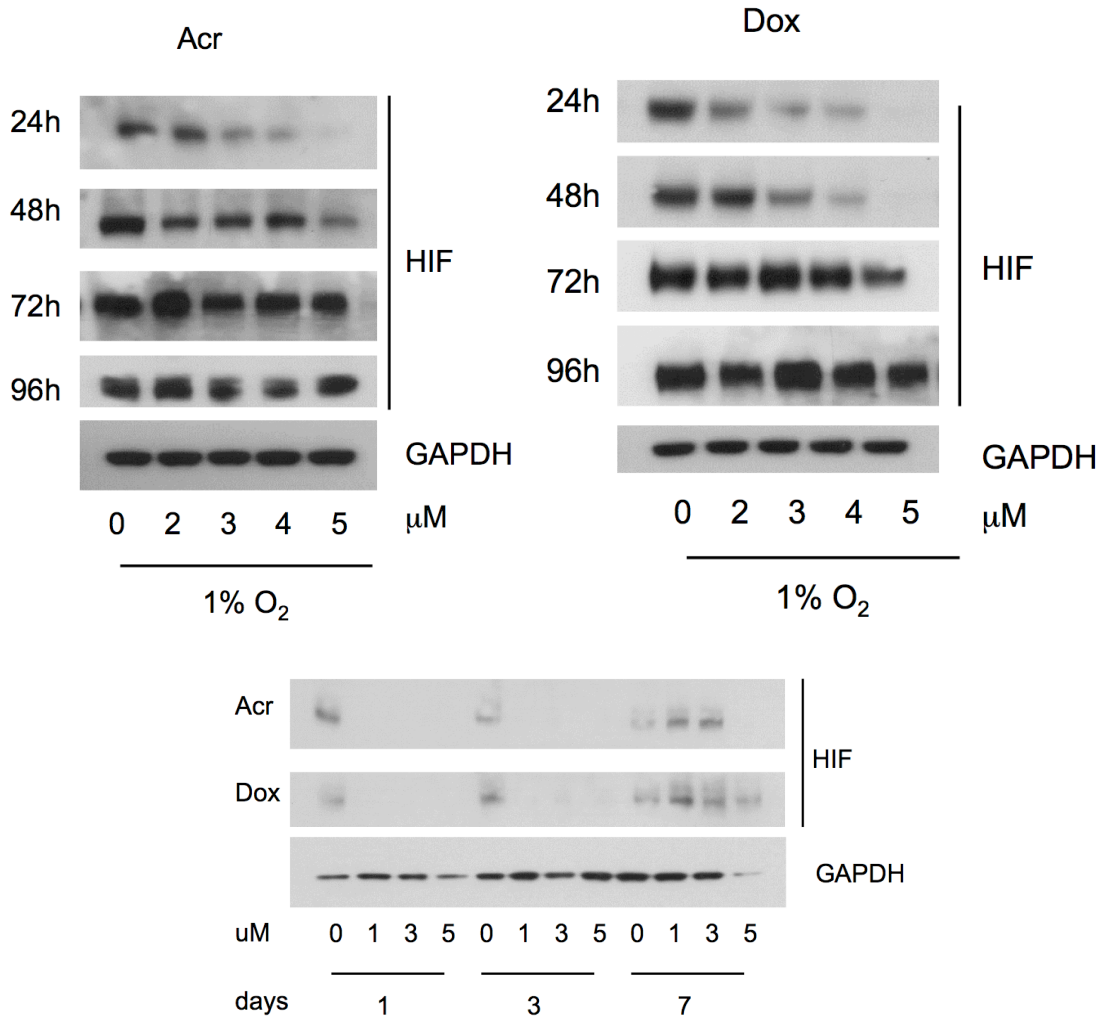

Fig. 5.8. HIF expression levels for free a) Acr and b) Dox compared with c) those drugs loaded in NPs, *in vitro*. At each condition, black band is indicative of HIF presence. Experiments were performed by Dr. Sodhi's group.

Figure 5.8 illustrates that free drug molecules can only prevent HIF expression at high concentrations of 5 μM. In addition, free drugs are limited in duration of action. For Dox, HIF expression was inhibited for up to 48 hrs, while Acr was effective for only 24 hrs. On the other

hand, NPs have been effective in inhibiting HIF expression at even 1 μM drug concentration. In addition, they have extended drug duration of action to at least three days. Overall, NPs showed great promise in preventing HIF expression *in vitro*.

5.3.4.2. Angiogenesis inhibition *in vivo*

To assess the effectiveness of NPs *in vivo*, it is important to track mRNA levels of VEGF, as it is related to formation of abnormal formation of blood vessels in diabetic retinopathy. Figures 5.9-5.11 show the variation of VEGF levels for after 1, 3, and 7 days post-treatment with NPs, respectively.

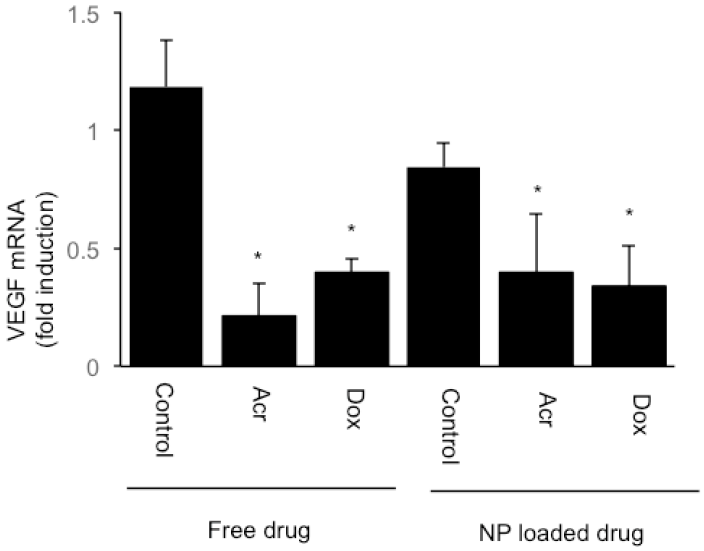

Fig. 5.9. Effect of free drug compared with drug loaded NPs on VEGF levels after 1 day post-treatment, *in vivo*. Determination of VEGF level was done by Dr. Sodhi's group.

(b)

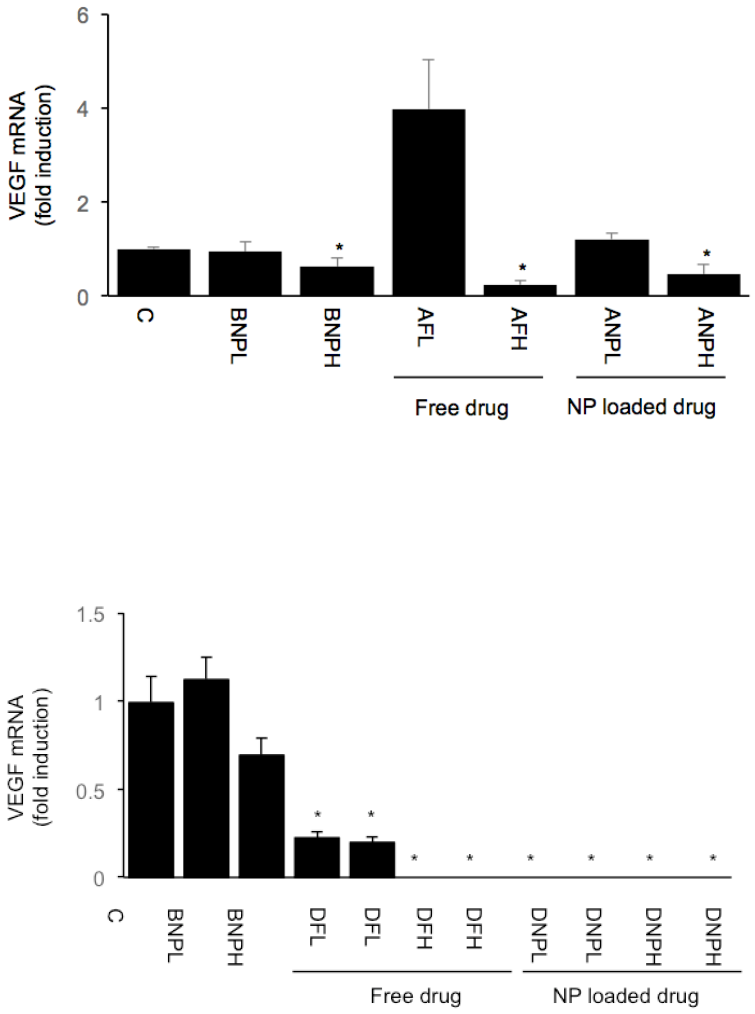

Fig. 5.10. Effect of NPs on reduction of VEGF compared with free drug after 3 days post NP injection. a) Acr, b) Dox. In this and subsequent figure, control represents the animals that received PBS injection. BNPL and BNPH refer to animals that received blank NPs at a low and high concentrations, respectively. AFL and AFH represent animals that received free Acr at a dose of 2.5 and 7.5 mg/Kg, respectively, while DFL and DFH refer to animals that received free dox at dosages of 6 and 18 mg/Kg, respectively. ANPL, ANPH, DNPL and DNPH represent animals that received the same dosages of Acr or Dox mentioned before but in the NP form. VEGF level was determined by Dr. Sodhi's group.

(a)

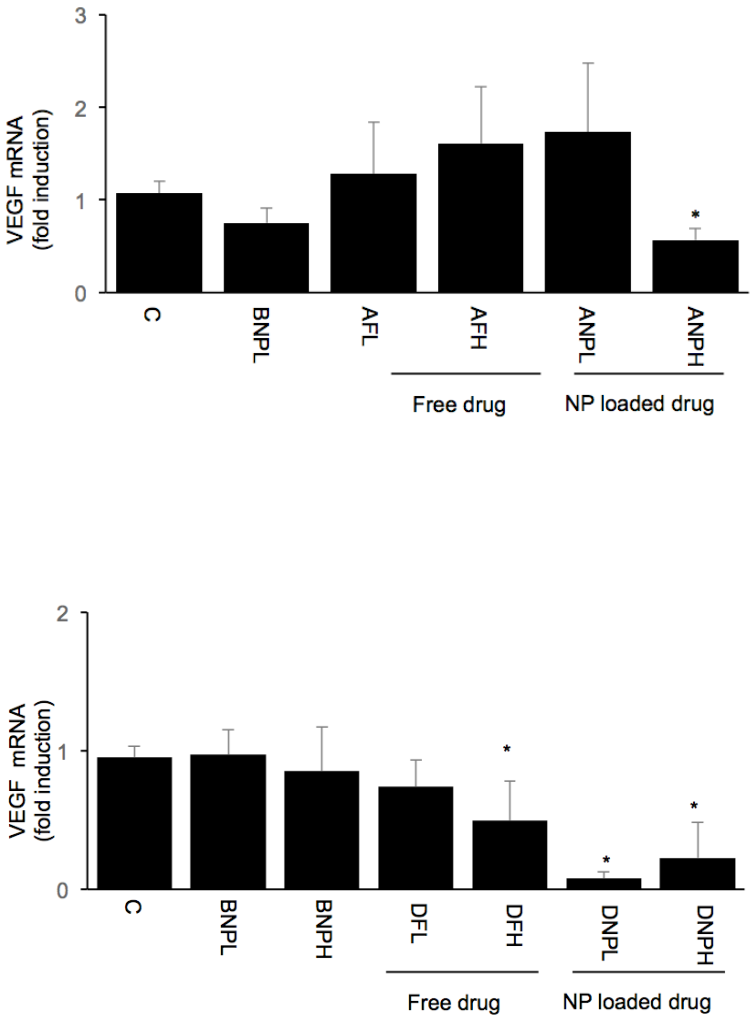

Fig. 5.11. VEGF levels in retina 7 days after treating the mice with free drug or drug loaded NPs. a) Acr, b) dox. VEGF level was assessed by Dr. Sodhi's group.

On day 1, both Acr and Dox (free or loaded in NPs) have been able to reduce the VEGF expression. On day 3, Acr NPs or free Acr are only effective at high dose (7.5 mg/Kg), while Dox (free or NP form) has been effective in reducing VEGF levels. It is remarkable how free Dox at high dose or NPs at either dosage have been able to completely block VEGF expression on day 3. On day 7, free Acr is no longer effective on reducing VEGF, while Acr loaded NPs are able to reduce VEGF at high dosage. In addition, free Dox is only able to reduce the VEGF at high

dosage, while Dox loaded NPs at either dosage have decreased VEGF expression. Overall, these results demonstrate that drug-loaded NPs are more effective than free drug in reducing VEGF expression. In addition, unlike cancer model, Dox seems to be more advantageous than Acr. Considering the fact that for 3 days and 7 days studies, low dose free drug was injected for three subsequent days, while animals received NPs only for day 0, it is clear that NPs have been effective in reducing treatment frequency.

5.4. Conclusions

This chapter highlighted preliminary results on using anti-HIF loaded NPs for the treatment of cancer and ocular diseases. The followings are the main conclusions of this ongoing study:

1. PEGylated nanoparticles loaded with Acr or Dox were synthesized with small size (below 200 nm) and high drug loading (>10 μg/mg of NPs).
2. Dox loaded NPs showed a half-life of around an hour and a high tumor accumulation of 15% in the mouse with cancer model.
3. Acr loaded NPs enabled inhibition of HIF expression for two weeks post NP injection in the cancer model, while Dox loaded NPs were not as effective in reducing HIF levels.
4. In general, NPs showed longer lasting effectiveness on reducing VEGF expression compared to free drug. Also, in the ocular model, Dox loaded NPs were more effective compared to Acr loaded NPs.

5.5. Acknowledgements

I would like to thank Jayoung Kim, David Wilson and Kisha Patel from Dr. Green's lab for their help with the synthesis of NPs and performing the in vivo experiments. I appreciate Dr. Debangshu Samanta and Dr. Gregg Semenza for their contributions to the cancer project. I am very grateful to Dr. Monika Deshpande, and Dr. Akrit Sodhi for their valuable contributions and

insight regarding the ocular drug delivery project. I would also like to thank Dr. Corey Bishop and James Shamul for their well-informed discussions on nanoparticle formulation. I am very grateful to Howard Hughes Medical Institute for the International Student Research fellowship.

5.6. References

1 Semenza, G. L. Hypoxia-inducible factors: mediators of cancer progression and targets for cancer therapy. *Trends in pharmacological sciences* **33.4**, 207-214 (2012).

2 Lee, K., Zhang, H., Qian, D. Z., Rey, S., Liu, J. O., & Semenza, G. L. Acriflavine inhibits HIF-1 dimerization, tumor growth, and vascularization. *Proceedings of the National Academy of Sciences* **106**, 17910-17915 (2009).

3 Sodhi, A., & Montaner, S. Angiopoietin-like 4 as an emerging therapeutic target for diabetic eye disease. *JAMA ophthalmology* **133**, 1375-1376. (2015).

4 Paulus, Y. M. & Sodhi, A. in *Pharmacologic Therapy of Ocular Disease* (eds Scott M. Whitcup & Dimitri T. Azar) 271-307 (Springer International Publishing, 2017).

5 Iwase, T. *et al.* Sustained delivery of a HIF-1 antagonist for ocular neovascularization. *Journal of controlled release* **172**, 625-633 (2013).

6 Semenza, G. L. The hypoxic tumor microenvironment: A driving force for breast cancer progression. *Biochimica et Biophysica Acta (BBA)-Molecular Cell Research* **1863**, 382-391 (2016).

7 Gilkes, D. M., Semenza, G. L. & Wirtz, D. Hypoxia and the extracellular matrix: drivers of tumour metastasis. *Nature Reviews Cancer* **14**, 430-439 (2014).

8 Subhani, S., Vavilala, D. T. & Mukherji, M. HIF inhibitors for ischemic retinopathies and cancers: options beyond anti-VEGF therapies. *Angiogenesis* **19**, 257-273 (2016).

9 Liang, D., Kong, X. & Sang, N. Effects of histone deacetylase inhibitors on HIF-1. *Cell Cycle* **5**, 2430-2435 (2006).

10 Ziff, O. J. & Kotecha, D. Digoxin: The good and the bad. *Trends in Cardiovascular Medicine* **26**, 585-595 (2016).

11 Manivannan, C., Meenakshi Sundaram, K., Sundararaman, M. & Renganathan, R. Investigation on the inclusion and toxicity of acriflavine with cyclodextrins: A spectroscopic approach. *Spectrochimica Acta Part A: Molecular and Biomolecular Spectroscopy* **122**, 164-170 (2014).

12 Waite, C. L. & Roth, C. M. Nanoscale drug delivery systems for enhanced drug penetration into solid tumors: current progress and opportunities. *Critical Reviews™ in Biomedical Engineering* **40** (2012).

13 Tewes, F. *et al.* Comparative study of doxorubicin-loaded poly (lactide-co-glycolide) nanoparticles prepared by single and double emulsion methods. *European Journal of Pharmaceutics and Biopharmaceutics* **66**, 488-492 (2007).

14 http://www.sigmaaldrich.com/catalog/product/sigma/a8126?lang=en&region=US.

15 Bishop, C. *Nanoparticles for anti-HIF efficacy, Unpublished work.*

16 Li, Z. *et al.* Recent progress in application of PEGylated nanocarriers for antitumor drug delivery systems. *Drugs of The Future* **41**, 177-184 (2016).

17 Shamul, J. *Deprotonation of Doxorubicin hydrochloride, Unpublished work.*

Chapter 6

Conclusions and Future Directions

6.1. Binding kinetics of particles under flow

In chapter 2 binding kinetics of spheres under shear flow in the dilute sphere limit was studied implementing BD simulations. The results presented were from the first theoretical model developed in Larson Group capable of determining the binding kinetics of two spheres for the whole Pe range and with hydrodynamic interactions. In addition, agreement with various limits obtained by literature was achieved. Furthermore, binding times were computed with either implementing an interparticle potential or by choosing a cut off distance. A major advantage of the technique presented was its ability to analyze particles with surface anisotropy.

The successful implementation of a BD simulation method to particles under flow opens the door to many further opportunities. A handful of them are as follows:

1) The method introduced here is not limited to shear flows and could hopefully be applied to other types of flows as well, such as extensional flow, mixed shear, and extensional flows, etc. To this end, proper development and application of boundary conditions, and periodic box dimensions that allow imposition of these boundary conditions are essential.[1]
2) Investigation of binding kinetics of more complex patterned colloids, such as patchy particles[2] with multiple patches under shear flow is another area of interest. Lock and key colloids,[3] could also be studied if the deviations from spherical shape could be accounted for, perhaps in some approximate way. Other shapes could be considered using

hydrodynamic functions developed by Kim and Karrila[4] for particles without spherical symmetry.

3) The binding kinetics of non-dilute denser suspensions under shear flow could be implemented using the methods of Stokesian dynamics[5] to handle multi-particle interactions.

6.2. Layer-by-layer assembly of polyelectrolytes and nanopartilces

In chapter 3, different parameters impacting layer-by-layer growth of polyelectrolytes (PEs) and nanoparticles (NPs) including polyelectrolyte molecular weight (MW), NP size and charge, as well as pH and salinity of the deposition media were examined. Obtained results indicated the importance of polyelectrolyte layer in between NP deposition steps to enhance the integrity of LbL films. In general, intermediate values of PE MW led to rapid LbL film growth in most of the cases. It was due to a competition between high layer integrity and bridging between two subsequent NP deposition steps for larger chain PEs and high diffusivity for smaller PE chains.

When the polyethylenimine (PEI) was deposited at a higher pH of 9.9 (lower charge) followed by NP deposition at a lower pH of 7, highest film growth occurred. It was due to sudden enhancement in PEI charge during deposition of NPs and its desire to absorb more NPs to compensate for charge increase. In addition, a relation between salinity and MW of PEs on LbL film growth was demonstrated.

Some of these trends, especially the effects of pH and PE molecular weight, and to some extent the effect of salinity, can be understood qualitatively. But even the general trends observed were defied for some particle sizes, depending on the particular PE. Even when the expected trend was followed, for example the non-monotonic dependence of growth rate on PE molecular weight, the value of the optimal molecular weight varied greatly (more than an order of magnitude) from PEI to poly(acrylic acid) (PAA), for no reason we could determine. Hence, while some qualitative

trends are now evident and explicable, even semi-quantitative predictions are not yet in sight, and there are polymer-specific exceptions to even the qualitative trends.

Clearly, much progress is still needed to develop an improved qualitative and quantitative understanding of LbL deposition of PEs and NPs. In addition to further systematic LbL growth experiments such as those performed here, more detailed microscope experiments could be very helpful, such as atomic force microscopy (AFM) studies of binding and adhesion forces between individual NPs and PEs, direct measurements of PE and NP diffusion in the film, fluorescence resonance energy transfer (FRET) measurements of binding and unbinding events, and other direct measurements of molecular structures and transitions. Finally, using fluorescently labeled PEs and monitoring their diffusion within the film network could provide significant insights on the physics behind different phenomena observed.

6.3. Multidrug carrier for the postoperative management of ocular surgery

In chapter 4, a multidrug delivery system was developed for the postoperative treatment of ocular surgery (cataract surgery in particular). The formulation was made up of temperature sensitive A-B-A triblock copolymer solutions, where A block could be poly(D,L-lactide-co-glycolide) (PLGA), Poly(lactic acid) (PLA) or Poly(lactide-co-caprolactone) (PLCL), while the B block was poly(ethylene glycol) (PEG). In the optimal formulation, these polymer solutions were liquid at room temperature and formed a hydrogel depot at body temperatures. An antibiotic (moxifloxacin) was directly added to the co-polymer solution and was "loosely" entrapped in the hydrogel network once the temperature was raised to the body temperature. This enabled rapid release of moxifloxacin for about a week. However, a steroid (dexamethasone) and an ocular hypotensive drug molecule (levobunolol) were encapsulated in the microparticles (MPs) first and then loaded in the hydrogel network. Encapsulating the drug molecules in MPs considerably enhanced the duration of release of drug molecules to several weeks. Deprotonation of

levobunolol hydrochloride dramatically enhanced its loading in MPs. Due to their rapid degradation and creation of a local acidic environment, PLGA-PEG-PLGA accelerated the release of drug molecules entrapped in MPs. On the other hand, PLCL-PEG-PLCL hydrogels illustrated slow drug release. Finally, it was demonstrated that by changing the hydrophobicity of the polymer encapsulating the levobunolol, its drug release profile could be fine-tuned.

The results presented in this chapter were preliminary demonstration of the suitability of thermoresponsive hydrogels as ocular drug carriers. However, the following points should be addressed in the future:

1) Illustration of proper gelation of formulation, *in vivo*. The resulting hydrogel should not block the visual axis or interfere with the vision.
2) Demonstration of the ability of the formulation to prevent infection, inflammation and management of intraocular pressure, *in vivo.*

Even though the multidrug delivery formulation developed in this chapter was designed as a drug carrier to manage postoperative treatment following ocular surgery, it could be applied to co-deliver different types of drug molecules for other ocular indications as well. A direct application could be reformulating the hydrogel to release anti-hypoxia inducible factors (anti-HIF) for several weeks to be used for the treatment of diabetic retinopathy that was described in chapter 5.

6.4. Inhibiting HIF expression for drug delivery for cancer or ocular diseases

In chapter 5 preliminary results on using NPs to sustain the inhibition of HIF expression was discussed for cancer and ocular drug delivery. By deprotonation of doxorubicin (Dox), its loading in NPs was enhanced significantly. Several NP synthesis protocols were examined to synthesize acriflavine (Acr) loaded NPs with small size (<200 nm) and adequate drug loading (>10 μg/mg of NPs). It turned out that single emulsion nanoprecipitation method is the best method for synthesis of Acr loaded NPs.

The blood half-life and biodistribution in the cancer model was studied with Dox loaded NPs. NPs had a half-life of about an hour and demonstrated 15% tumor accumulation. In the cancer model, even though Dox loaded NPs were not effective in inhibition of HIF expression, Acr loaded NPs maintained HIF levels low for two weeks. Finally, unlike free drug, NPs had a much longer effect on reducing the angiogenesis in the eye. Also, Dox was superior than Acr for the eye model.

It should be noted that the preliminary studies for eye models were performed on healthy animals. Evaluation of NPs impact on reduction of angiogenesis in animals with diabetic retinopathy is the next step in this study. Given NPs were very effective in reducing the VEGF levels in healthy animals (which were already low), it would be interesting to see the impact of NPs on reducing angiogenesis and VEGF levels on mice with diabetic retinopathy.

In addition, systemic delivery of NPs for the treatment of ocular diseases may not be the best approach. Since eyes have a much smaller volume compared to other body organs, the portion of NPs that will end up to the eye is low. It may be best to deliver NPs directly to the eye through intravitreal injection. However, NPs could scatter throughout the eye surface and potentially cause "snow-globe" effect. Furthermore, as mentioned in chapter 4, due to their small size NPs are not effective in releasing the drug molecules for the long term (at least a month). Utilizing the technology developed in this thesis (Chapter 4) would be the best solution to sustain the release of anti-HIF molecules for the long term as well as finely tune their daily dosage.

On the other hand, for the case of cancer treatment, using NPs is a more suitable strategy. Since the best approach to deliver anti-HIF agents to leaky tumor vasculatures is through their systemic delivery. Our preliminary results indicated significant HIF inhibition for the case of Acr loaded NPs. For cancer and eye diseases, combination of anti-HIF agents might be much more effective, since they could have some synergistic effects and could reduce the overall drug dosage and inherent side effects.

6.5. References

1 Kraynik, A. M. & Reinelt, D. A. Extensional motions of spatially periodic lattices. *International Journal of Multiphase Flow* **18**, 1045-1059 (1992).

2 Shah, A. A., Schultz, B., Kohlstedt, K. L., Glotzer, S. C. & Solomon, M. J. Synthesis, assembly, and image analysis of spheroidal patchy particles. *Langmuir* **29**, 4688-4696 (2013).

3 Sacanna, S., Irvine, W. T. M., Chaikin, P. M. & Pine, D. J. Lock and key colloids. *Nature* **464**, 575-578 (2010).

4 Kim, S. & Karrila, S. J. *Microhydrodynamics: principles and selected applications*. (Butterworth-Heinemann Publications, 1991).

5 Brady, J. F. & Bossis, G. Stokesian dynamics. *Annual review of fluid mechanics* **20**, 111-157 (1988).

Appendices

Appendix A: Supplementary Information for Chapter 2

A.1. Brownian Dynamics method

When the suspension is dilute enough, two-body interactions dominate. Periodic boundary conditions are implemented with box dimensions chosen to approach the dilute limit and minimize artificial effects of the box geometry on binding kinetics.

The Langevin equation governing the particles' motion under shear flow is given by

$$r(t+\delta t) = r(t) + k_B T(\nabla \cdot M(\mathrm{t}))\delta t + \mu^{-1} M(t)[F^C(\mathrm{t}) + F^B(\mathrm{t})]\delta t + (N:E)\delta t + v^S(t)\delta t \qquad \text{(A1)}$$

where r can represent the positions as well as angles of both particles (12 degrees of freedom), k_B is the Boltzmann constant, T is temperature, M is the mobility matrix (inverse of resistance matrix described previously[1]), δt is the timestep for numerical integration, F^C denotes the conservative force, F^B is Brownian force, and v^S represents imposed shear velocity. Also, elements of N are obtained from g and h third-rank tensors reported by Jefferey[2] and E is rate of strain tensor for shear flow.

To prevent doing the expensive calculations to obtain the divergence of the mobility matrix, a midpoint algorithm for the absence of shear flow has been suggested which implicitly applies the effect of this term.[3,4] This algorithm has been modified as shown in Eq. (B2-a) to account for the effect of shear flow:

$$r(t^*) = r(t) + \mu^{-1} M(\mathrm{t})[F^C(\mathrm{t}) + F^B(\mathrm{t})]\frac{\delta t}{2} \qquad \text{(A2-a)}$$

$$r(t+\delta t) = r(\mathrm{t}) + \mu^{-1} M(\mathrm{t}^*)[F^C(\mathrm{t}) + F^B(\mathrm{t})]\delta t + (N:E)\delta t + v^s(t)\delta t \qquad \text{(A2-b)}$$

Here t^* is the mid-point of a timestep that spans the interval [t , $t+\delta t$]. (Inclusion of the shear flow terms in Eq. (A2-a) was also tested, and the effect on the average binding times was around 1.3 %, within statistical error.)

Equation (A3), which represents a Cholesky decomposition of the resistance matrix R (inverse of mobility matrix), is used to determine the Brownian force/torque:

$$F^B \, or \, T^B = \sqrt{\frac{6k_B TR}{\delta t}}\; N_r, \quad R = L \times L^T \qquad \text{(A3)}$$

where N_r represents 12 different random numbers in the range of (-1, +1) for the three elements of Brownian force and three elements of Brownian torque for both particles. The resistance matrix is written as the product of a lower triangular matrix with its transpose.[1]

A.2. References

1 Liu, J. & Larson, R. G. Brownian dynamics method for simulation of binding kinetics of patterned colloidal spheres with hydrodynamic interactions. *Journal of Chemical Physics* **138** (2013).

2 Jeffrey, D. J. The calculation of the low Reynolds number resistance functions for two unequal spheres. *Physics of Fluids A* **4**, 16-29 (1992).

3 Fixman, M. Simulation of polymer dynamics. I. General theory. *The Journal of Chemical Physics* **69**, 1527-1537 (1978).

4 Grassia, P., Hinch, E. & Nitsche, L. Computer simulations of Brownian motion of complex systems. *Journal of Fluid Mechanics* **282**, 373-403 (1995).

Appendix B: Supplementary Information for Chapter 3

B.1. Effect of pH drift

Figure B.1 shows the effect of pH drift on LBL growth of a PEI/PS- composite. PEI with a MW of 750 kg/mol and 41 nm-sized PS- particles were used for this experiment. For one case the pH of PS- suspension and rinsing waters was monitored prior to each respective deposition, while for the case without pH monitoring, the pH value of the solutions and rinsing waters was set at the beginning of the experiment.

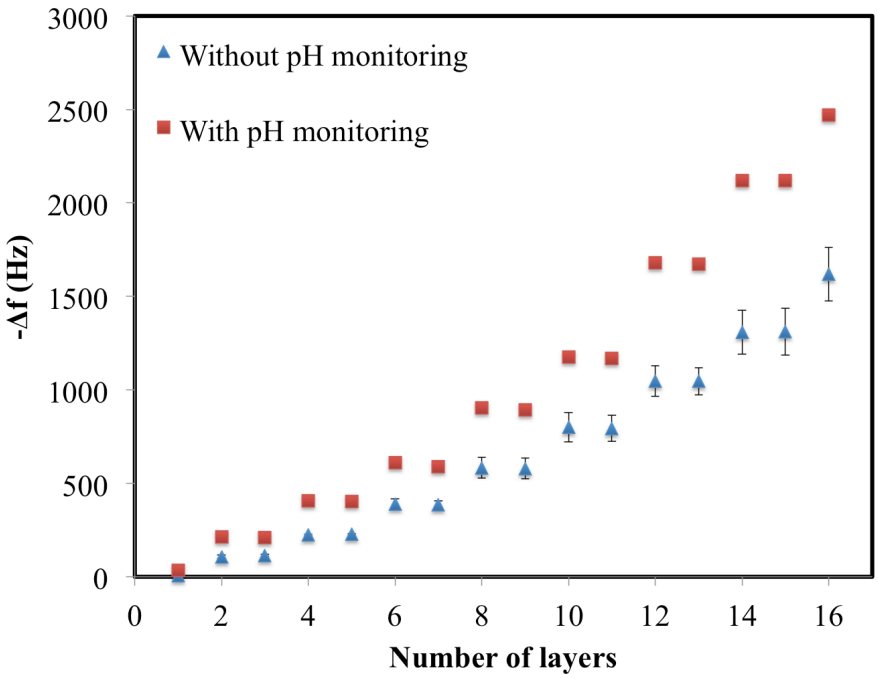

Fig. B.1. Influence of pH drift on the PEI/PS- film buildup, PEI (odd numbered steps) and PS- (even numbered steps) are deposited at pH values of 9.9 and 7, respectively. No salt was added to either of the ingredient of the LbL film except for the ions introduced to the solutions by pH adjustment.

As shown in Fig. B.1, by constantly monitoring and adjusting the pH, a boost in LbL growth is achieved. As mentioned in the Chapter 3, when the pH difference between PEI and PS- deposition steps is increased, faster LbL growth occurs. Adjusting the pH value of deposition solutions during LbL assembly enables one to better maintain such a pH difference.

B.2. Effect of deposition time

Figure B.2 depicts the effect of deposition time on the growth kinetics of a poly(ethyleneimine) (PEI)/polystyrene (PS) layer-by-layer (LbL) assembled film. PEI with a molecular weight (MW) of 70 kg/mol and 41 nm-sized negatively charged PS (PS- hereafter) nanoparticles were chosen for this experiment.

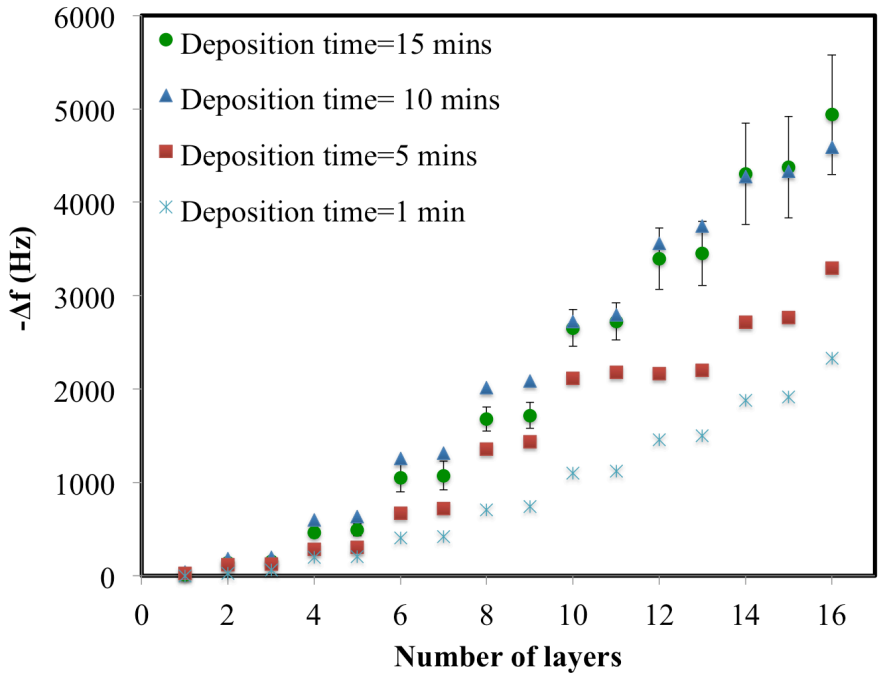

Fig. B.2. The effect of deposition time on LbL growth of PEI/PS- composite.

As shown in Fig. B.2, increasing the deposition time boosts the growth of PEI/PS- composites up to around 10 minutes deposition time. Upon increasing the deposition time up to this limit,

polyelectrolytes (PEs) and nanoparticles (NPs) are evidently more diffused to the film. However, it seems that the growth of the film becomes saturated and does not vary much beyond a deposition time of 10 minutes. This trend was observed in other LbL film buildup studies as well.[1] Based on these observations, 15 minutes was allowed for deposition during each step of LbL growth with QCM (8 double layers) in our experiments. However, for growing thick LbL films (59 double layers), a deposition time of 10 minutes was considered to save time while maintaining considerable film growth.

B.3. Film surface

Figure B.3 shows surface features of a sample LbL film obtained by optical microscope of the AFM.

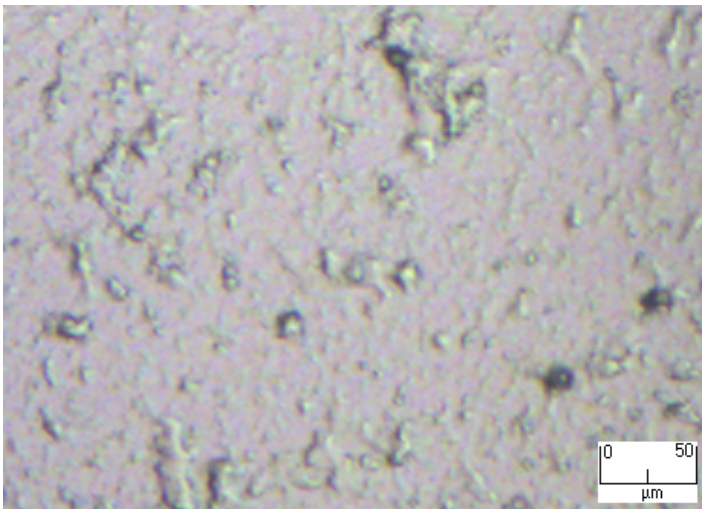

Fig. B.3. An optical micrograph of the surface features of the LbL films. PEI with a MW of 70 kg/mol and PS- particle size of 41 nm were used, with six double layers deposited.

B.4. Charge compensation factor

For the data shown in Fig. 3.2 in Chapter 3 of this dissertation, charge compensation factor defined by following equations is calculated and shown in Fig. B.4 below.

$$\Gamma_i = \frac{\Delta m_i^{NP} \sigma^{NP}}{\Delta m_i^{PE} \sigma^{PE}} \tag{B.1}$$

$$\sigma^{NP} = \frac{\#\ surface\ charges\ of\ NP}{Mass\ of\ NP} \tag{B.1.1}$$

$$\sigma^{PE} = \frac{f_{PE}}{MW\ of\ monomer} \tag{B.1.2}$$

In Eq. (B.1), Γ_i is the charge compensation factor calculated for each PE/NP double layer i, Δm_i is the deposited mass for each NP or PE layer, σ is the surface charge per unit weight, and f_{PE} is linear charge density of PE bounded within [0,1] such that a fully charged PE corresponds to f_{PE} = 1. The MW of a PEI monomer is 43.07 g/mol. The number of charged functional groups on the NP surface is determined using the surface charge density reported by the manufacturer. Note that the PE layer goes down first followed by the PS layer. Hence, overcompensation of PE charge by the deposited PS layer would require that $\Gamma_i > 1$. If $\Gamma_i < 1$, the PE charge is undercompensated.

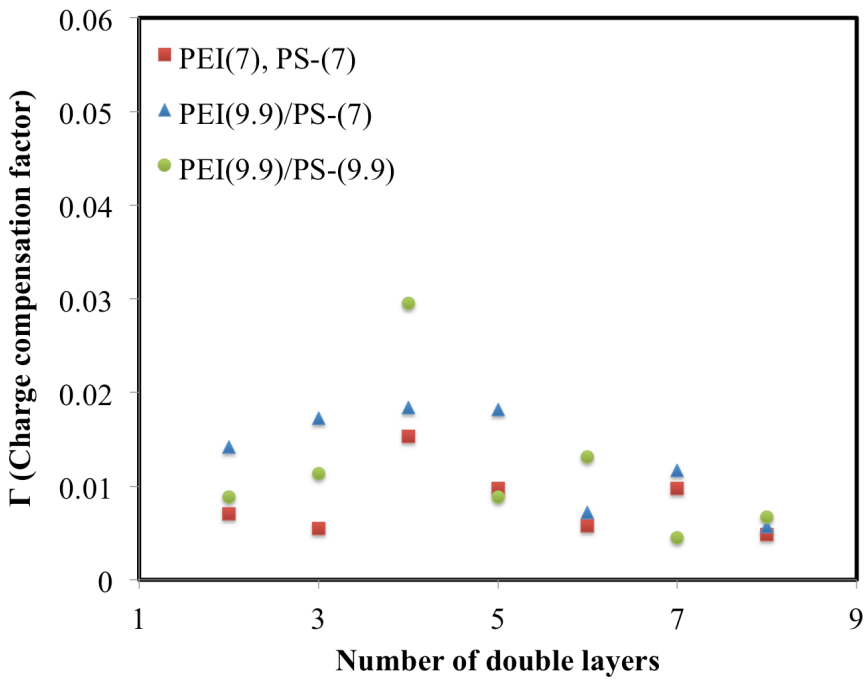

Fig. B.4. Charge compensation factor for PEI/PS- composites grown with different pH values (pH of each deposition solution is shown in the parentheses in the legend). PEI with a MW of 70 kg/mol and 41 nm-sized PS- particles are used for this experiment.

Conspicuous in Fig. B.4 is the very low charge compensation factor (on the order of 0.01) for PEI/PS- composites. We believe that NPs act as spacers and promote LbL growth despite not having a 1-to-1 charge compensation in the film.

In Fig. B.4, the data for the first double layer is not shown, since the value for Δm_i of PE for the first double layer was very low and the resulting value of compensation factor became very large, placing it significantly outside the range of the charge compensation factors for the rest of data points.

B.5. Effect of nanoparticle concentration on the growth of PAA/PS+ composite

Figure B.5 shows the role of concentration of positively charged PS (PS+ hereafter) NPs on the growth kinetics of poly(acrylic acid) (PAA hereafter)/PS+ multilayers.

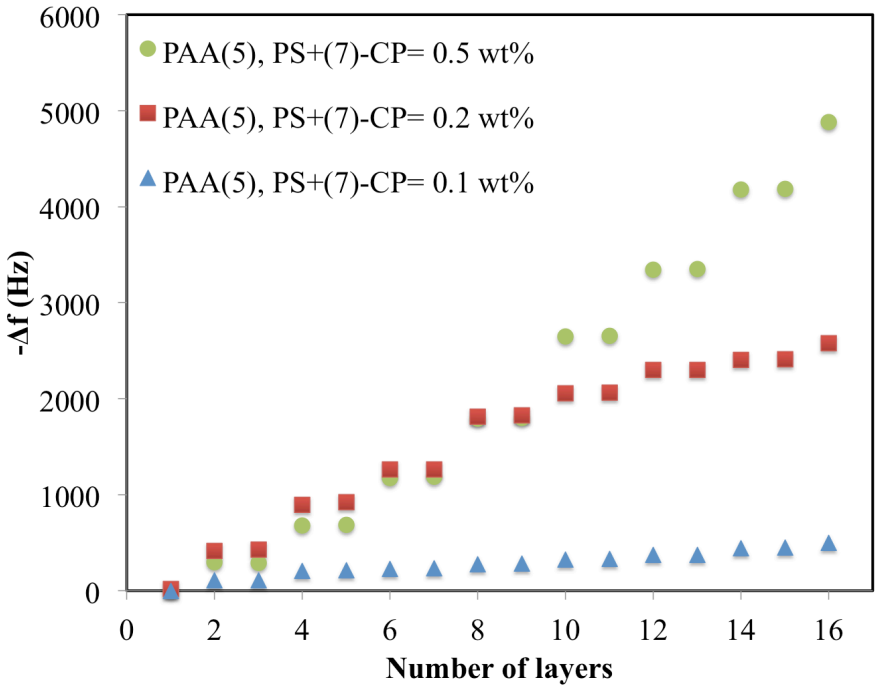

Fig. B.5. The effect of PS+ concentration on LbL film buildup of PAA/PS+ composite. PAA with MW of 240 kg/mol and 100 nm-sized PS+ particles were employed. CP refers to the concentration of particles.

According to Fig. B.5, increasing the PS+ concentration increases the film growth rate. The enhancement in the growth kinetics is more pronounced when the concentration is incremented from 0.1wt% to 0.2wt%. The rise in the number of NPs in the media presumably increases their availability near the solution-film interface and results in more adsorption into the film.

B.6. Effect of deposition pH on surface morphology of the LbL films

Figure B.6 contrasts the surface morphology of two LbL films deposited at different pH conditions. For both cases PEI with a MW of 70 kg/mol and PS- particles with 41 nm size were used. Other than ions introduced to the solutions for pH adjustment, no salt ions were added to the deposition solutions.

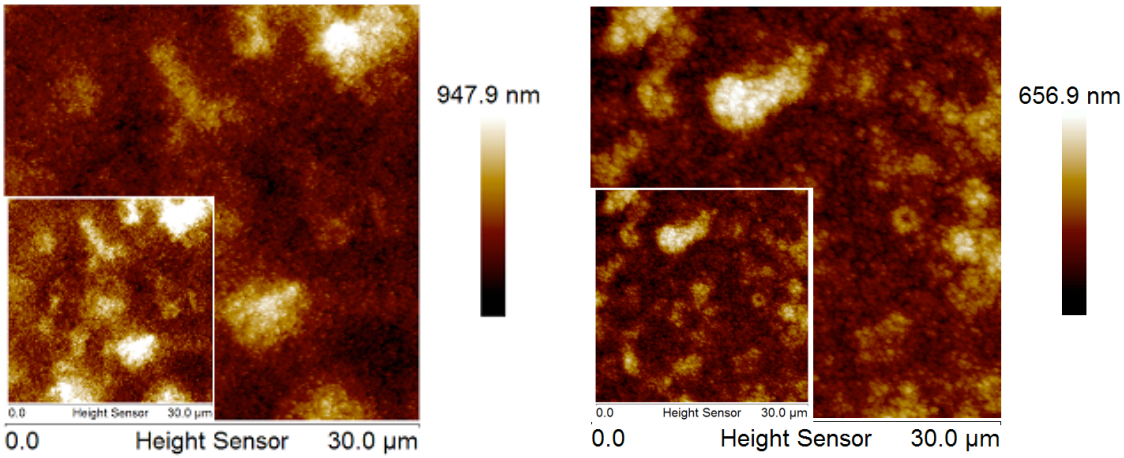

(a) (b)

Fig. B.6. Surface characteristics of LbL films composed of 8 bilayers of PEI with MW of 70 kg/mol and 41 nm sized PS- particles deposited at different pH values. No salt was added for the deposition of either of film ingredients. a) Film growth at pH amplified condition. PEI and PS- are deposited at pH values of 9.9 and 7, respectively. b) PEI and PS- are both deposited at pH value of 7. For the plots in the inset, maximum value of color bar is fixed to 700 nm.

As seen in Fig. B.6, films deposited at pH-amplified condition have a larger absolute roughness. However, as mentioned in the dissertation, this film has a much faster growth rate. Comparing the two plots in Fig. B.6 considering roughness to thickness ratio, one can understand that for a given film thickness, the film deposited in pH amplified condition has around 30 % less roughness value.

B.7. References

1 Rahman, M. & Taghavinia, N. Layer-by-layer self assembly deposition and characterization of TiO2 nanoparticles by using a short chain polycation. *The European Physical Journal-Applied Physics* **48**, 10602 (2009).